UNIVERSITÀ DEGLI STUDI DI PADOVA

UNIVERSITA' DEGLI STUDI DI PADOVA

Dipartimento di Ingegneria Industriale DII
Corso di Laurea Magistrale in Ingegneria Aerospaziale

Tesi di laurea magistrale in Ingegneria Aerospaziale

Surface integrity and superelastic response of a Room-Temperature Austenitic AM NiTi after heat treatment and machining

Relatore
Dott. Ing. Rachele Bertolini

Laureanda
Alessandra Guarise

Matricola
1236498

Anno Accademico 2022-2023

“It was much bigger than me
or the sum of any of its part.
It was like climbing a mountain
I couldn’t see the top of.
I don’t think I’ve ever felt so alive”

C.B.

Ringraziamenti

Approfitto di questo spazio per ricordare e ringraziare le persone che mi hanno circondato in questi mesi, in questi anni e coloro che sono con me da sempre.
Giunti a questo punto, sento di aver fatto parecchia strada e di averla condivisa con tante tante persone. Alcune di queste sono salite sul mio stesso treno per poi rimanerci, altre sono scese alla fermata successiva o a quelle dopo, qualcun altro è da poco salito.

Vorrei quindi ricordare e ringraziare…

La mia relatrice, la Dott.ssa Rachele Bertolini, per avermi appoggiata e capita più di quanto avrei potuto immaginare prima di iniziare questo percorso, grazie per essere stata la mia guida in questi mesi.

La Prof.ssa Stefania Bruschi per avermi coinvolta e ascoltata, ho apprezzato molto i confronti costruttivi che abbiamo avuto.

I miei amici di laboratorio Andrea e Edoardo. Siete stati la mia forza, il motivo di tante genuine risate, grazie a voi le cose sono sembrate più semplici e la salita una piacevole passeggiata. Senza di te Andrea sarei ancora a lucidare i provini (probabilmente sbagliandoli tutti) e le tue battute, Edoardo, sono state un vero toccasana durante la scrittura della tesi. Lo so, già mi manca l'A.R.E.A. team.

Un capitolo di ringraziamenti a parte andrebbe alla mia famiglia: siete stati il mio ossigeno quando non riuscivo a respirare, il più grande conforto quando esisteva solo il vuoto. E quanti pensieri, preoccupazioni, vicissitudini abbiamo condiviso, ci hanno fatto crescere insieme ogni giorno, ci hanno fatto arrivare alla meta. Inutile dire che senza Papà, Mamma e mia sorella Elena non avrei mosso un passo in università e in questa cosa complicata che è la vita.

Vorrei ringraziare i miei zii, i miei nonni e le mie cugine. Siete stati sempre molto premurosi e presenti a condividere con me i miei traguardi e, quando succedeva, anche gli insuccessi e le preoccupazioni. Grazie perché vi sento sempre molto vicini. Un saluto speciale a mio nonno Rico che non è riuscito a vedere la conclusione di questo percorso, hai creduto sempre molto in me e questo traguardo lo devo anche a te.

Un grazie agli amici dell'università che porto nel cuore.
Nicola e Martina dove saremmo arrivati senza il nostro mitico trio ProjetX? Avrò sempre nostalgia dell'ultimo progetto fatto insieme con te, Nicola, e di tutte le ore di sonno rubate, delle ansie e delle gioie condivise di quell'ultimo esame.
Non posso non citare il grande e mitico Stoppa (che da oggi chiamerò semplicemente Andrea). Con il tempo ho piacevolmente ritrovato in te un amico sincero e genuino con cui poter parlare di tantissime cose.
Elena e Alessandro, sarebbe stato bello conoscerci sin dal primo giorno della triennale. Abbiamo condiviso molte cose sui libri e non (come dimenticare la vostra super ospitalità a Berlino!). Voi, assieme a Giulia, Lorenzo e Matteo, siete stati un punto fermo in questi anni di magistrale e ho bisogno di credere che la nostra amicizia perdurerà nel tempo.

Un grazie agli amici che ci sono sempre stati e che mi conoscono da tempi immemori, grazie al gruppo degli Amiconi con il quale so di potermi mostrare per come sono e che siete garanzia di tante risate e serate spensierate.

Grazie alle mie passioni, al teatro e a tutti gli amici con i quali ho condiviso esperienze bellissime sul palco in questi anni a Padova.

Contents

LIST OF FIGURES

CHAPTER 2

CHAPTER 3

CHAPTER 4

CHAPTER 5

CHAPTER 6

LIST OF TABLES

CHAPTER 2

CHAPTER 3

CHAPTER 5

CHAPTER 6

CHAPTER 1

INTRODUCTION

The present thesis work aims to evaluate and analyse some of the main properties of the Nickel - Titanium alloy (NiTi) known as Nitinol (name originated by combining the abbreviations of its chemical composition with the initials of the laboratory, i.e., Naval Ordinance Lab, where it was first developed [1]).

Nitinol is primarily known to belong to the Shape Memory Alloys (SMAs) family.

Nickel-Titanium alloy is the best known of the SMAs, but copper or iron-based alloys also exist: Fe - Mn- Si, Cu - Zn - Al, Cu - Al - Ni.

As the name suggests, SMA means that the material returns to its original shape after undergoing deformation.

As reported in the following pages, shape return occurs under certain conditions. In this specific study, the focus is on the super-elastic property of the material.

This thesis work hopes to implement a study previously conducted by Khademzadeh, S., et al. [3], in which Nitinol cylinders are obtained by laser powder bed fusion (LPBF).

The work presented starts from the Nitinol cylinders and develops subsequent processes such as heat treatment and lathe machining with rough and finish turning.

Several process parameters were evaluated, resulting in specimens that differed by the temperature of the heat treatment and the type of machining conditions (flood or cryogenic).

As mentioned earlier, Nitinol is an SMA alloy, therefore it has specific properties that we want to analyse at the end of the established process chain.

The purpose of the study is to understand how Additive Manufacturing (AM), heat treatments, and machining affect the main properties of Nitinol.

To answer this question, several tests were carried out on the post-machining specimen, starting with material characterisation to check the surface integrity. To verify the super-elastic property of the alloy, transformation temperature analyses were executed to establish the conditions under which such properties may occur. Nano-indentation analyses were conducted to quantify the actual work recovery ratio of the material. From the literature, Nitinol is known to have good tribological properties, thus a tribological test was carried out through a pin-on-disk configuration. In that test, the pin is represented by the Nitinol sample and the disk is made of the same steel used in bearings.

Machining and tests were carried out at the TE.SI laboratory in Rovigo, except for the nanoindentation test conducted at Material Characterization Facility, Istituto Italiano di Tecnologia (IIT) located in Genova (IT).
For each test, the results of the different specimens are compared to see which process gives the best benefits in terms of super-elasticity, hardness, surface integrity and tribological properties of the material.
At the end of the study, a possible application is presented, which must be in line with the previous work and exploit the advantages of the NiTi alloy. Therefore, considering all the requirements, aerospace NiTi bearings could be the appropriate application intended to demonstrate shock resistance.

In this reading, the first chapters are focused on providing theoretical basis such as Nitinol and its properties and the physical aspects behind the experiments. The following chapters describe the test procedures and methods. Finally, the last chapters provide a summary and comparison of the results together with observations.

INTRODUZIONE

Nel presente lavoro di tesi, sono state valutate ed analizzate alcune delle proprietà della lega Nickel-Titanio (NiTi) conosciuta come Nitinol (nome dato dalla combinazione delle abbreviazioni degli elementi di cui è composto con le iniziali del laboratorio che lo ha creato, il Naval Ordinance Lab).

Si tratta di un materiale conosciuto principalmente perché facente parte della famiglia delle leghe con memoria di forma, SMAs (Shape Memory Alloys).

La lega Nickel- Titanio è la più conosciuta tra le leghe SMAs, ma è possibile trovare anche leghe a base di rame o ferro: Fe – Mn- Si, Cu – Zn – Al, Cu – Al – Ni.

Delle leghe SMAs, come suggerisce il nome, viene studiata la proprietà che permette al materiale di ritornare alla forma originale dopo aver subito una deformazione.

Come verrà riportato nelle seguenti pagine, il ritorno di forma avviene in determinate condizioni. In questo specifico caso il focus è sulla proprietà super-elastica del materiale.

Si vuole quindi analizzare come i processi di lavorazione del Nitinol influenzano e modificano tali proprietà e le condizioni in cui esse si verificano.

Tale lavoro di tesi si introduce. e auspica di implementare uno studio precedentemente condotto da Khademzadeh, S., et al il cui fine è stato l'ottenimento di cilindri in Nitinol tramite laser powder bed fusion con particolare attenzione ai parametri di processo utilizzati e ai diversi risultati ottenuti.

Il lavoro qui presentato parte dai risultati dello studio precedente, quindi dall'ottenimento dei cilindri di Nitinol, e sviluppa successivi processi quali trattamenti termici e lavorazioni al tornio con tornitura di sgrossatura e di finitura.

Sono stati valutati diversi parametri di processo ottenendo altrettanti campioni che differiscono principalmente dalla temperatura del trattamento termico e dalla tipologia di lubrorefrigerazione adottata nella lavorazione al tornio.

Come accennato in precedenza, il materiale in esame, rientra nelle leghe SMAs e, come tale, presenta delle proprietà specifiche che si vogliono analizzare alla fine della catena di processo stabilita. La domanda che ci si è posti per l'intero studio consiste nel capire come i processi di Additive Manufacturing (AM), trattamenti termici e lavorazioni al tornio hanno condizionato le principali proprietà del Nitinol. Tale quesito ha trovato riscontro nei risultati delle analisi effettuate sui campioni lavorati. Si è proceduto alla caratterizzazione del materiale con particolare attenzione all'integrità superficiale. Per verificare la proprietà superelastica della lega, si sono svolte analisi sulle temperature di trasformazione (TdT) così da stabilire le condizioni in cui si possono presentare tali proprietà, e analisi di nano-indentazione per quantificare l'effettivo ritorno elastico del materiale.

Viste le buone proprietà tribologiche del Nitinol acclamate in letteratura, si è effettuato un test tribologico avente configurazione pin – on – disk. In tale test, il pin è rappresentato dal campione di Nitinol, debitamente tornito affinchè presentasse una forma sferica, e il disk è una piattaforma in acciaio proveniente dal disco di un precedente cuscinetto.

In ciascuna prova si vuole valutare quale parametro di processo presenta maggiori vantaggi in termini di super-elasticità, durezza, densità e proprietà tribologiche del materiale.
A conclusione del lavoro svolto, viene presentata un'applicazione che rispetta le lavorazioni fin qui svolte e che sfrutta i vantaggi della lega NiTi. L'applicazione riguarda un cuscinetto a sfere ad uso Spazio pensato per resistere meglio agli shock.

Proseguendo nella lettura, si nota che i primi capitoli sono incentrati nell'offrire una base teorica dei temi trattati quali il Nitinol e le sue proprietà, descrizione delle lavorazioni e test, aspetti fisici alla base degli esperimenti. I successivi capitoli riguardano i procedimenti e metodi seguiti nelle varie prove, mentre i capitoli finali rappresentano un sunto e un confronto dei risultati ottenuti accompagnati dalle relative osservazioni e conclusioni.
Si auspica, infine, di presentare un lavoro di unione tra le varie lavorazioni e aspetti trattati che possa convalidare un ragionamento a prova delle proprietà della lega NiTi.

CHAPTER 2

THEORETICAL CONCEPTS

2. 1 SMA behaviour

In the early 1960s, Buchler and co-worker were the first to study the effect of shape memory in the equiatomic alloy NiTi. But it was not until 1970 that Jackson et al. did a thorough characterization of the material. Despite the high cost of this alloy, it remains of great interest because of its shape memory and super-elastic or pseudo-elastic properties.

A phase transformation induced by a change in temperature is the mechanism responsible for the *shape memory* property while the transformation induced by stress is the mechanism responsible for the *super-elastic* property.

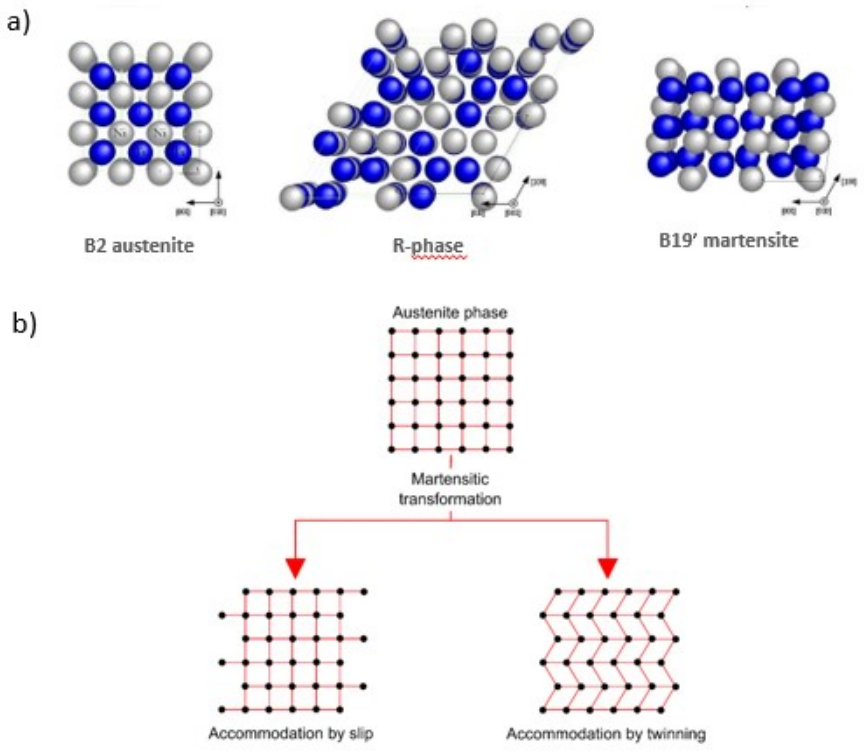

Figure 2. 1: (a) the structure of Nitinol [4]*, (b) the martensitic phase transformation scheme* [5]

The high temperature parent phase of the Nitionl alloy having a B2 crystal structure is called *Austenite,* on the opposite side there is the *Martensite* phase that is the lowest temperature phase in Nitionl with B19' (B19 prime) monoclinic crystal structure. An intermediate phase called the *R-phase* may occur under certain conditions.

2.1. 1 The R-Phase

The R phase is an intermediate phase between the B2 austenite and B19' martensite phases and it is characterized by a rhombohedral crystallographic structure (see Figure 2. 1(a)). There are conditions that facilitate the occurrence of the R phase at the disadvantage of the martensitic phase, for example when Nitinol has a high dislocation density, or when Ni-rich precipitates are present (due to heat treatments). These cases resist large strain in the crystal lattice. Therefore, the R phase is more likely to arise between the austenitic and martensitic phases since it requires less straining of the lattice.

2.1. 2 Phenomenology of the martensitic transformation

The key characteristic of all SMAs is the occurrence of a martensitic phase transformation between the austenitic phase and the different variants of the low temperature, low symmetry martensitic phase. The martensitic transformation is a shear-dominant diffusionless solid-state phase transformation occurring by nucleation and growth of the martensitic phase from the parent austenitic phase [6] Therefore, when an SMA alloy undergoes a phase transformation then the high-symmetry, cubic austenitic phase gives way to the low symmetry martensitic phase.
A diffusionless transformation is an instantaneous distortion in the crystal lattice (B2 ←→B19') that occurs at the speed of the sound. In contrast, diffusion transformations, as common in steel alloys, requires the diffusion of atoms over relatively long distances. Diffusion requires heating the alloy at high temperature for extended periods of time [5] The term shear-dominant means that the martensitic transformation of Nitinol is characterized by a shear/shuffle in the crystal lattice due to a change in the thermodynamic stability of the system. In the steel alloys martensitic transformation, the dislocation motion (i.e. slip) is irreversible while twinning in Nitionl is reversible [5] (see Figure *2.* 1)

Transformation temperatures play an important role and are reported as follows: A_s (austenite start) and A_f (austenite finish) refer to the temperatures at the beginning and end of the transformation from martensite to austenite phase, similarly M_s (martensite start) and M_f (martensite finish) indicate the beginning and end of the austenite to martensite transformation. The martensite deformation temperature M_d has a key role as it represents the maximum temperature at which super-elasticity can occur. The martensitic phase transformation begins at M_s and continues as the temperature drops until it reaches M_f where transformation ends. The material is then fully austenitic. The reverse transformation (martensite to austenite) can then occur at temperature A_s and continues until A_f is reached ($A_f > A_s$). At this point, the material is fully austenitic.

The transformation temperatures depend mainly on the composition of the alloy and the previous processes. Microstructural defects, precipitates, and grain size can alter transformation temperatures by several degrees [6]

The direct transformation from austenite to martensite (A → M) is an exothermic phase transformation because it is associated with a release of heat due to a change in enthalpy. The reverse transformation, from martensite to austenite (M →A), is accompanied by heat absorption so it is an endothermic phase transformation. The amount of heat exchanged is proportional to the volume fraction of the transformed material. Because of these characteristics, it is possible to measure the transformation temperatures using differential scanning calorimeters (DSC).

2.1. 3 Shape Memory (SME) and Super-elasticity effects

Shape memory property occurs when the material is in the martensitic phase.

For the following explanation, refer to the O → A → B → C → O path of the stress-strain-temperature graph (see *Figure 2. 2)*. In the O →A step, the material undergoes cooling to a temperature below that of M_f, thus at A the structure is twinned martensite. At this point the material undergoes deformation (A → B) which leads to the arising of stress and inelastic deformation, in B the structure is detwinned martensite. Strains are recovered only in the last step C→O where SMA loses the detwinned martensite structure and returns to its cubic parent form.

To get from C to O, the material is heated to a temperature higher than A_f. Therefore, the crystallographic lattice clearly undergoes changes throughout the path. The absence of macroscopic deformations in the first step (O → A) is due to the self-accommodating growth of the martensitic variants. In this phase the interfaces are highly mobile, this great mobility is at the heart of the shape memory effect. The load presence in the second step (A → B) leads to the reorientation of the variants, thus large strains are created. In the last step (C → O), the material is heated, then the martensitic phase becomes unstable in the absence of stress. Finally, the parent phase is restored and the SMA returns to its original shape.

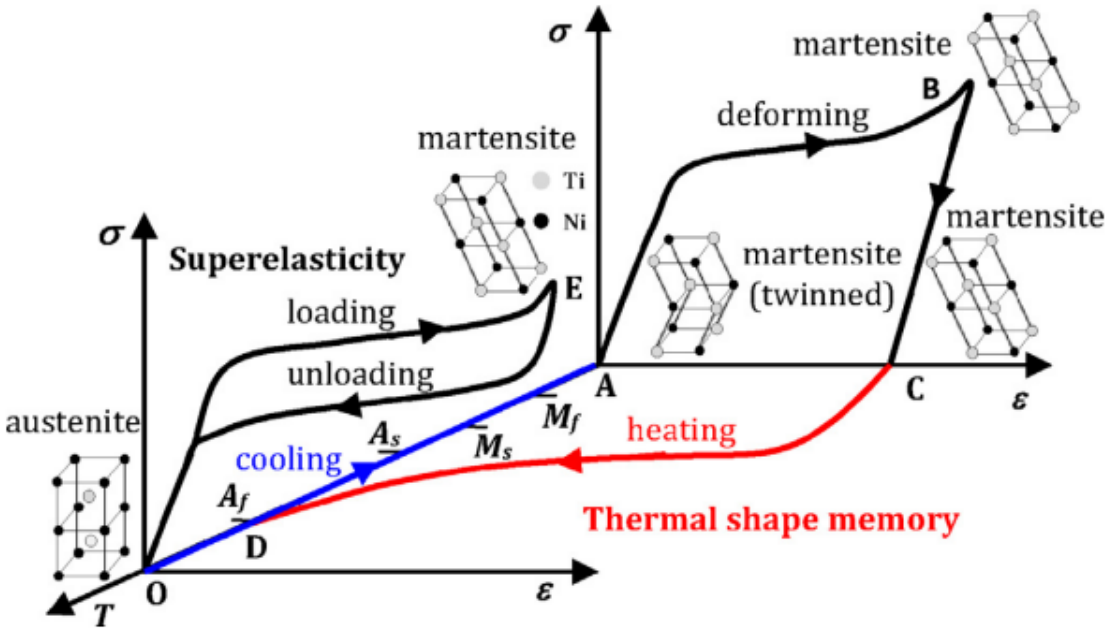

Figure 2. 2: stress-strain- temperature diagram of Nitinol [7]

The diagram in *Figure 2.2.* also shows the effects of super-elasticity. To have super-elasticity, the starting point is at a zero-stress level, above A_f thus fully austenitic (point O in the diagram). Subsequently, the material undergoes loading accompanied by an increase in stress. In this step (O → E), the transformation from austenite to martensite takes place until point E where there is complete martensite. Large strains arise during the transformation. Further load increases result in no further phase transformation. When the load is released (E → O), the reverse transformation from martensite to austenite begins and strains fully recover. At O the material is in its original shape and fully austenitic. Note that the path is hysteresis-shaped, the thermal hysteresis is the difference in the phase transformation temperatures when the alloy is heated versus when it is cooled (see *Figure 2. 2 (a)*) [5].

Now refer to *Figure 2. 3* (*b)* which shows a typical cyclic tensile curve for super-elastic Nitinol. At applied load (A to D) elastic deformation occurs until UPS (Upper Plateau Strength/Stress) is reached (at point B). From B to C there is an iso-stress phase where the material transforms from austenitic to detwinned martensitic, followed by the elastic deformation of the SMA from C to D. In the return curve (D → A) the load is no longer applied, the elastic deformation is recovered, and the material returns to its original form, thus austenitic in A. Note that LPS (Lower Plateau Strength/Stress) is the stress at which the transformation from martensite to austenite occurs and it is less than UPS.

A typical Nitinol alloy will exhibit super-elasticity up to 8% strain before permanent deformation begins. However, there is always some percentage of permanent or residual elongation, El_r. The magnitude of El_r depends on the past thermomechanical processing of the material and on the % strain the component was subjected before unloading [5]

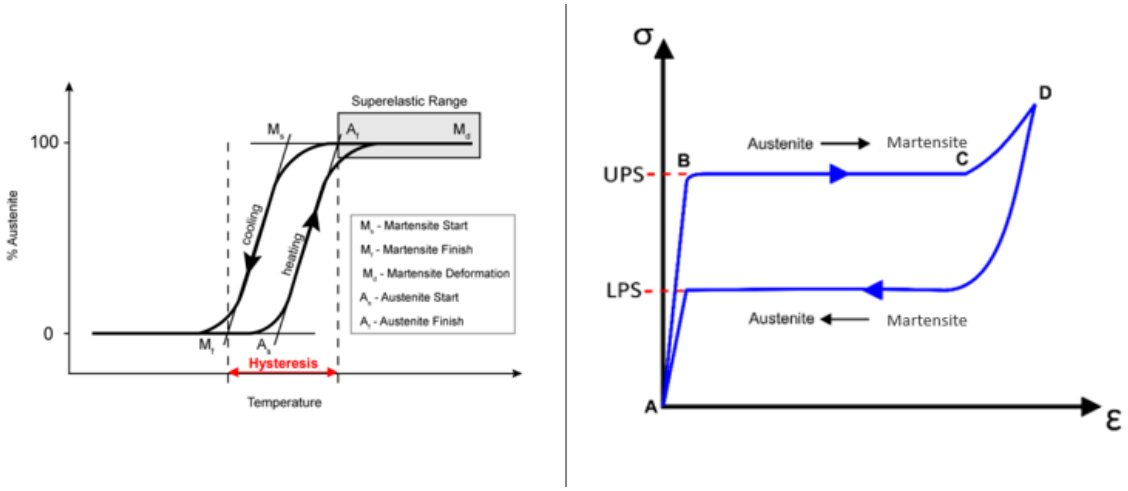

Figure 2. 3: (a) Thermal hysteresis, (b) stress-strain diagram of the Nitinol super-elasticity [5]

2.1. 4 Nitinol's many properties

The nitinol alloy has a unique combination of properties that make it attractive for various applications. The ratio of Ni and Ti elements are important factors to guarantee the desired functional properties. NiTi parts fabricated from a Ti-rich powder (i.e., where the percentage of titanium is greater than that of nickel) exhibit the shape memory effect, those fabricated from a Ni-rich powder (i.e., where the percentage of nickel is greater than that of titanium) demonstrate super-elasticity behaviour [8]

Hardness also depends on composition. For example, in Ni-rich NiTi alloys, hardness arises with increasing nickel content; in fact, higher nickel content increases the volume fraction of hard coherent Ni_4Ti_3 precipitate.

In this study, a Ni-rich NiTi alloy will be treated. This alloy has a high hardness (comparable to that of steel), low elastic modulus, large recoverable strain range and high compressive strength. In addition, this SMA alloy has a moderate density (approximately 15% lower than that of steel), high corrosion resistance, electrical conductivity, and low magnetic permeability. Good tribological properties such as wear resistance and low coefficients of friction have also been found [9].

These properties make Nitinol an interesting material for biomedical, aerospace, and marine applications for the manufacture of gears, valves, bearings, medical tools, etc. It is a difficult material to machine, so the use of sharp carbide tools, light feeds and slow speeds is recommended.

2. 2 Additive Manufacturing (AM) to produce Nitinol parts

The high ductility, adhesion, hardness, and burr formation make Nitinol difficult to machine and cause high tool wear. Additive manufacturing is a tool-less process that reduces the problems associated with the machinability of Nitinol. In fact, the part produced by AM only requires finishing operations.

2.2. 1 Powder preparation

The AM technique starts with the powders; therefore the Ni/Ti ratio must be chosen when preparing the powders. In this case, a Ni-rich NiTi alloy was used to obtain the super-elastic effect. On the other hand, with a Ti-rich alloy, the shape memory property and a higher transformation temperature are obtained.

To get NiTi powders, it is common to start from a pre-alloyed NiTi ingot; less often, blending of nickel and titanium elementally is used, so it is preferable to begin directly with the alloyed ingot.

There are several techniques for obtaining the powder, the most common being: hydriding, mechanical attrition, water atomisation and gas atomisation. Many of these techniques have the disadvantage of producing a powder with a high level of impurities (e.g., high hydrogen content in water atomisation and hydriding) or powders with irregular shapes as in mechanical attrition.

Gas atomisation is the most suitable technique because it produces a powder with fewer impurities and a more regular shape due to the use of an inert gas in the process chamber and a lower particle solidification rate.

NANOVAL is one of the most widely used methods of ingot gas atomisation. The ingot is melted in a graphite crucible in an autoclave under an inert atmosphere (usually argon) and then the molten ingot is passed through a nozzle. A flow of gas is injected into the nozzle to stabilise the molten material. In the throat of the nozzle, the gas flow is accelerated to break the molten stream into many droplets which are collected and solidified in an atomisation tower and finally deposited in a vacuum chamber. The main disadvantages of NANOVAL method are the formation of distinct numbers of particles, the adhesion of small particles to the larger ones, and the existence of impurity contents (carbon 0.03-0.1 wt.%; oxygen 0.05-0.18 wt.%) [8]

It is important to note that the powder size influences the microstructure of the material. It has been found that a medium powder size (between 25 and 75μm) is preferable to achieve spherical shape, good flowability (ability of the powder material to flow), low impurity content and excellent transformation ability [8].

2.2. 2 Laser powder bed fusion

In the previous study conducted by Khademzadeh, S., et al [3], the AM technique known as Laser Powder Bed Fusion (LPBF) was used to produce the Nitinol parts. The work starts with the creation of a CAD model (including the geometry of the parts and the support), and the setting of process parameters such as laser power, scanning speed, hatch distances, input energy density, layer thickness and laser spot diameter.

In this process, there is a device that deposits a layer of metal powder (10-30 microns) onto a platform positioned on a cylinder. Once the layer is deposited, the laser melts the shape corresponding to the section to be machined. At the end of the process, the part is removed together with the platform.

The oxygen level has to be controlled for the production of NiTi parts through filling the working chamber with argon to minimize the possibility of oxidation.

Optimal parameters are methodically developed to make sure that the final product is not only fully dense, but also shows a low level of impurity contents.

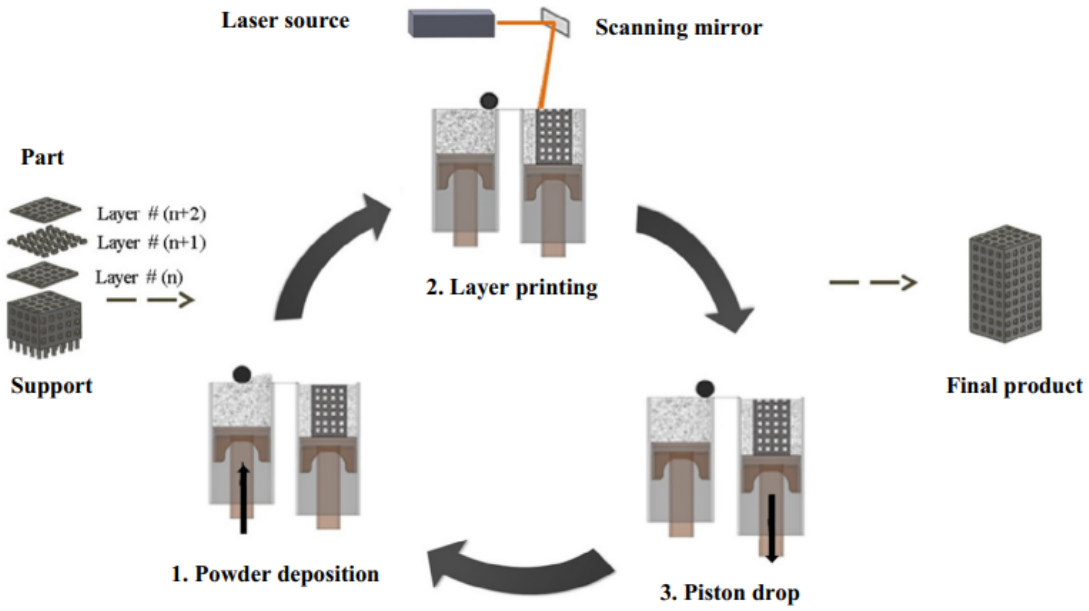

Figure 2. 4: three steps procedure of the laser powder bed fusion (LPBF) mechanism [8]

2.2. 3 Khademzadeh, S. results [3]

As mentioned above, this work was preceded by a study carried out by Khademzadeh, S**.** et al. to investigate the effects of LPBF process parameters on phase composition, porosity, and surface topography in NiTi parts. Three different regimes of process parameters, that differ in laser power and scanning velocity, were successfully developed in this research.
The main achievements of the Khademzadeh's work are:

(i) using high laser power in LPBF of NiTi produces a single-phase austenite containing sharp peaks in the XRD analysis. This result can be attributed to the highly crystalline and coarse grain structure.

(ii) the increase in laser power leads to an improvement in surface quality and a reduction in complexity.

(iii) Optimisation of LPBF process parameters (high level of laser power and scanning velocity) results in minimum porosity and surface roughness.

2. 3 Heat Treatment

The reason why Ni-rich NiTi alloys exhibit the super-elastic property is because they have higher strength than Ti-rich NiTi or equiatomic NiTi [8]. After an AM process, heat treatment (annealing and ageing) is recommended to restore the initial strength of the material and facilitate the super-elastic property. In fact, the reduction in the strength of the material is due to the nucleation of martensite in the austenitic zones. This process is reversed by the heat treatment (especially by ageing).
In this research work, some of the specimens obtained by AM are subjected to a heat treatment. This consists of *stress-relief annealing* followed by *ageing* treatment.

Stress-relief Annealing's purpose is to reduce or eliminate residual stress or defects of the workpiece and provide an equilibrium state for the material. In fact, residual stress may have been induced by the AM process.
Ageing is used to restore the original strength by forming Ni-rich precipitates which act as barriers to dislocation formation and do not favour the nucleation of martensite.

A Ni-rich alloy generally exceeds the limit of Ni solubility, and, therefore, the extra Ni tends to form Ni-rich precipitates such as $Ni_4Ti_3, Ni_3Ti_2, Ni_3Ti$ within the matrix [8]
These precipitates depend not only on the conditions of heat treatment (temperature and duration) but also on how the specimen is cooled after treatment (e.g., water, oil, air quenching etc.)

2.3. 1 Effect of heat treatment on transformation temperatures

As a result of annealing, the transformation temperatures decrease, thus the martensitic transformation is delayed. This phenomenon is because precipitates are dissolved during annealing and the new ones are suppressed during water quenching, leading to depletion of Ti in the matrix and, therefore, decreasing the transformation temperatures. Another consequence of annealing is that the peak width (in DSC results) of the martensitic transformation also decreased for Ni-rich material. The reason for this behaviour is that the annealing process leads to a more homogeneous equilibrium state, so that the material does not encounter any obstacles during transformation, so that there is a single step transformation during both cooling and heating.
Several studies have thus confirmed that lower transformation temperatures and single-phase transformation as the result of solution annealing [8]

On the contrary, ageing can lead to a two-step transformation with two distinct peaks. The first peak relates to the R-phase, thus, as the material cools, it shows the transformation from austenite to R-phase; only after the second and final peak does complete martensite occur.
R-phase generally appear during cooling because the kinetic barrier to form R-phase is lower than that to form martensitic phase. However, the presence of the R- phase can also be seen when martensite is transformed into austenite, i.e., when the material is heated. The reasons why aging treatment leads to the multi-step transformation are:

i) The precipitates formation
ii) The difference in the nucleation barriers for the R-phase and martensite
iii) Super saturation of Ni leading to a Ni concentration between particles
iv) Grain size

Let's have a closer look at the reason and the origin of these causes:

because of ageing between 200 and 800°C, the austenitic phase of the NiTi alloy decomposes into multiphase systems consisting of stable $NiTi$ or $NiTi_2$ and Ni_3Ti phases. The decomposition of the Ni-supersaturated solid solution at temperatures below 800°C leads to the formation of a Ni-rich metastable phase (Ni_4Ti_3 is one of the most important of these phases) [4].
The size of Ni_4Ti_3 precipitates varies with the temperature of the ageing process. Numerous studies have shown that the precipitate size decreases as the heat treatment temperature decreases. For example, at ageing temperatures of 600°C, precipitates can exceed 1 micron and they are regarded as incoherent with the matrix. At lower ageing temperatures, e.g., 500°C, the size decreases to a few hundred nanometres and the precipitates are regarded as fully coherent with the parent matrix.
Coherence occurs when Ni_4Ti_3 is surrounded by strain fields, which inhibit dislocation growth and increase the NiTi mechanical strength and shape memory property.
Beside the strain field, fine Ni_4Ti_3 precipitates create Ni concentration gradients in the surrounding NiTi matrix. The Ni concentration combined with the strain field creates a strong resistance to the formation of the direct large transformation from B2 austenite to B19' martensite. In this way the single step transformation is transformed into a two (or more) steps transformation with two lower energy barriers. A lower Ni concentration can lead to an increase in the temperature at which martensite begins. In addition, the strain field around the precipitates favours the formation of the R phase. The elastic interaction between the martensite nucleus and the precipitates does not favour the transition from austenite to martensite.

As the increasing of aging temperature precipitates tend to increase in size, losing coherence with the matrix[10]. The strain field generated by coherent precipitates favors the formation of R-phase. It is also reported that the precipitates lose coherency with the matrix when they are large enough (disc/needle shape), hence the R-phase disappears.
At intermediate ageing temperatures (300-400°C) there is the highest concentration of precipitates around which Ni atoms congregate. As a result, the NiTi matrix is enriched with Ti atoms, resulting in higher transformation temperatures. At ageing temperatures above 500°C, some of the precipitates dissolve and Ni atoms diffuse back into the matrix. This decreases the transformation temperatures[11].

The main effects of different heat treatments (stress relief annealing, ageing at 300°C, ageing at 600°C) on martensitic transformation are summarized in the following table where M1, M2, …, Mn all represent the transformation to B19' martensite.

	Kind of transformation	**TTs**	**Precipitates**
S.R. annealing	Direct (B2 ⇄ B19')	Decrease	Usually undetected
T300	Multi steps (B2 →R→M1→...→Mn)	Increase	Fine and coherent with the matrix
T600	Usually direct (B2 ⇄ B19')	Decrease	Bigger and incoherent with the matrix

Table 2. 1: Summary of the effects of heat treatment on martensitic transformation

The three stages of martensitic transformation are shown in the figure *Figure 2. 5*. In the first step (a) the austenitic phase transforms into the R-phase which begins to nucleate and expand into the B2 matrix. In the second step (b) the R-phase transforms into B19' whose expansion is limited by thecoherent stress region. Finally, in the last step (c), the regions outside the coherent stress boundary are transformed into martensite.

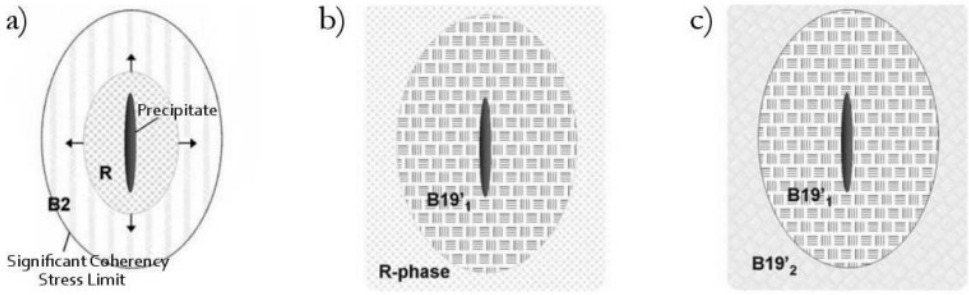

Figure 2. 5: multi-step martensitic transformation due to coherency strain field around precipitates [4]

In a further study [4], the different morphologies of Ni_4Ti_3 precipitates within the grain were investigated. As can be seen from the *Figure 2. 6*, the grain is divided into three regions as there are three transformation steps from austenite to martensite (B2 →R→M1→M2→M3) where M1, M2 and M3 all represent transformations to B19' martensite. At the intermediate part of the grain (zone *1*) the transformation from austenite to the M1 peak takes place. In the grain boundary (zone *2)*, the transformation corresponding to peak M2 occurs. Both transformations are associated with the transition to the R phase. Finally, at the centre of the grain (zone *3*) there is a direct transformation that involves the M3 peak.

It is interesting to note that the presence of the R phase is related to the coherent precipitates in zones 1 and 2 and their corresponding strain fields. It was also observed that the precipitates within the grain are much larger than those near the boundary.

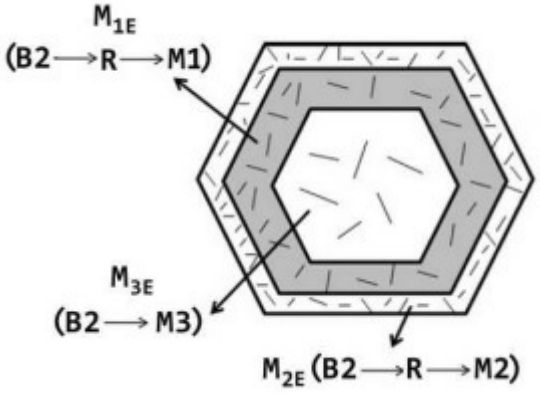

Figure 2. 6: grain divided into three areas according to precipitates size [4]

Now it is well accepted that the large-scale microstructural inhomogeneity between the grain boundary and the grain interior is one of the main reasons for inducing the multistage R-phase transformation. It was found that samples with large grains (average grain size between 6 and 21 μm) are more inclined to form the R phase, unlike samples with smaller grains (smaller than 5.6 μm) where the martensitic transformation is usually direct (B2 ⇄B19') [12].

Moreover, the formation of $NiTi_2$ precipitates may change the chemical composition of the matrix, leading to the change of R-phase transformation temperatures.

However, further studies are needed to better understand the occurrence of the R-phase in relation to chemical composition, precipitates (coherency, size, density), grain size, etc.

2. 4 Machining

Cutting operations remove material from the various surfaces of a workpiece as it is clamped and rotated by the jaws of a chuck. Machining produces chips and an axially symmetrical part [12].
Two cutting processes were used in this research:

- Turning: the workpiece is rotated and a cutting tool removes a layer of material as the tool moves along its length (see *Figure 2. 7 a*).
- Cutting off: the tool moves rapidly inward and separates the piece from the blank (see *Figure 2. 7* b).

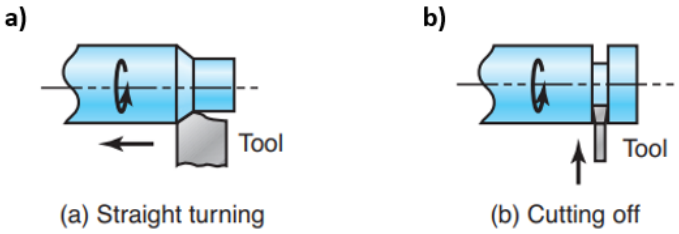

Figure 2. 7 cutting processes: a) straight turning, b) cutting off [13]

In the cutting processes, it is important to identify the main parameters that influence the machining and the result. The velocity at which the cutting tool travels to the left as the workpiece rotates is called the *cutting speed* (m/min), V_c, while the depth at which it is set is the *depth of cut* (mm), a_p, and finally the *feed rate*, or *feed* (mm/rev), f, is the distance the tool travels per unit revolution of the workpiece.
In this study, the following independent variables were evaluated: cutting speed, feed rate, depth of cut and cutting fluid. They affect forces, power, temperature rise, tool life, chip type, surface finish and integrity.

2.4. 1 Surface finish and integrity

Surface finish influences the dimensional accuracy, the properties, and the performance of machined parts and it refers to the geometric features of a surface. Surface integrity treats the material properties, such as fatigue life and corrosion resistance, thar are influenced by the nature of the machined surface.

In a turning operation, as the tool moves across the workpiece, it leaves a spiral profile called feed marks (see *Figure 2. 8*) on the machined surface. The higher the feed, f, and the smaller the tool-nose radius, R, the more prominent the feed marks will be, hence the surface roughness, R_t, is given by:

$$R_t = \frac{f^2}{8R} \tag{2. 1}$$

Feed marks are important in finishing machining as they characterize the surface integrity.

It is worth mentioning the factors influencing surface integrity as it is the subject of this study. Such factors are: temperatures generate during machining and possible metallurgical transformation, surface residual stresses, plastic deformation and strain hardening of the machined surface [13].

Surface integrity aspects of NiTi SMAs have been investigated below by considering surface roughness, phase transformation, microhardness.

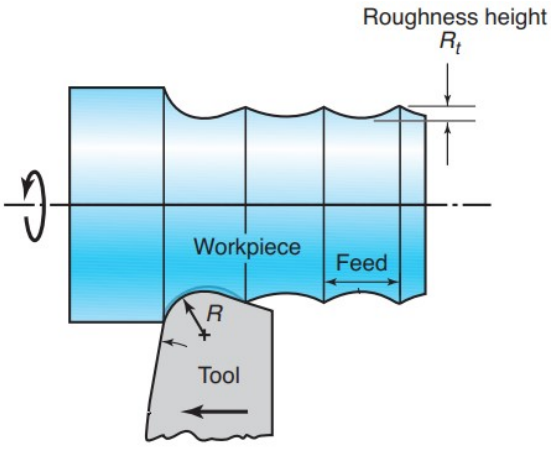

Figure 2. 8: feed marks on a machined surface [13]

2.4. 2 Surface structure

The surface of a piece of metal generally consists of several layers. In this study, attention was focused on two layers in particular: the metal substrate layer, and the severe plastically deformed (SPD) layer:

- The metal substrate layer, or *bulk*, has a structure that depends on the composition and processing history of the metal.

- The severe plastically deformed (SPD) layer is above the bulk metal and has typically been plastically deformed and work hardened during the manufacturing process. The depth and properties of this layer depend on the processing method used.

2.4. 3 Flooding machining

As mentioned earlier, cutting fluid is an independent variable that affects surface integrity among other things.
In the current study, machined samples obtained using cutting fluids (flooding) have been compared with the less conventional method in which a cryogenic gas is used during the cutting process (cryogenic). Let us take a closer look at the two different techniques.

Cutting fluids play a very important role in machining operations since:

- reduce wear and friction by increasing tool life and improving the surface finish of the workpiece.
- cool the cutting zone by reducing machining temperatures.
- reduce the forces and energy involved.
- move chips away from the cutting zone.
- protect the machined surface from corrosion.

The cutting fluid gains access to the tool-chip interface through the capillarity action of the interlocking network of surface asperities in the interface. Because of the small size of this network, the cutting fluid should have a small molecular size and possess proper wetting characteristics [13].

There are four different types of cutting fluids:

- oils: these include vegetable, animal, mineral, compound, and synthetic oils.
- emulsions (soluble oils): these are a mixture of oils, water, and additives. The water acts as a coolant, the oil prevents oxidation caused by the water, emulsions are used for high-speed machining where high temperatures are reached.
- semi-synthetics: these are chemical emulsions containing small amounts of mineral oil, diluted in water with additives that reduce the size of the oil particles.
- Synthetics: chemicals with additives diluted in water without oil.

In this study, the *high-pressure flooding system* is the cutting-fluid application used to process the specimens. It is a high-pressure coolant system that can increase the rate of heat removal during machining. The fluid is sprayed at high pressure through nozzles that produce a powerful jet of fluid directed at the cutting zone. Pressures are typically in the range of $5.5 \div 35$ *MPa* and it requires a large quantity of fluid ($10 \div 225$ *l/min*). This method is particularly suitable for materials that are difficult to machine. Today, efforts are being made to adopt methods that use less cutting fluid (minimum quantity lubrication, MQL) for environmental and health reasons.
When choosing the cutting fluid to be used, it must be remembered that this choice has an impact on the workpiece material, the machine tool components, the environment, and the cost.

2.4. 4 Cryogenic machining

It is not easy to identify the boundary between refrigeration and cryogenic temperatures. Several standards define cryogenic as temperatures below -180°C, since the boiling point of most permanent gases (helium, hydrogen, nitrogen, neon, etc.) is below that temperature [14].
In cryogenic machining, a liquid nitrogen (LN_2) is used as a coolant. Nitrogen is an inert, non-hazardous, non-toxic, non-flammable, colourless and odourless gas, which constitutes 79% of air. It is lighter than air and disperses into air after application. Low-temperature machining improves the hardness and toughness in the cutting tool material, thus increasing the material removed rates, resulting in lower energy consumption and higher productivity compared to flood machining. The finished part also shows improvements in terms of surface integrity, wear resistance, corrosion resistance and fatigue life as a result of the cryogenic treatment [14].
The following table (*Table 2. 2*) compares different aspects of cryogenic versus flood machining.

Effects	Flood	Cryogenic (LN_2)
Cooling	Good	Excellent
Lubrication	Excellent	Marginal
Chip Removal	Good	Good
Machine cooling	Good	Marginal
Workpiece cooling	Good	Good
Product Quality (surface integrity)	Good	Excellent
Sustainability Concerns	Water pollution, microbial infestation, high cost	Initial cost

Table 2. 2: flood and cryogenic effects comparison [14]

Several studies confirm that the near-surface layers are characterised by grain refinement due to cryogenic processing, which leads to severe plastic deformation (SPD). Surface-near grains are refined in the nano range [14].

In addition, grain refinement is one of the main causes of the increase in surface hardness of cryogenically machined material.

Cryogenic machining is also known for improving the surface quality, in fact the surface roughness is generally lower with cryogenic machining than dry or flood machining.

Another aspect that distinguishes cryogenic from flood machining is that in the former, the workpiece is martensitic during the cutting process because the temperatures are low. Therefore, less force is required to remove material in cryogenic machining. In flood, and even more so in dry machining, the temperatures are higher, and the material is therefore likely to be in the austenitic phase, so the cutting forces are also higher.

2.4. 5 Effect of machining on processing temperatures

To examine the martensitic transformation peaks of the workpiece, the DSC instrument is used, which provides graphs like those shown in *Figure 2. 9*. Peak broadening and increased transformation temperature are the typical response of machined samples as compared to as-received material. During the cutting process, martensitic transformation is delayed or even suppressed due to the stresses and increased dislocation density caused by machining (see *Figure 2. 9 a) and c*)).
Dislocations are defects in the orderly arrangement of a metal's atomic structure. Very high cutting temperature annihilate or reduce the dislocation density and result in forward transformation after machining process (see *Figure 2. 9 case b*)[15]. Thus, the cutting temperature plays an important role on surface phase state of machined NiTi alloys. Therefore, at higher cutting speeds, the peck does not broaden as much as it does at low speeds. In fact, during the cutting process, temperature increases more and thus reduces the density of dislocation and defects in the machined surface [15]
Cryogenic cutting achieves temperatures below Af, resulting in residual stress and plastic strain due to high dislocation density, leading to the stabilisation of martensite (aka transformation temperature rise).

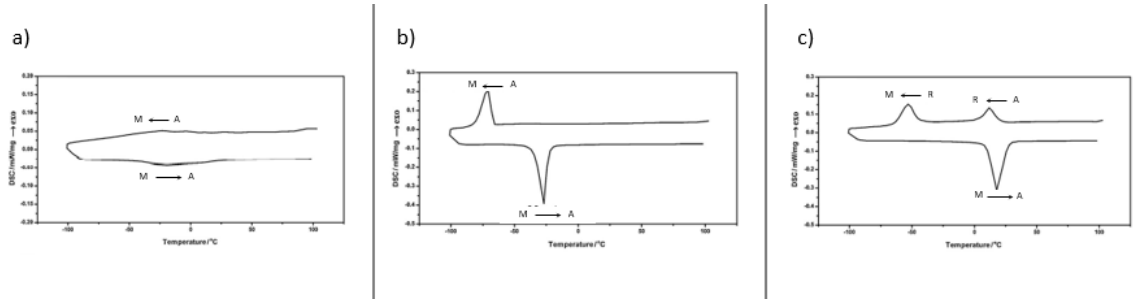

Figure 2. 9: DSC curves showing different types of martensitic transformation peaks, a) very broad peaks and therefore difficult to detect, b) well defined sharp peaks, c) intermediate situation between case a) and b) with R-phase peak [16].

Referring to *Figure 2. 9,* it can be assumed that:
case a) represents the case where the phase transformation is difficult to achieve (the peak is only hinted at). In this case the dislocation density is high and the processing temperatures are low.
case b) is where the martensitic transformation occurs directly, the peaks are sharp, so the processing temperature is high enough to have a low dislocation density.
case c) is the combination of the two previous cases. Due to the stresses and dislocations, the transformation is not direct and there is an R-phase.
As cryogenic machining uses very low cutting temperatures, it should fall under *case a)* or, if the cutting speed is increased, *case c).* However, there are several other factors that can influence the martensitic transformation by accelerating or slowing it down. These include the presence and type of precipitates in the material.

2. 5 Surface Roughness

Surface roughness indicates is a value calculated by measuring the average of heights and depths across a machined surface. Measuring surface roughness is integral to determining the compliance of equipment and products with industry regulations and standards [29].

Irregularities of different size and shape cause roughness on a surface; the concavities/convexities affect the quality and functionality of the object's surface. Surface irregularities are measured by classifying the height/depth and intervals of surface features to evaluate their concavity/convexity [29]. One of the most efficient methods of measuring surface roughness at the nanoscale is the laser microscope, which provides an accurate, non-contact 3D surface roughness measurement of the surface features of a sample under ambient conditions.

The area method parameters that are used to evaluate the roughness of Nitinol specimens are as follows:

- (S_v) maximum pit depth: the maximum value for the valley's depth:

$$S_v = |\min(Z(x,y))|$$

(2. 2)

- (S_p) maximum peak height: the maximum value for the peak height:

$$S_p = \max(Z(x,y))$$

(2. 3)

- (S_z) maximum height: this parameter expands the profile parameter R_z three dimensionally and it is equivalent to the sum of the maximum peak height S_p and the maximum valley S_v

$$S_z = S_p + S_v$$

(2. 4)

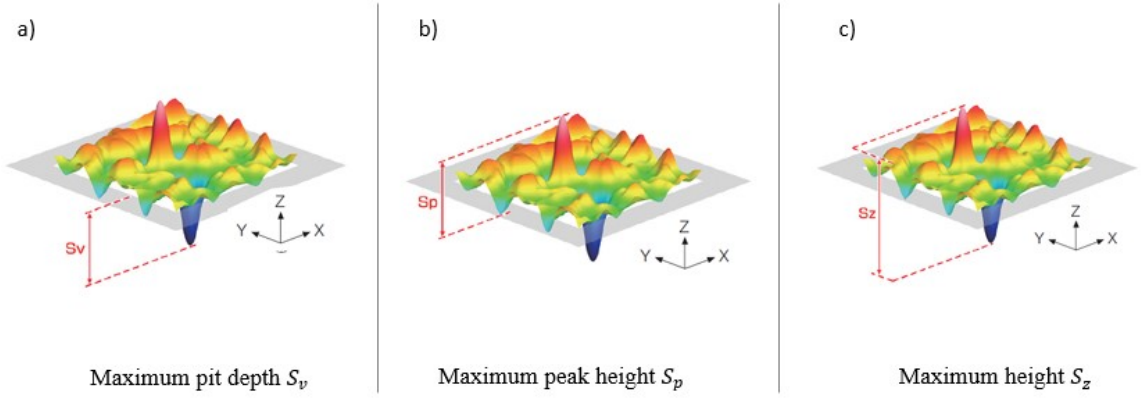

Figure 2. 10: S_v, S_p, S_z area method parameters [29]

- (S_a) arithmetical mean height: S_a expands the profile parameter R_a three dimensionally and represents the arithmetic mean of the absolute ordinate $Z(x,y)$ within the evaluation area. It is one of the most used parameters since it is not significantly influenced by scratches, contamination, and measurement noise.

$$S_a = \frac{1}{A} \iint_A |Z(x,y)| dxdy \tag{2. 5}$$

- (S_q) root mean square height (RMS): it represents the root mean square for $Z(x,y)$ within the evolution area. It corresponds to the standard deviation of the height distribution.

$$S_q = \sqrt{\frac{1}{A} \iint_A Z^2(x,y) dxdy} \tag{2. 6}$$

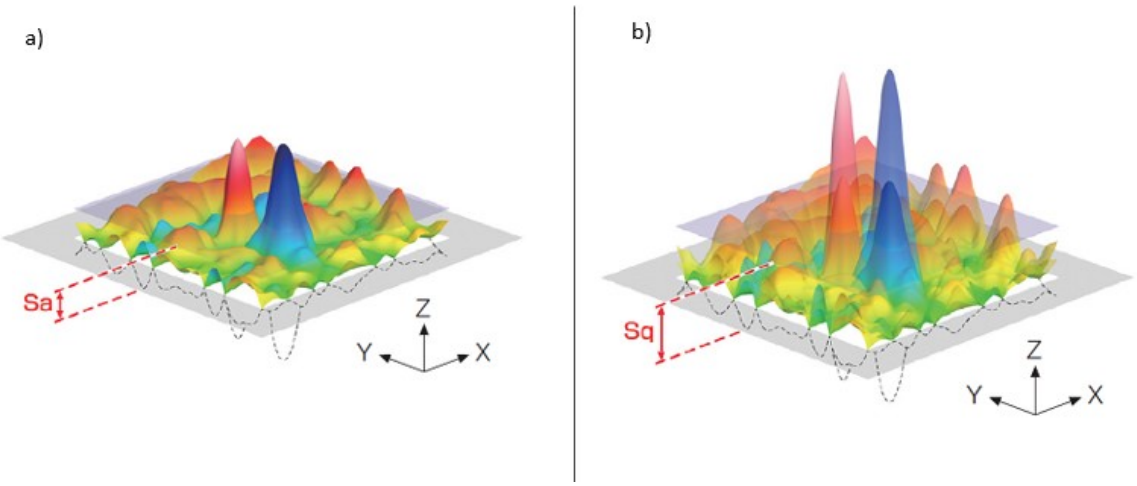

Figure 2. 11: S_a, S_q area method parameters [29]

2. 6 Nanoindentation

The unique smart properties of Nitinol include strain recovery as the most mention-worthy one. The martensitic transformation, triggered by variation in applied stress and thereby leading to strain recovery in SMA, is termed as super-elastic effect (SE).

The instrumented indentation technique (IIT) involves pressing an indenter of known geometry into the surface while both penetration depth and normal load are monitored.
IIT, which implements low load (in mN) and small displacement (in nm) of the indenter tip on specimen surface, is used to investigate certain localised material properties such as Young's modulus, hardness, and strain recovery. This is a great advantage compared to classical hardness measurement in which each imprint has to be precisely measured separately with an optical microscope.
This method has the potential to evaluate the martensitic transformation and super-elastic effect characteristics in the alloy, as well. Most of these investigations dealt with the local variation in hardness, elastic modulus, indentation depth, indentation impression, energy dissipation etc [17].
Data are obtained from one complete cycle of loading and unloading through load and depth sensing indentation technique. In fact, the shape of the entire unloading curve and the total amount of recovered displacement can be accurately related to the elastic modulus and the size of the contact impression [18].

2.6. 1 Oliver-Pharr method

The Oliver-Pharr method is the most frequently adopted method in instrumented indentation testing to probe the elastic modulus and microhardness of materials. The procedures and formulas of this method are shown below.
Effects of an indenter on the load-displacement behaviour can be accounted for by defining a reduced modulus, E_r, through the equation:

$$\frac{1}{E_r} = \frac{1-\nu^2}{E} + \frac{1-\nu^2}{E_i} \tag{2. 7}$$

where E and ν are Young's modulus and Poisson's ratio for the specimen and E_i and ν_i are the same parameters for the indenter.

E_r is also expressed as follow:

$$E_r = S\frac{\sqrt{\pi}}{2}\frac{1}{\sqrt{A}} \tag{2. 8}$$

Here, S is the experimentally measured stiffness of the upper portion of the unloading data, S is equal to the unloading slope $\left(\frac{dP}{dh}\right)$ owing to elastic recovery, E_r is the reduced modulus (previously defined), and A is the projected area of the elastic contact.

It should be noted that the contact stiffness S is measured only at peak load *(*see *Figure 2. 12)*.
The load-displacement relationships are nonlinear, and the contact area changes continuously during unloading. The area of contact at peak load is determined by the geometry of the indenter and the depth of contact, h_c.
At any time during loading the total displacement h is:

$$h = h_c + h_s \tag{2. 9}$$

where h_c is the depth of contact and it is the vertical distance along with contact is made, and h_s is the displacement of the surface at the perimeter of the contact. At peak load, the load is P_{max} and the displacement is h_{max}.

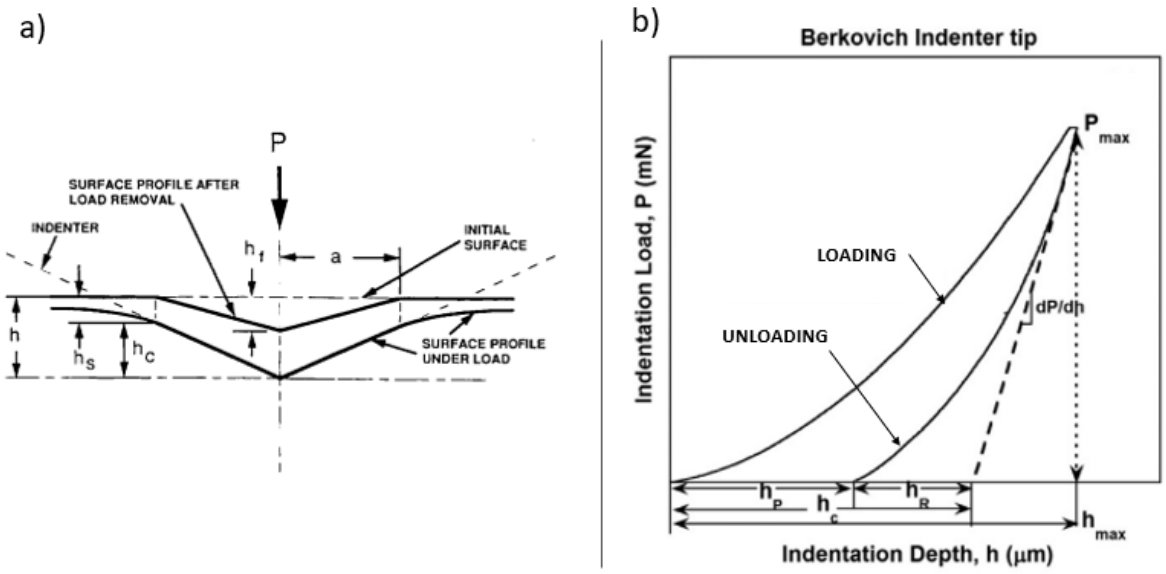

Figure 2. 12: a) section through an indentation showing various displacement[18]*, b) schematic representation of load versus indentation*[17].

When the indenter is fully withdrawn, the elastic displacement is recovered, and the depth of the final indentation is h_p, it is also known as the permanent depth *(*see *Figure 2. 12).*
The projected area of contact at peak load can be computed from the relation:

$$A = F(h_c) \tag{2. 10}$$

The functional form of F must be established experimentally prior to analysis. For this reason, an indenter area function calibration is very necessary before testing in order to account for several error sources such as tip rounding and indenter geometry defects [19].

Thus, the projected area function is fitted to a six-order polynomial form:

$$A_p = C_0 h_c^2 - C_1 h_p + C_2 h_c^{\frac{1}{2}} - C_3 h_c^{\frac{1}{4}} + C_4 h_c^{\frac{1}{8}} - C_5 h_c^{\frac{1}{16}} \tag{2. 11}$$

The deflection of the surface at the contact perimeter depends on the indenter geometry. For a conical indenter, h_s is expressed as follows:

$$h_s = \epsilon \frac{P_{max}}{S} \tag{2. 12}$$

where the geometric constant ϵ for the conical indenter is given by

$$\epsilon = \frac{2}{pi} (\pi - 2) \tag{2. 13}$$

therefore, it is possible to determine the contact depth from the experimental data, it is noted that

$$h_c = h_{max} - h_s \tag{2. 14}$$

In addition to the modulus, the data obtained using the current method can be used to determine the hardness, H (expressed in GPa). It is defined in terms of maximum load P_{max} and the projected area of contact A_p between indenter and sample at the maximum load:

$$H = \frac{P_{max}}{A_p} \tag{2. 15}$$

Super-elasticity of the alloy is better comprehended from nanoindentation, upon quantifying the degree of depth recoverability ratio, ψ, as per the following relation [17]:

$$\psi = \frac{h_{max} - h_p}{h_{max}} \tag{2. 16}$$

The work recovery ratio, μ, is another useful parameter for assessing the recoverable deformation capacity of NiTi. It is calculated as the ratio between the recoverable deformation energy, W_R, and the total one, W_{tot}:

$$\mu = \frac{W_R}{W_{tot}} \tag{2. 17}$$

2.6. 2 NiTi Resilience

Resilience is the ability of a material to recover its shape when the force is removed, allowing it to withstand relatively high local stresses without permanent damage.

The resilience of Nitinol is due to its properties of hardness, low elastic modulus and super-elasticity. High hardness values make the material resistant to permanent deformation, a low elastic modulus means that, following the application of a load, the material undergoes high elastic strain, and finally, super-elasticity allows the alloy to have a high recovery from elastic deformation.

Furthermore, the super-elasticity effect results in a non-linear elastic modulus causing Nitinol to have an even smaller "effective modulus"[9].

The high elastic strain due to relatively elastic modulus and super-elasticity of Nitinol results in an expanded contact area under a concentrated applied load and a consequent reduced peak Hertz stress (see paragraph *2.7. 2*) avoiding permanent deformation [9].

When talking about resilience, it is useful to combine the values of hardness and elastic modulus rather than considering them as separate data. For this reason, a new parameter is introduced, the MR Modell ratio [20], which is the ratio of material hardness to the corresponding modulus of elasticity. Modell gives an indication of the depth of penetration that a metal can tolerate without exceeding the elastic limit.

$$MR = \frac{H}{E} \tag{2. 18}$$

2. 7 Tribological mechanisms

2.7. 1 Defining Wear and Friction

Friction and wear can be defined as the responses of a tribo- system.

Friction is the resistance to the sliding of one solid body over or along another. Friction dissipates energy generating heat, thus impeding free movement at interfaces, and affecting the flow and deformation of materials in metalworking processes.

There are two commonly accepted theories of friction: adhesion and abrasion.

The adhesion theory claims that two dry and clean surfaces contact each other at only a fraction of their apparent contact area. In this way, only small asperities support the perpendicular contact force N. At the asperities, the stresses are therefore high and can cause plastic deformation at the junctions, forming an adhesive bond.

In the abrasive theory, it happens that the asperity of the harder material penetrates and *plows* the softer surface. This results in the removal of the surface material; therefore, small chips are created.

In both cases, a tangential force F is required to shear the junctions and slide the two bodies in contact. The ratio between F and N (F/N) is called *coefficient of friction, μ.* The value of μ depends on the materials and process involved.

Almost all the energy dissipated in overcoming friction is converted into heat, which raises the surface temperature.

Wear generates continuous material loss due to various types of microscopic material removal mechanism, causing material to leave the surface as debris. Wear generally alters a part's surface topography and may result in severe surface damage.

As for friction, also for wear there are different basic mechanisms: adhesive, abrasive, and fatigue wear.

In the adhesive wear, bonds form at the asperity junctions and they often are stronger than the base metals themselves. The wear fragments generate because the fracture follow a path in the softer material. Thus, the fragment is attached to the harder component, and it eventually detached during further sliding developing a loose wear particle.

Abrasive wear is generated by a hard, rough surface or a surface containing hard particles, sliding across another surface producing microchips and leaving scratches on the other material.

Fatigue wear or surface fatigue is caused by a cyclic loading such as rolling contact in bearings. The wear particles are usually formed through the mechanism of spalling or pitting.

As in many situations, various types of wear take place in different locations. The surface topography is the result of the combination of the wear mechanisms explained above.

The wear resistance of pure metals has been found to be directly proportional to their hardness. Classical wear theories, such as Archad's theory, consider hardness one of the main factors playing a role in the wear characteristics. Archad's law states that the volume V of worn material is proportional to the normal force, N, the sliding distance, s, and inversely proportional to the hardness of the material, H.

$$V = k_{adh}\frac{Ns}{H} \tag{2. 19}$$

k_{adh} is a constant, the so-called adhesive wear coefficient.

Thus, wear can be reduced by increasing the hardness of materials by heat treatment or reducing the normal load. Elastomers and rubbers resist abrasive wear very well because they deform elastically, and they recover when abrasive particles cross past over their surfaces.
It can be concluded that the super-elastic property of Nitinol plays a key role in wear resistance.

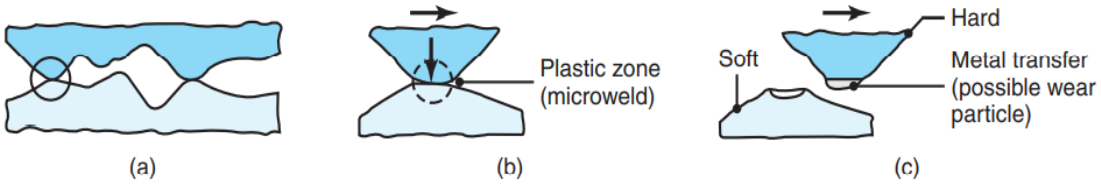

Figure 2. 13: (a) two contacting asperities, (b) adhesion between two asperities, and (c) the formation of a wear particle [13].

2.7. 2 Hertzian contact

The real area of contact comprises several individual areas. In many experiments, crossed cylinders or a sphere pressed against a flat are used. It is then assumed that the total area of contact is confined to a single circular area [21]
When two solid surfaces are loaded together there always be some deformations. They may be purely elastic or may involve some additional plastic, and so permanent, changes in shape.
Let now consider two curved bodies of different radii of curvature. When they are bought into contact, they will initially touch at either a point or along a line. With the application of a load, elastic deformation enlarges these into contact areas across which the loads are distributed as pressures [22].

In 1881 Heinrich Hertz presented the first analysis of this situation which is based on the following assumptions:

a. The surfaces are continuous, smooth, nonconforming, and frictionless.

b. The size of the contact area is small compared to the size of the bodies.

c. Each solid can be considered to behave as an elastic half- space in the vicinity of the contact zone.

d. The gap, h, between the undeformed surfaces can be approximated by the following expression.

$$h = Ax^2 + By^2 \tag{2. 20}$$

where x and y are orthogonal coordinates lying in the common tangent plane to the two surfaces. Thus, expression (2.20) requires parabolic surface profiles.

If two elastic sphere 1 and 2 of radii R_1 and R_2 are pressed into contact with force F_z, then the resultant circular contact area has radius a such that

$$a = \left(\frac{3F_z R}{4E}\right)^{\frac{1}{3}} \tag{2. 21}$$

where E is the contact modulus defined by

$$\frac{1}{E} = \frac{1-\nu_1^2}{E_1} + \frac{1-\nu_2^2}{E_2} \tag{2. 22}$$

E_1, E_2 are the elastic modulus, ν_1, ν_2 the Poisson's Ratio of the body 1 and 2 respectively.
R is the reduced radius, and it is correlated with those of the individual component by the expression

$$\frac{1}{R} = \frac{1}{R_1} + \frac{1}{R_2} \tag{2. 23}$$

If one of the two loaded solid is a plane, then the reduced radius is numerically equal to that of the opposing sphere ($R = R_1$) and the radius of the plane surface becomes infinite ($R_2 = \infty$).

The resulting pressure distribution $p(r)$ is semi-elliptical, as in Figure 2, and the expression is

$$p(r) = p_0\left(1 - \frac{r^2}{a^2}\right)^{\frac{1}{2}} \; where \; r^2 = x^2 + y^2$$

(2. 24)

The maximum pressure, known as the Hertz stress, is p_0, and it occurs on the axis of symmetry

$$p_0 = \frac{3F_z}{2\pi a^2} = \frac{3}{2}P_m$$

(2. 25)

P_m is the mean pressure.

The centres of the two spheres move together by a small displacement Δ given by

$$\Delta = \frac{a^2}{R} = \frac{a\pi p_0}{2E} = \left(\frac{9F_z^2}{16RE^2}\right)^{\frac{1}{3}}$$

(2. 26)

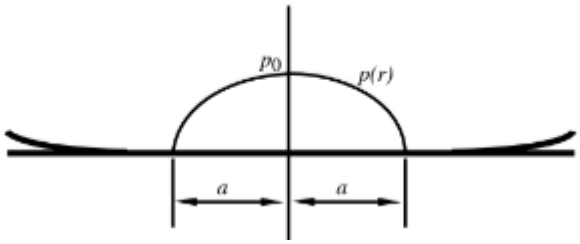

Figure 2. 14: resulting semi elliptical pressure distribution [22]

2.7. 3 Tribotest

In this study, the purpose of tribotesting is to increase the fundamental and general understanding of how a material behaves in tribological applications. Thus, Nitinol is characterized in terms of wear resistance, friction properties and types of surface damage. The purpose of this scientific procedure is to evaluate the tribological applications of a new material. However, it is not always possible to obtain high degree of realism in the tests, thus the interpretation of the results becomes a relevant part of the analysis.

Another important part of tribotesting is the use of reference materials since tribological properties are comparative parameters. For this reason, a comparison between Nitinol and a common bearing steel will be reported below to gain knowledge about the tribological mechanism.

Evaluation of the wear process is one of the main aspects of tribotesting. A used technique to evaluate wear is weighting and measurement of changes in dimensions. Weighting may often be difficult if the worn volumes are small compared to the weight of the component.
Therefore, the study of worn surfaces, for example with microscopy or surface topography techniques, becomes an integral part of the evaluation procedure. For example, to provide information about the depth of the damage, it is recommended the study of the worn surface in cross-section.
In situations of mild wear, the mass loss is often very small in relation to the total mass of the worn component. A precision balance typically has a resolution of 0.1 mg at 100 g load. Often this excludes the weighting of component before and after wear testing as a method to quantify wear.
With the introduction of high-resolution instruments such as optical interferometry, it is now possible to store and obtain topographical data digitally and to measure the volume of topographical features in the sub μm^3 range.

To evaluate the tribological properties of NiTi alloy a pin-on-disk configuration was used. This type of test is representative of both *abrasion wear* and *wear in sliding contact.*
The most studied wear mechanism is pure abrasion, which is grooving by hard particles or hard asperities on a countersurface. In pure abrasion there is a linearity between wear volume and sliding distance. It is also observed a proportionality between abrasive wear resistance and indentation hardness.
Sliding wear do not specify any wear mechanisms but refers to the types of contact between two surfaces in relative motions. Adhesion or surface fatigue are common surface damages but also grooving by surface asperities is possible. Nevertheless, wear and friction in sliding contacts are of great interests because of their common occurrence. Several sliding wear test configurations are specified in national standards. For this specific study, the pin-on-disk standard (ASTM G99) has been consulted.
Sliding in combination with abrasive particles is the major driver of abrasive wear in bearings [23].

CHAPTER 3

NiTi APPLICATION

3. 1 NiTi application: Space Bearing

One of the fundamental steps of this research work was to find the application that could best represent the properties of the Ni-rich (50.8 at. % Ni, 49.2 at. % Ti) NiTi alloy and the process chain developed.

The main factors guiding application selection were:

- The shape of the object: it had to be obtained by turning. This led to the exclusion of filiform and non-axisymmetric objects.
- Exploiting the super-elastic property of the material: the martensitic transformation of the NiTi alloy occurs by applying a load and not by changing the temperature (shape memory).

The aerospace sector is the best candidate as it requires the use of materials that can withstand high loads, thus taking full advantage of the super-elastic property.

Spacecraft experience violent (shaking) and sustained (acceleration) initial forces during launch.

The launch mechanical environment involves [24] :

- Steady state accelerations: quasi static loading means under steady state accelerations. Usually, the quasi static load are equivalent to static loads.
- Low frequency vibrations
- Broad band vibrations (random vibrations and acoustic loads): they are produced by engines functioning and the aerodynamic turbulent boundary layer.
- Shocks: caused by the actuation of pyrotechnic devices used by the release mechanism for stage and satellite separation, solar arrays deployment etc.

In addition, a satellite in space is subject to different external forces, causing friction, gravitational and magnetic effects as well as particle pressure from solar wind (photons, protons, etc.).

Thus, some typical requirements for spacecraft structures are strength, stiffness, structural life, structural response, damping, etc.

Inside space mechanism, the contacts between balls and races in ball bearings are a primary vulnerability for launch load damage [1]. Bearing systems must be designed with the intent of achieving optimally low mass and (usually) high stiffness, high reliability, and the capability to sustain launch vibration-induced loads without damage or degradation.[25] Spacecrafts make use of bearings for a wide variety of systems such as deployment mechanisms, pointing gimbals and flywheels used in gyroscope and reaction wheels. The bearing race can be subjected to high static loads causing damage due to indentation. These phenomena can occur during launch where the bearing may not run smoothly and may fail prematurely.

In such cases, one of the methods used by bearing designers to eliminate or mitigate the occurrence of damage is to replace the conventional bearing material with a better performing one.

Aerospace bearing goals are:

- Lighter weight materials
- Use of corrosion proof components considering the extreme environments
- Hardness
- Wear resistant and compatibility with existing lubricants.
- Fracture resistant
- Capable of producing ultra-smooth surface finishes

Materials commonly used in bearings are steels such as M50 and 52100 known for their high hardness, easy machining and good tribological properties, but they are also susceptible to corrosion, highly magnetic and have a high density. Stainless steels such as 440C are also commonly used in bearings, since they are very high-performance materials but have the disadvantage of rusting and they are also highly magnetic. Silicon nitride ceramics (Si_3N_4) are widely used as bearing materials because of their corrosion resistance, light weight, high hardness, and ability to withstand high speeds. However, they are electrical insulators and have high processing costs.

Dr Christopher DellaCorte (Senior Technologist, Tribology & Rotating Machinery, NASA) was one of the first researchers to develop bearings and gears made from 60NiTi (60wt%Ni, 40wt%Ti), showing that these alloys are immune to atmospheric corrosion (rust) and can withstand impact loads, making them valid replacements for conventional materials.

The following table (*Table 3.1*) shows the parameter values of NiTi-60 and NiTi-55 obtained from tests carried out by DellaCorte and compared with those of M-50 steel.

Property	NiTi-60	NiTi-55	M-50
Density	6.7 g/cm^3	6.5 g/cm^3	8.0 g/cm^3
Hardness	56-62 Rc	35-40 Rc	60-65 Rc
Magnetic	NON	NON	Magnetic
Corrosion Resistance	Excellent	Excellent	Poor
Young's Modulus	~114 GPa	~100 GPa	~210 GPa
Maximum Use Temp.	~400° C	~400° C	~400° C
Electrical Resistivity	~80 x 10^{-6} Ωcm	~80 x 10^{-6} Ωcm	~60 x 10^{-6} Ωcm

Table 3.1: nominal comparative properties for conventional bearing steel M-50, NiTi55 and NiTi60 [1]

As can be seen from the table, Nitinol has a high Modell ratio H/E due to its relatively high hardness values and low elastic modulus resulting in high resistance to concentrated contact damage. Mass is also minimised as the density of NiTi is lower than that of steel.

In previous research[26] , several tests and experiments were carried out to investigate the super-elasticity and hardness of 60NiTi and to meet the requirement for a material with good tribological properties. It is worth mentioning a test that compared a 60NiTi ball with a 440C ball rolling against a 440C plate. The test showed that the coefficient of friction of 60NiTi was lower than that of 440C (see *Figure 3. 1*). This result is not fully understood, but it is thought that the Nitinol ball returns lower coefficients of friction due to its super-elastic properties. Therefore, the elastic deformation of the surface in contact with the plate is better recovered by the Nitinol ball than by the steel ball. Based upon these considerations, lower friction, and higher overall efficiency of NiTi bearings may be expected. The advantage of materials such as Nitinol lies in its ability to deform and withstand high levels of recoverable strain; in fact, when a load is applied, this alloy is able to deform elastically, creating a relatively large contact area, so that the stress is more distributed reducing change for permanent damage. It was also discovered that highly recoverable materials can better withstand debris-induced damage [26].

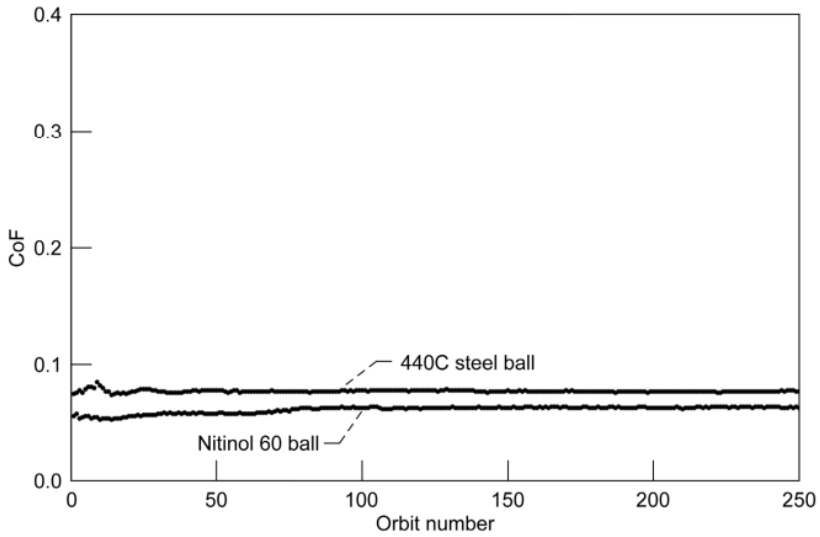

Figure 3. 1: coefficient of friction of a 440C steel ball and a 60NiTi ball rolling against 440C. Both balls have been lubricated [26]

In the various tribological tests carried out by DellaCorte, different combinations of materials have been examined for the ball-race pair. The following figure *(Figure 3. 2*) evaluates the indentation of Si_3N_4 or 60NiTi balls with plates made of Stellite68, 440C, M50 and 60NiTi. The figure therefore shows the clear advantages of using 60NiTi for both the ball and the race (simulated by plates) in terms of improved load tolerance and corrosion resistance (no rust).

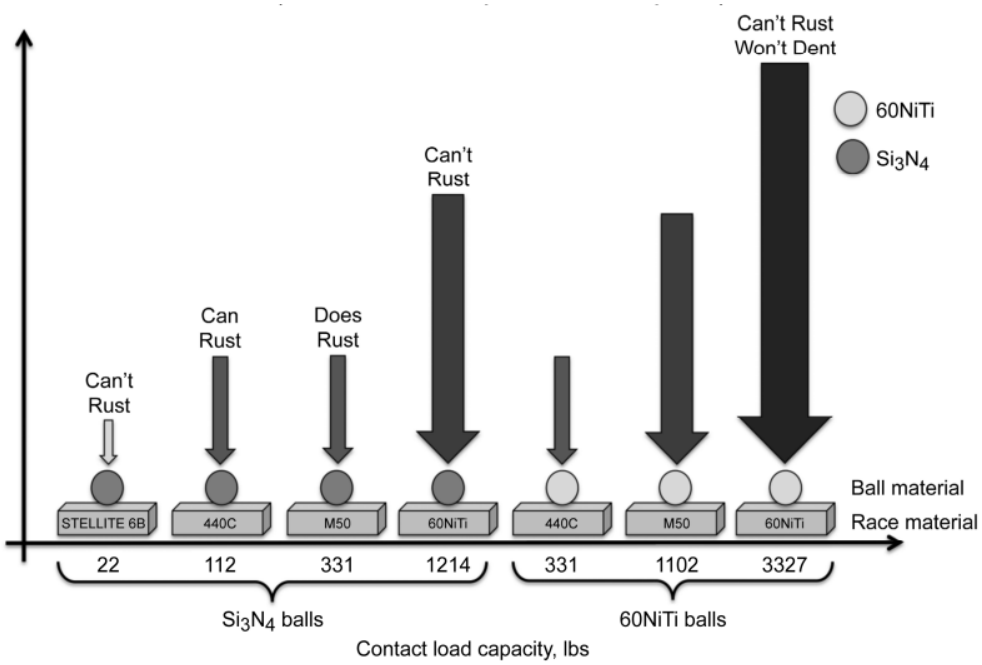

Figure 3. 2: indentation load tolerance of various bearing material combinations [26]

Through a series of conventional and unconventional materials tests (hardness test, Brinell test, rolling contact fatigue test, tribology test, compression test, etc.), DelleCorte shows that [26]:

- The use of super-elastic materials with a high degree of hardness and a relatively low modulus of elasticity results in increased contact load capacity.
- A larger Hertzian contact area is achieved by using materials such as 60NiTi, which have a high degree of recoverable deformation under high contact loads. This reduces peak and average stress as the contact load is spread.
- Several tests show that Nitinol is a good candidate for improving the performance of machine components.

3. 2 Using bearings in spacecraft reaction wheels

Reaction wheels are an example of the use of bearings on a satellite. They are used for stabilised attitude control of spacecraft, as precise orientation is required to allow the proper operation of the satellite and its payload (directional antennas, telescopes, etc.). Simplified reaction wheels are flywheels that are supported by ball bearings and driven by an electrical motor. By adding or removing energy from the flywheel, torque is applied to a single axis of the spacecraft, causing to react by rotating. Several reaction wheels can be used to provide full three-axis attitude control and stability.

DellaCorte et al.[] evaluated the launch load tolerance of a 5kg reaction wheel assembly (RWA) using four R4 bearings where a limiting contact stress is applied to the ball-race contact (see *Figure 3. 3*Figure 3. 3 *)*. The materials 60NiTi, 440C and REX20 of the different bearings were evaluated. For each ball-race configuration differing in the material used, the individual ball-race load limit (N) was measured and consequently the limiting contact stress (GPa) was calculated through the Hertz theory.

To determine the radial load capacity of bearing R4 as a function of the capacity of each ball race, the relationship given by Derner and Pfaffenberger was used:

$$F_R = \frac{9N_{max}}{5} \tag{3.1}$$

Where F_r is the bearing load capacity, N_{max} is the single ball load capacity. Finally, since two pairs of bearings are used, multiply F_r by four to find the load capacity of the entire reaction wheel.

The test showed that conventional materials such as 440C and Si3N4 (whether used as a ball or disc) have RWA load values close to the g-forces required to withstand the launch (approximately 20 g)

with the addition of margin. The use of materials such as REX20 greatly increases the load capacity of the reaction wheel (approx. 90 g).

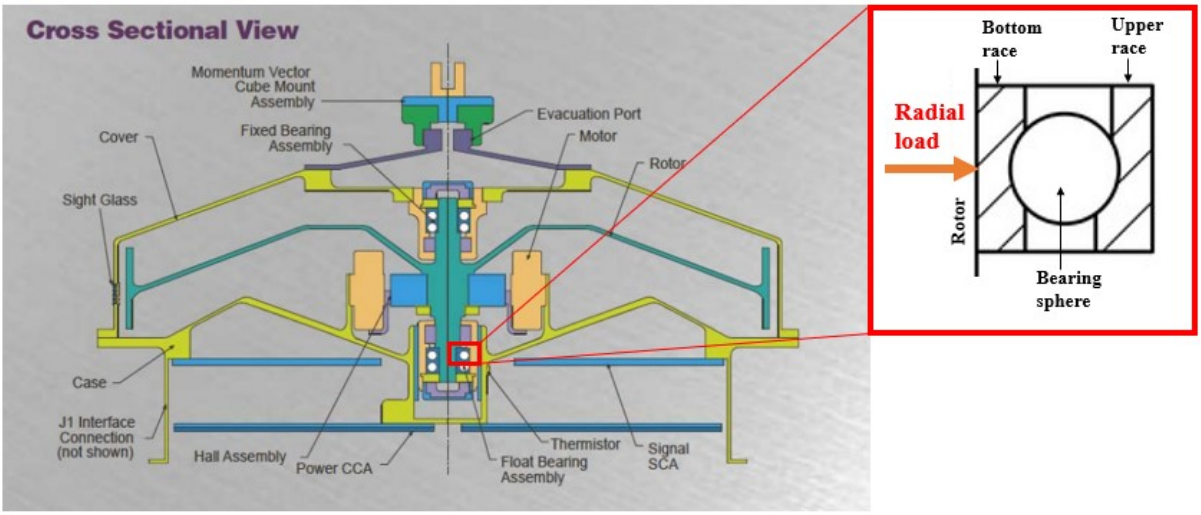

Figure 3. 3: typical reaction wheel assembly based upon Honeywell Corporation Model HR0610 Design [1] *. The two bearing pairs and the detail of the ball-race under radial load are shown.*

Even better is the combination of 60NiTi for both the ball and the disc. On the other hand, if 60NiTi is used only for the ball or disc, the RWA load capacity values are comparable to or lower than those of REX20. For example, using the Nitinol ball and 440C disc, an RWA load of approximately 68g was calculated. DellaCorte concludes that the use of 60NiTi will always lead to an improvement in load capacity compared to the use of conventional materials. This translates into the possibility of improving mechanical performance and possibly reducing the number of bearings.

The example of the reaction wheel test carried out by DellaCorte is intended to show how some studies on the 60NiTi alloy have indeed demonstrated the great potential of this alloy and how, thanks to its properties, it is even better than the best known and most widely used materials.
However, it should be noted that the present study uses a NiTi alloy with a different chemical composition (50.8 at%.Ni, 49.2 at%.Ti), which is more comparable to 55NiTi. Therefore, the properties and results are expected to be different from those of 60 NiTi. Previous tribological studies carried out on 60NiTi show the importance of this type of test to validate and analyse the NiTi properties, showing the potential use of this material in applications such as reaction wheels.
The tribological tests conducted in this study, which will be presented below, do not aim to make a comparison with other materials, unlike the tests carried out by DellaCorte; rather, the focus of this research is to compare Nitinol samples with different process parameters to validate the manufacturing process that gives better results in terms of wear resistance, work recovery ratio, hardness, elastic modulus etc.

CHAPTER 4

THESIS PATTERN

4. 1 Thesis pattern: Manufacturing Process Chain

The scheme of the manufacturing process chain is shown. This scheme is intended to help the reader follow the various processes described below in the Materials and Methods and Results sections.

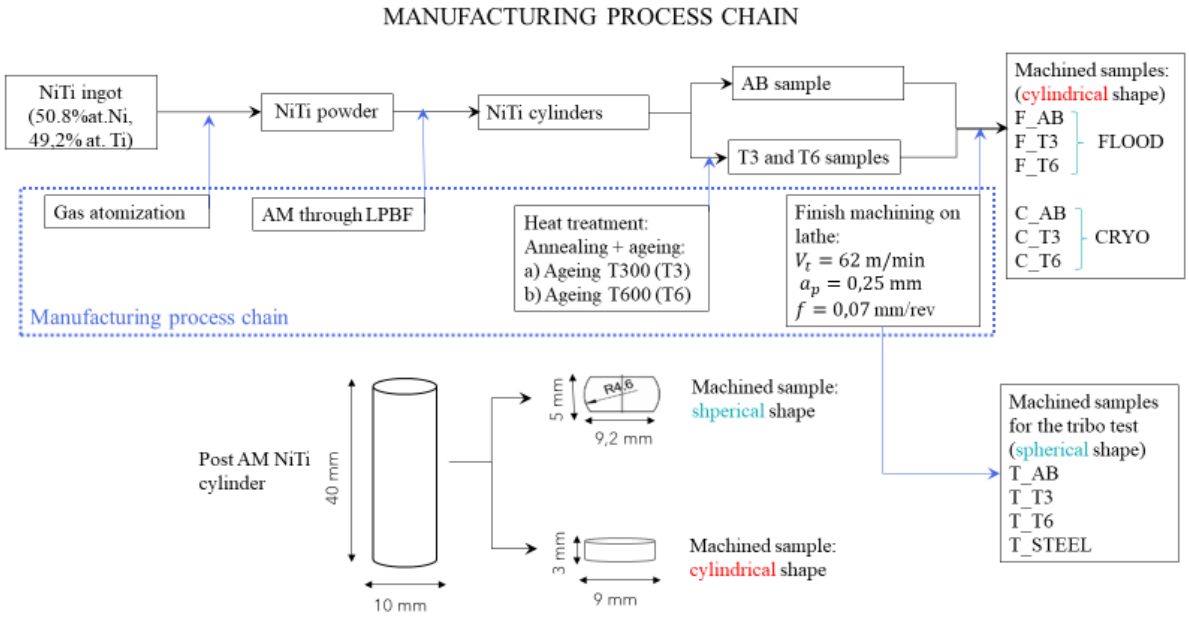

Figure 4. 1: Manufacturing process chain scheme.

4. 2 Thesis pattern: NiTi Testing

The diagram shows the tests carried out on the samples obtained from the manufacturing process chain. The different types of analyses and their purpose are indicated.

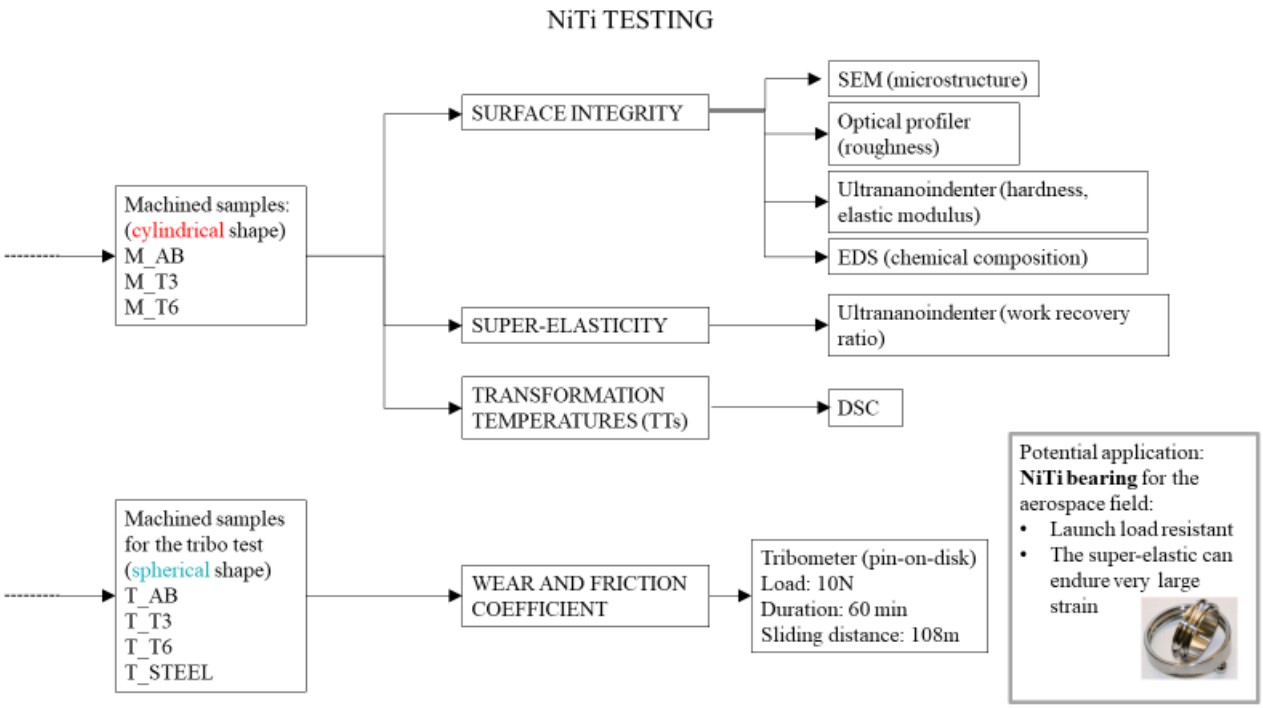

Figure 4. 2: NiTi testing scheme.

CHAPTER 5

EXPERIMENTAL PROCEDURE

5. 1 NiTi Powder

The $Ni_{50.8}Ti_{49.2}$ (at%) pre alloyed spherical powder was produced by gas atomization (ECKART TLS ™) of as-cast ingot. Particle size was ranged between 15 μm and 45 μm. Level of impurities in powder particles is presented in the following table:

Ch. Composition	Carbon (wt%)	Oxygen (wt%)	Nitrogen (wt%)
$Ni_{50.8}Ti_{49.2}$	0.005	0.028	0.001

Table 5. 1: Nitinol powder impurity level

5. 2 Additive Manufacturing

The near- net- shape Nitinol parts were fabricated through the laser powder bed fusion (LPBF) technique where a high-power laser directly melts selected area of powder to manufacture objects layer by layer and with good accuracy.

As mentioned above, the preparation of the specimens by AM and the related decisions have been carried out in a previous work [3]. Therefore, the process parameters are simply given below.

The starting point for the LPBF process is a three-dimensional CAD model of the part and the 3mm thick block support structure used to secure the part to the platform and improve thermal conduction. The support generation and slicing in horizontal layers of defined thickness were performed using a Sisma MYSINT™ 100 machine. Chessboard meander hatch was utilized as scanning strategy to obtain a homogeneous distribution of residual stresses after LPBF.

In this work a laser spot of 30 μm was used. The work carried out by S. Khademzadeh [3] evaluates various process parameters including laser power (P), scanning speed (V) and hatch distances (dH). For the samples used in this project, those parameters were adopted that ensure a high density and austenitic phase at room temperature to ensure super-elasticity.

LPBF parameters optimized for Ni-rich NiTi are shown below:

Power P (W)	**Scanning Speed V (mm/s)**	**Hatch distance d_h (mm)**	**Layer thickness t (mm)**	**Input energy density E (J/mm^3)**	**Oxygen level (ppm)**
70	1100	0.06	0.025	42.42	<200

Table 5. 2: LPBF parameters

Cylinders of 10 mm diameter and 40 mm height were printed vertically, namely with the axis parallel to the building direction (BD) and then mechanically removed from the block support.

Figure 5. 1: Sisma MYSINT™ 100 machine (left), NiTi cylinders on the platform (right)

5. 3 Heat Treatment

A Carbolite Gero™ CWF 1200 furnace was used to perform the heat treatments.
It was necessary to set a target temperature a few degrees higher than the temperature selected for the treatment, as a normal temperature drop is to be expected due to the opening of the oven door. Once the set temperature is reached, it is maintained for the duration of the treatment. The nitinol cylinder is placed in the chamber in a horizontal position and, in the case of annealing, argon was introduced into the chamber during treatment to ensure an inert atmosphere. The furnace is then closed, and the cylinder removed at the end of the scheduled heat treatment time and cooled according to the method specified in the following tables. Temperature is monitored thanks to a 3 mm thermocouple gland through the centre of the door.

The heat treatment of the cylinders consists of two stages:

1. stress relief annealing (common for all samples).
2. ageing (which differs between samples aged at 300°C and 600°C).

The parameters of the two different heat treatments are shown below:

Stress relief annealing			
Treatment Temperature T (°C)	**Treatment duration t (h)**	**Inert atmosphere**	**Cooling system**
1060	1	Yes using argon	Water

Table 5. 3: stress relief annealing parameters to which all treated samples are subjected.

Ageing-300			
Treatment Temperature T (°C)	**Treatment duration t (h)**	**Inert atmosphere**	**Cooling system**
300	3	No	Air

Table 5. 4: ageing 300, procedure that only concerns samples to be aged at 300°C.

Ageing-600			
Treatment Temperature T (°C)	**Treatment duration t (h)**	**Inert atmosphere**	**Cooling system**
600	3	No	Air

Table 5. 5: ageing 600, procedure that only concerns samples to be aged at 600°C.

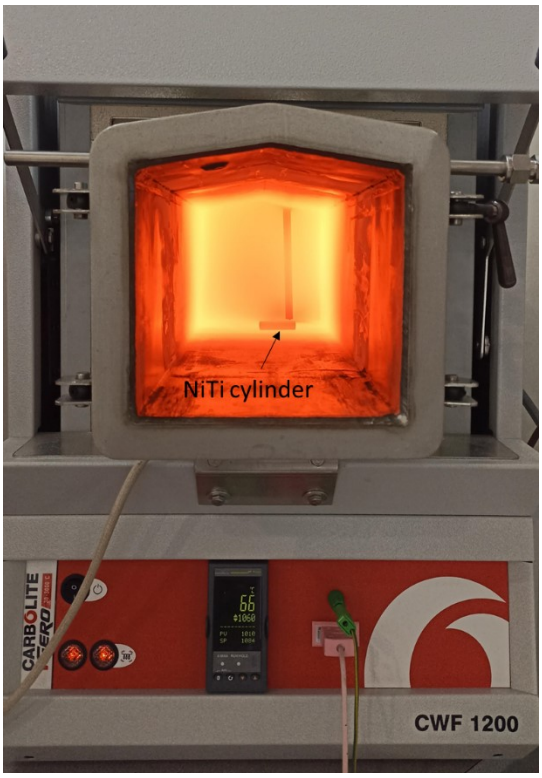

Figure 5. 2: Carbolite Gero™ CWF 1200 furnace with the door open and the Nitinol cylinder inside

5. 4 Lathe

The samples were longitudinally turned on a Mori Seiki™ NL1500 lathe using VCEX 110301L-F 1125 inserts.

It is a CNC lathe, which means that movement and control of the machine tool and its components are achieved by computer numerical control. It is also equipped with a turret with 12 tool stations to perform several operations.

It is recalled that specimens to be turned have a diameter of 10 mm and a height of 40 mm.

Machining on the lathe consists of three stages:

1) roughing: the final diameter of the sample after roughing is 9.5 mm

2) finishing: the final diameter of the sample after finishing is 9 mm

3) cutting off: the sample is cut from the original cylinder. The cut is made at 3 mm from the end face of the cylinder.

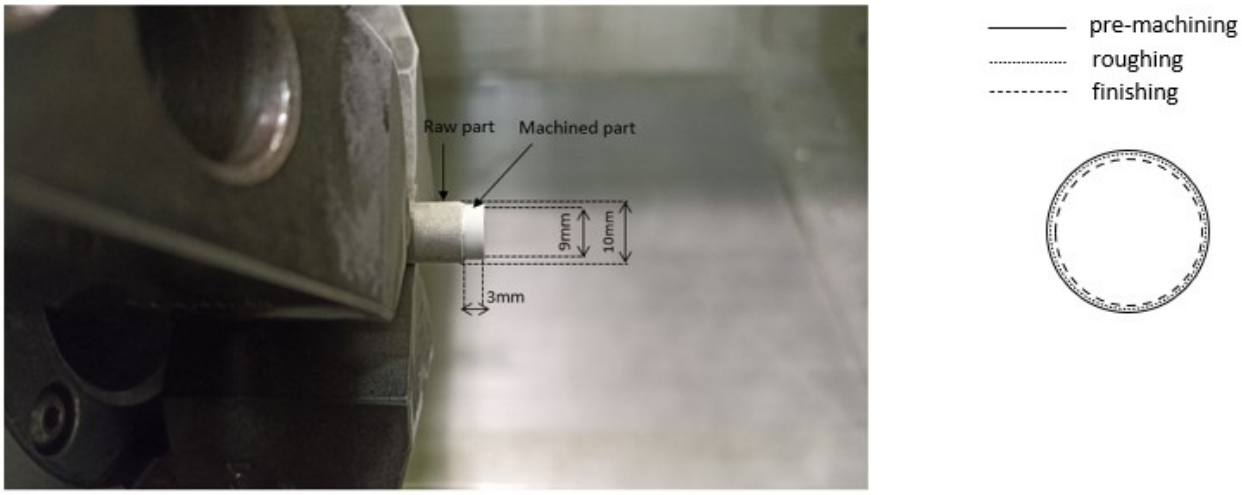

Figure 5. 3: Sample inserted in the lathe jaws, dimensions of machined and raw part are shown (left), the three situations of pre-machining, roughing, and finishing are shown in the cylindrical sample section (right).

Figure 5. 3 shows the sample placed in the lathe jaws. The right-hand end of the specimen was roughed and finished, while the rest of the specimen was left unfinished (raw part). The 3mm long piece is ready to be cut off. Cutting off involves subtracting 2mm of material from the unmachined part.

Cutting parameters for machining NiTi, that are shown below, are suggested for difficult to cut alloys.

	Initial diameter D_0 (mm)	**Final diameter D_f (mm)**	**Depth of cut a_p (mm)**	**Cutting speed V_c (m/min)**	**Feed f (mm/rev)**
Roughing	10	9.5	0.25	62	0.07
Finishing	9.5	9	0.25	62	0.07

Table 5. 6: cutting parameters in rough and finish machining.

Specimens were obtained by both flood and cryogenic machining.
Lubrication was manually activated and consisted of a high-pressure jet of cooling lubricant directed at the tool chest through a nozzle. The coolant was a water-based fluid containing 5% semi-synthetic oil.

Cryogenic machining uses the same process and cutting parameters as flood machining. In this case, the coolant is liquid nitrogen LN_2, which is sprayed onto the tool through copper tubes. The nitrogen is stored in a Dewar container at a pressure of 15 bar. The liquid nitrogen is passed through a coil where the liquid heats up and evaporates. This allows the nitrogen to be extracted in gaseous form and conveyed into a metal hose that terminates at the nozzles mounted on the lathe turret.

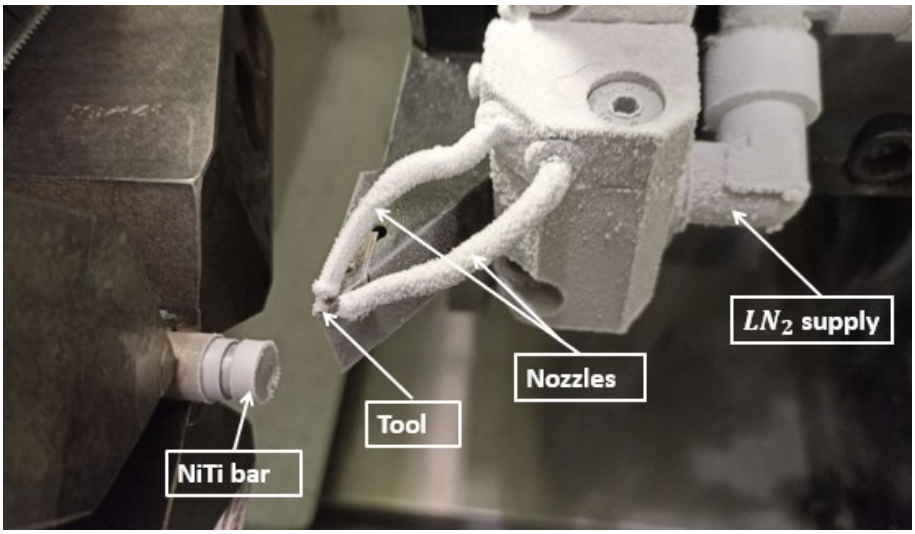

Figure 5. 4: cryogenic machining setup

At the end of the turning process, six different types of specimens were obtained. Their characteristics are shown in the following table.

N°	Specimens	Annealed	Aged	Cooling Machined Conditions
1	**F_AB**	NO	NO	FLOOD
2	**F_T3**	YES	YES at 300°C	FLOOD
3	**F_T6**	YES	YES at 600°C	FLOOD
4	**C_AB**	NO	NO	CRYO
5	**C_T3**	YES	YES at 300°C	CRYO
6	**C_T6**	YES	YES at 600°C	CRYO

Table 5. 7: Identification of the six flood and cryogenic samples

5.4. 1. Insert

As the material to be machined is composed of nickel and titanium, the choice of a tool suitable for turning this alloy ends with the VCEX 110301L-F 1125 insert. In fact, these inserts are suitable for machining ISO S class materials, which are iron, nickel, cobalt, and titanium base materials.
The main features of this type of insert are as follows:

VCEX 11 03 01L-F 1125 insert	
Cutting edge count	2
Corner Radius	0.1 mm
Clearance angle major	7°
Substrate	HC
Coating	PVD TiAlN + TiAlN

Table 5. 8: VCEX 11 03 01L-F 1125 insert characteristics.

Figure 5. 5: Sandvik Coromant ™ VCEX 11 03 01L-F 1125 insert

5. 5 Roughness Measurements

A *Sensofar Metrology™ S Neox* 3D profilometer was used for the roughness measurements at the Te.Si laboratory in Rovigo. The profilometer is supported by a computer with *SensoSCAN* software from *Sensofar Metrology™*. The *Nikon™ TU Plan Flour EPI* 20x lens was used for analysis.

The test specimens obtained by turning (length 3 mm and diameter 9 mm) were washed in an ultrasonic bath with 99% ethanol and dried with a hairdryer. They were then placed in a vice, which acts as a support since the specimens are cylindrical in shape. In this way, the side of the specimen that has been machined is placed directly under the lens of the profilometer.

An attempt was made to analyse an area that was in the centre of the machined surface so as to avoid edges that may be subject to burr residue from turning. The dimensions of the area to be captured are multiples of a base area of 0.88mm x 0.65mm. It was decided to scan an area equal to two base areas with a 5% overlap, so the acquired area has dimensions of 1.66mm x 0.65mm.
The scan is preceded by a series of steps such as focusing the sample and evaluating the scan area in Z, which must include the deepest valley and the highest peak. The scan is then started in *confocal* mode. At the end of the acquisition, it is verified that the scanned area is complete and positioned in the desired zone.

Sesofar Metrology's sensoVIEW software was used to study the 3D measurements, as it provides a comprehensive set of tools. The different steps in which the software tools are used are shown below:

- Raw acquisition (see *Figure 5. 6*)
- Crop (see *Figure 5. 7*)
- Form removal: Plane (see *Figure 5. 8*)
- Form removal: Polynomial 3D (see *Figure 5. 9*)
- ISO 2517 (see *Figure 5. 10*)

Sample C_V62 roughness measurement was taken as an example to show the various steps.

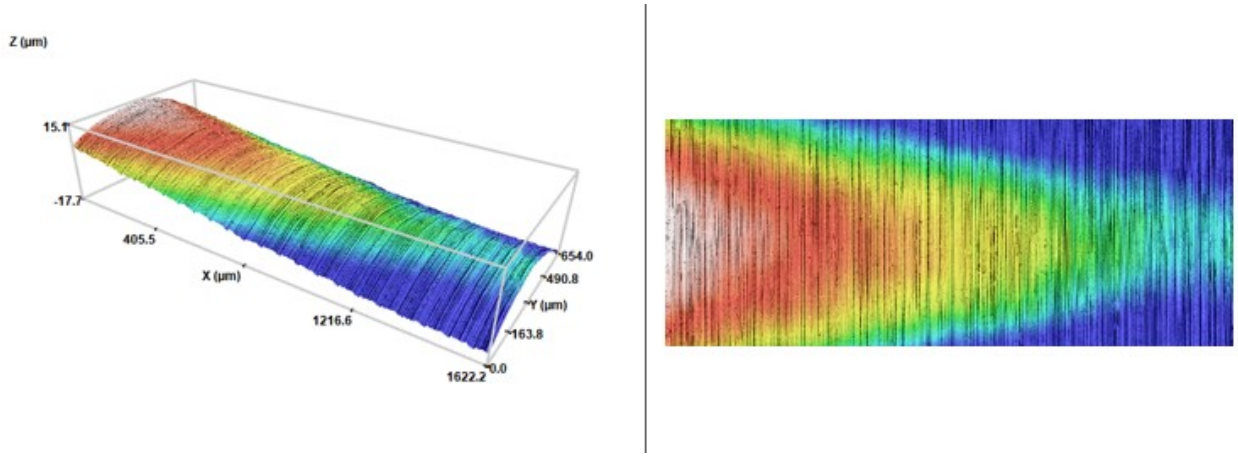

Figure 5. 6: raw acquisition: 3D view (left), 2D view (right)

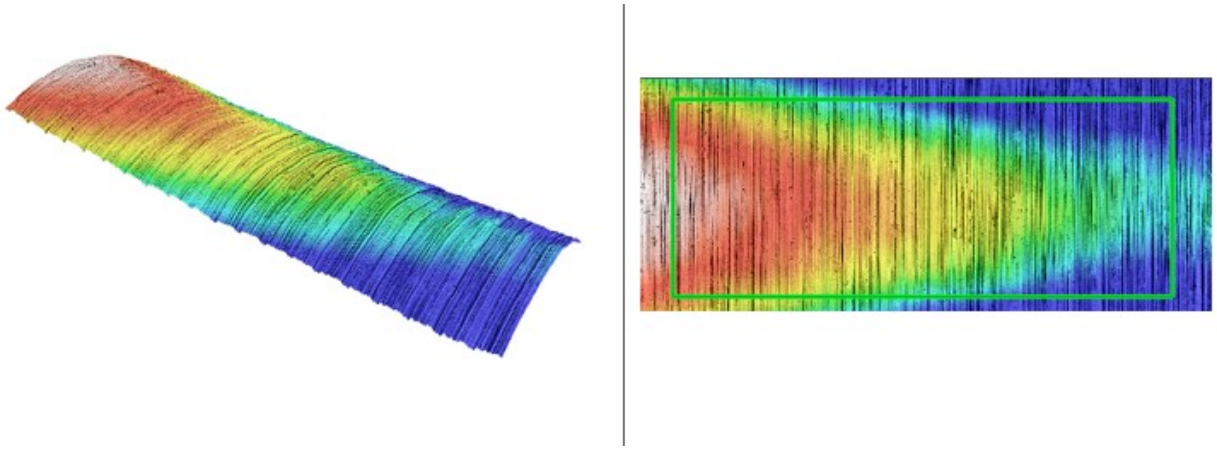

Figure 5. 7: crop: 3D view (left), 2D view (right)

An area of 1400µm x 550µm was cropped so that only the central part of the curved surface of the sample was considered, excluding more peripheral areas that could alter the final roughness measurement.

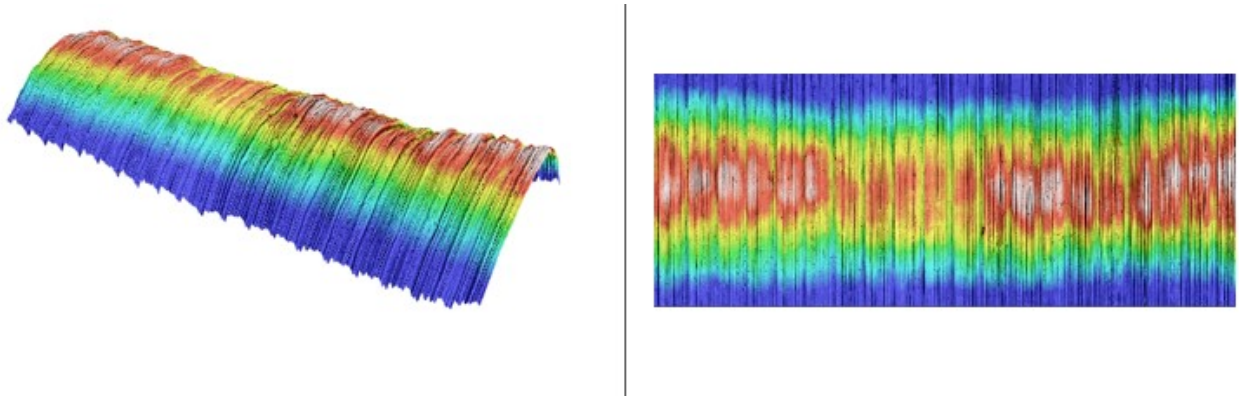

Figure 5. 8: Form Removal Plane, 3D view (left), 2D view (right)

The *Form Removal Plane* function is used to place the surface in a single plane to rectify any errors in positioning the specimen under the profilometer lens.

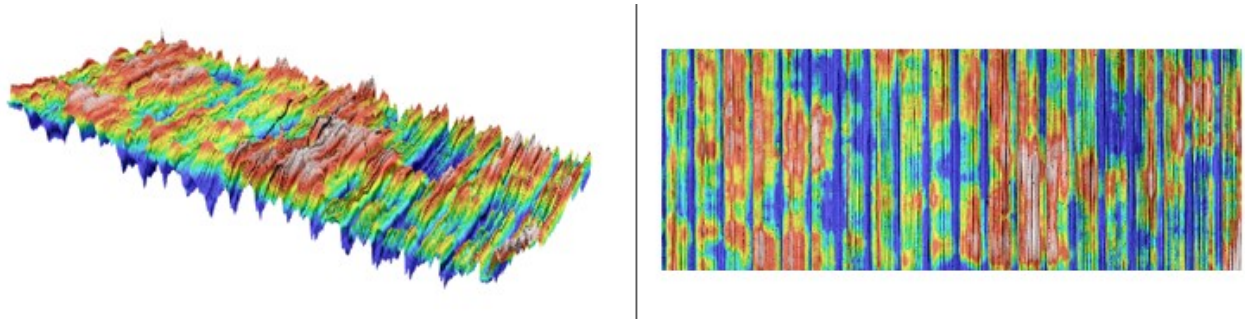

Figure 5. 9: Form Removal Polynomial 3D, 3D view (left), 2D view (right)

Form Removal Polynomial 3D is used to remove the form error due to the cylindrical shape of the specimen. A 4th degree polynomial was chosen to achieve a satisfactory result.

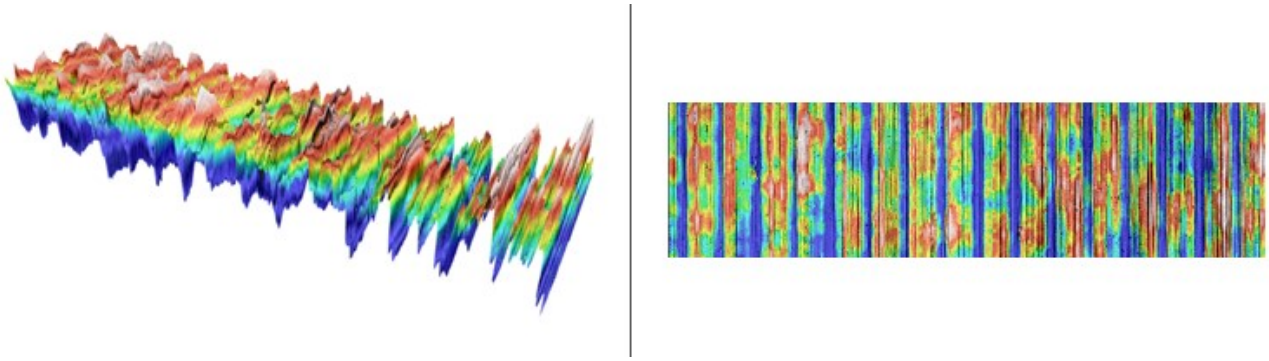

Figure 5. 10: addition of ISO 25178 filter, 3D view (left), 2D view (right)

Roughness must be evaluated net of errors, and for this reason the ISO 2517 standard with Gaussian filters λ_s, λ_c has been used. The first filter λ_s excludes all wavelengths below a certain value, considering them as background noise. Conversely, the second filter λ_c , also called *cut-off* filter, excludes wavelengths above a certain value, which is equal to the sampling length. In fact, the evaluation length is divided into smaller lengths, called *sampling lengths* l_r, which act as a low pass filter to exclude wavelengths attributable to waviness error.

The specimens were subjected to turning, which means that they show a periodic roughness profile. In the case of periodic profiles, the cut-off filter λ_c is a function of the RSm parameter, which corresponds to the average width of the profile feed marks. This means that the RSm parameter corresponds to the feed value *f*.
Therefore, it can be concluded that $RSm = f = 0.07\ mm/rev$.
The EN ISO 4288 standard provides the following table for determining the sampling length and thus the value of the cut-off filter according to the value of the RSm parameter.

RSm (mm)	**Sampling length, l_r (mm)**	**Evaluation length (mm)**
0.013 < RSm ≤ 0.04	0.08	0.4
0.04 < RSm ≤ 0.13	0.25	1.25
0.13 < RSm ≤ 0.4	0.8	4
0.4 < RSm ≤ 1.3	2.5	12.5
1.3 < RSm ≤ 4	8	40

Table 5. 9: sampling length according to the value of the RSm parameter

Since RSm is 0.07 in this case study, the sampling length is 0.25 mm. Therefore, when applying ISO 25178, a cut-off filter of 250 μm was set. It can also be seen that the adopted evaluation length of 1.4 mm is greater than the recommended minimum of 1.25 mm, demonstrating conformity with the standard.
A standard $\lambda_s$filter of 2.5 μm was adopted.
After applying the filters, the image shown *Figure 5. 10* is obtained and the roughness S-parameters can be calculated according to ISO 25178.

5. 6 Microstructure analysis and procedure

To observe the microstructure of Nitinol, samples must be polished and then chemically attacked to corrode the grain boundaries. This allows the microstructure of the material to be observed as the corroded and non-corroded areas reflect light differently.
To polish Nitinol, it is necessary to cut small wedges and embed them in resin. The various steps are shown below.

5.6. 1 Precision cut-off machine

QATM™'s compact automatic precision cut-off machine *Brillant 210A* was used to accurately cut pieces of Nitinol (diameter 9mm, length 3mm) from the turned sample. The machine is equipped with a variable speed cut-off wheel (150-3000 rpm) overlaid by a sample holder where the sample to be cut is placed. With a precision of 5 µm the manual Z-axis can be monitored via display for parallel cuts. Coolant was applied to the cutting area to prevent from getting too hot and thus avoid phase changes in the material.

The cutting-off parameters are:
Speed cut-off wheel: 2200 rpm
Feed: 0.04 mm/s

Figure 5. 11: QATM™'s compact automatic precision cut-off machine Brillant 210A

source: https://www.qatm.com/products/cut-off-machines/benchtop/qcut-150-a/

5.6. 2 Encapsulate samples

The cut nitinol parts are incorporated through the *Struers Labopress-3* mounting press with 30mm closure. The machine offers fully automatic operation with pressure and water assisted cooling cycle. In order to obtain perfectly encapsulated samples, a heating temperature of 180°, a force of 30kN and a heating and cooling time of 7 minutes each were set.

The Nitinol pieces were encapsulated in two different types of resin: WEM Dap resin, based on blue dial phthalate and reinforced with glass fibre, which has excellent abrasion resistance and does not have the problem of edge retention, was brought into contact with the nitinol pieces. The second resin is WEM Phenol, which is cheaper and softer and was used to give the specimen thickness.

Figure 5. 12: Struers Labopress-3 *source: https://spectrographic.co.uk/products/struers-labopress-3 (left), WEM Phenol resin (top right), WEM Dap resin (bottom right)*

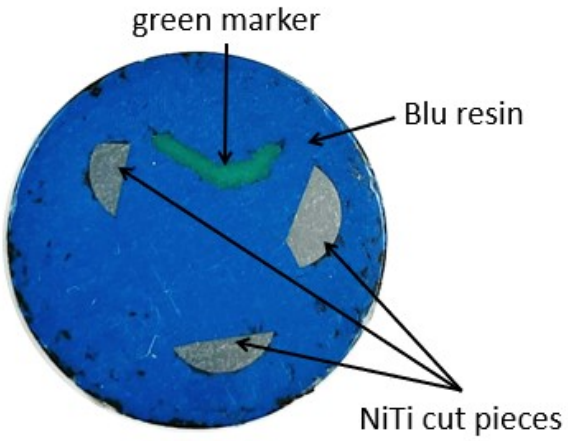

Figure 5. 13: The sample is the result of the encapsulation of the nitinol pieces into the resin. A coloured plastic marker was also incorporated to identify and orientate between the nitinol pieces.

5.6. 3 Polishing

After embedding, it is necessary to polish the specimens to smooth the surface and make the metal mirror-like. Grinding and polishing are carried out on the *Abramin* controlled machine, which uses a horizontally rotating disc and the rotating sample holder eccentrically pressed against it. Amount of pressure, lubricant or cooling water can be manually adjusted whereas the machine controls time and disc speed.

From coarse to fine: P220,P340,P500,P800,P1200,P2400,P4000 are the papers used for polishing.

The *Labopol-1* polishing machine was used to complete the polishing process and achieve a mirror finish on the specimen. To polish the Nitinol alloy, a solution consisting of 2/3 volume of alkaline silica suspension with a particle size of 0.2 microns and 1/3 volume of 30% hydrogen peroxide (H_2O_2) was used.

Figure 5. 14 Abramin *controlled machine, source: https://engineering.case.edu/research/labs/materials-science-metallography-lab/struers-abramin (left), sample holder before polishing (right)*

5.6. 4 Etching

After polishing, the chemical attack (etching) is carried out so that the grain edges can be accompanied and identified under the microscope. Nitinol was attacked using a solution based on hydrofluoric acid (HF) and nitric acid (HNO_3) whose composition is $1ml$ HF, $2ml\ HNO_3$, 47 $ml\ H_2O$. After several trials, an attack time of 60 seconds was chosen. In fact, if the attack time is too short, the right level of corrosion is not achieved to detect the grains; if the exposure time is too long, the sample is extensively corroded. A pipette was used to apply the solution directly to the nitinol pieces.

5.6. 5 Optical Microscope

The Leica® DMR Light Microscope was used for metallographic analysis with Zeiss AxioCam ERc5s camera. The software that comes with the microscope enables to view the sample in real time on a monitor, adjust the image and take measurements after acquisition. This model is equipped with a six-objective revolver: 5x, 10x, 20x, 50x, 100x. The camera provides 10x magnification.

5.6. 6 Scanning Electron Microscope (SEM)

The scanning electron microscope (SEM) was used to observe the microstructure at high magnification or to take pictures of the samples. The SEM uses a focused beam of high-energy electrons, emitted by a tungsten filament, to generate a variety of signals at the surface of the solid specimens. The signals reveal information about the sample including external morphology and chemical composition. Data are collected over a selected area of the sample and a 2-D image is generated.

Accelerated electrons in a SEM carry a significant amount of kinetic energy that is dissipated as the incident electrons are decelerated in the solid sample, producing a variety of signals. These signals include secondary electrons (SE) and backscattered electrons (BSE), both of which are commonly used for sample imaging: secondary electrons are most valuable for showing morphology and topography on samples, while backscattered electrons are most valuable for showing compositional contrasts in multiphase samples.

The images were obtained by SEM using the high vacuum mode, i.e. the operating chamber is brought to a pressure of approximately 10^{-4} Pa.

Images of the specimens were taken using the *FEI Qaunta 450* SEM at the Te.Si. laboratory in Rovigo, University of Padova.

An *EOL™ JSM 7900F HR* (FEG-SEM) was used to image the microstructure of the samples. The FEG-SEM is the most powerful SEM to date, guaranteeing a better resolution useful to detect the NiTi precipitates (micro-scale).

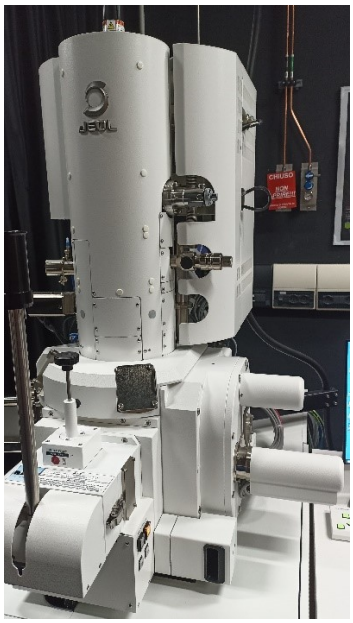

Figure 5. 15: EOL™ JSM 7900F HR (FEG-SEM).

5.6. 7 Energy-Dispersive X-Ray Spectroscopy (EDS)

The Energy-Dispersive X-Ray Spectroscopy (EDS) systems are typically integrated into either SEM instrument. EDS include a sensitive X-ray detector, a liquid nitrogen dewar for cooling, and software to collect and analyse data.

X-rays are produced by the interaction of an electron beam with the sample target. The EDS detector separates the characteristic X-rays of different elements into an energy spectrum which is analysed by the EDS software to determine the abundance of specific elements. The EDS system can determine the chemical composition of materials down to a spot size of a few microns and producing elemental composition maps over a larger area.

A typical EDS spectrum of X-ray count versus energy (in keV) is shown as the result of the EDS test. The energy peaks correspond to the different elements in the sample.

An Oxford Instrument™ ULTIM MAX 40 was used for EDS analysis to determine the chemical composition of the precipitates on unetched NiTi samples.

5.7 DSC

The Nitinol alloy solid-solid transition is studied using differential scanning calorimetry (DSC). This can be used to provide information on the transformation temperatures and to detect the existence of the intermediate R-phase.

DSC is a thermoanalytical technique that measures the difference in the amount of energy (heat) absorbed or released by a sample compared to a reference sample after controlled heating or cooling. The output of DSC is a graph plotting the heat flow (y-axis) as a function of the sample temperature (x-axis), which is measured by a thermocouple throughout the test.

In a heat flow DSC, such as the one used in these tests, the material to be analysed is collected in a pan. The sample pan and the reference pan, which is empty inside, are placed on a thermoelectric disc surrounded by a furnace. The furnace is heated, and the heat is transferred to the pans via the thermoelectric disc. The temperature recorded by the thermocouple of the sample pan is different from that recorded by the one of the reference pan, this is due to the sample's heat capacity (Cp). The heat flow depends on this temperature variation and is determined by the thermal equivalent of Ohm's law:

$$q = \frac{\Delta T}{R} \tag{5. 1}$$

Where q is the sample heat flow, ΔT is the temperature difference between sample and reference, and R is the resistance of the thermoelectric disc. The difference in the input energy required to match the temperature of the sample to that of the reference would be the amount of excess heat absorbed or released by the sample (during an endothermic or exothermic process, respectively). Absorption of energy due to a phase transformation in the specimen results in an endothermic peak on heating. Release of energy due to a phase transformation in the specimen results in exothermic peak on cooling.

5.7. 1 DSC configuration

Data was collected on a TA Instruments Q200 DSC equipped with a Refrigerated Cooling System.

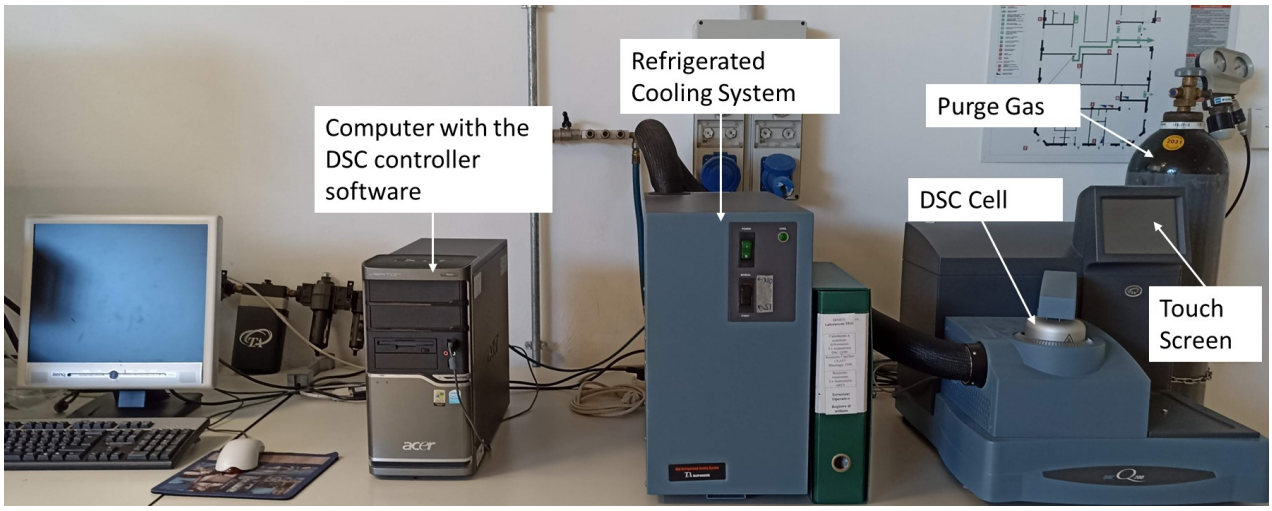

Figure 5. 16: DSC configuration

DSC Cell: the cell consists of a constantan body with separated raised platforms to hold the sample and the reference.

Refrigerated Cooling System: it is used to perform DSC cooling experiments and consists of a cooling head and anti-condensate heaters. The cooling head fits over the DSC cell.

Purge Gas: nitrogen is used as a flowing inert purge gas and it helps to remove moisture or oxygen which may accumulate in the cell, it eliminates localized hot-spots and provides for more efficient heat transfer and finally it helps to cool the cell.

Touch Screen: the instrument has a built-in integrated display in the form of a touch screen for local operator control.

Technical Specifications:
Heating range: -70 to 400°C
Heating rates: 1 to 20°C/minute
Temperature accuracy: ±0.1°C

5.7. 2 Procedure

The Standard Test Method for Transformation Temperature of Nickel-Titanium Alloys by Thermal Analysis (F2004-17) was followed to define the procedure.
The steps from sample preparation for DSC analysis to data acquisition are as follows:

1. Sampling: DSC test samples cannot weigh more than 50-60 mg, so it is necessary to cut small pieces of Nitinol from the machined sample using the Precision Cut-off Machine described above. In particular, the cut is made close to the machined surface to analyse the effects of machining, and a feed of 0.02 mm/s is used to avoid overheating during cutting. The mass of the DSC samples tested varied between 20 and 55 mg.
2. Polish the sample to remove the oxide.
3. Wash the sample in an ultrasonic bath with 99% ethanol and dry with a hairdryer.
4. Weight the sample using an analytical balance with a capacity of 100 mg capable of weighting to the nearest 0.1 mg.
5. Place the sample on the aluminium pan and encapsule using the Tzero Sample Encapsulating Press.
6. Open the DSC Cell and place the encapsulated sample pan on the test pedestal near the reference pan, close the cell.
7. Turn on the purge gas at a flow rate of 50 mL/min.
8. Defines input data via machine software: sample mass, sample name and Test Method.

   The Test Method used is:
   Ramp 10.00 °C/min to -70.00 °C
   Isothermal for 2.00 min
   Ramp 10.00 °C/min to 120.00 °C
   Isothermal for 2.00 min
   Ramp 10.00 °C/min to 10.00 °C

   This means to cool the sample from room temperature (24°C) to -70°C at a rate of 10±0.5°C/min and held at this temperature for 2 minutes to equilibrate the sample with the furnace. The sample is then heated from -70°C to 120°C at a heating rate of 10±0.5°C and again held at 120°C for 2 minutes. Then cool the sample to 10°C using the same heating rate. The cycle is now complete.

9. Data acquisition: record the resulting curve from the cooling and heating test method.
10. Begin with the post-processing work.

Figure 5. 17: weigh DSC sample and place it in the DSC pan.

5.7. 3 Data Analysis

TA Universal Analysis programme is used to analyse the DSC data.

The figure shows the heat flow (W/g) - temperature (°C) graph directly obtained from the SDC scan. From the start point to the end point, the graph follows the set test method, i.e., cooling-isothermal-heating-isothermal-final cooling to complete the cycle. The graph must then be further processed to obtain the transformation temperature and enthalpy change data.

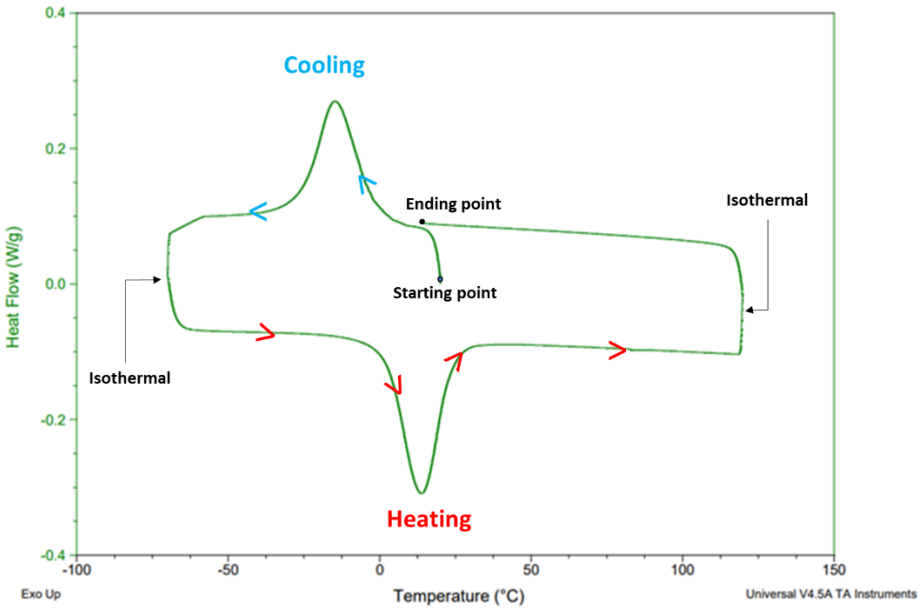

Figure 5. 18: DSC graph

The enthalpy of transition, ΔH, is calculated by integrating the peak corresponding to the given transition, it can be expressed using the following equation:

$$\Delta H = KA \tag{5. 2}$$

Where K is the calorimetric constant (it varies from instrument to instrument), and A is the area under the curve.

To calculate the area under a peak and therefore the enthalpy of transition, the Integrate Peak/Sig Horizontal function available in the software was used.

When using this function, it is necessary to identify the points that define the base of the peak area to be integrated (baseline). The software then automatically calculates the integral, which gives the ΔH value. It also draws the tangent to the graph at the inflection point; the intersection of the tangent with the baseline gives the temperature at the start of the transformation (rising part of the peak) or at the end of the transformation (falling part of the peak). In this way the start and end temperatures of martensite and austenite can be known. The function also returns the peak temperature values (M_p and A_p).

Figure 5. 19 shows the same graph as the previous figure but with the addition of the Integrate Peak/Sig Horizontal function. The values of the transformation enthalpy and transformation temperatures of both peaks are then given.

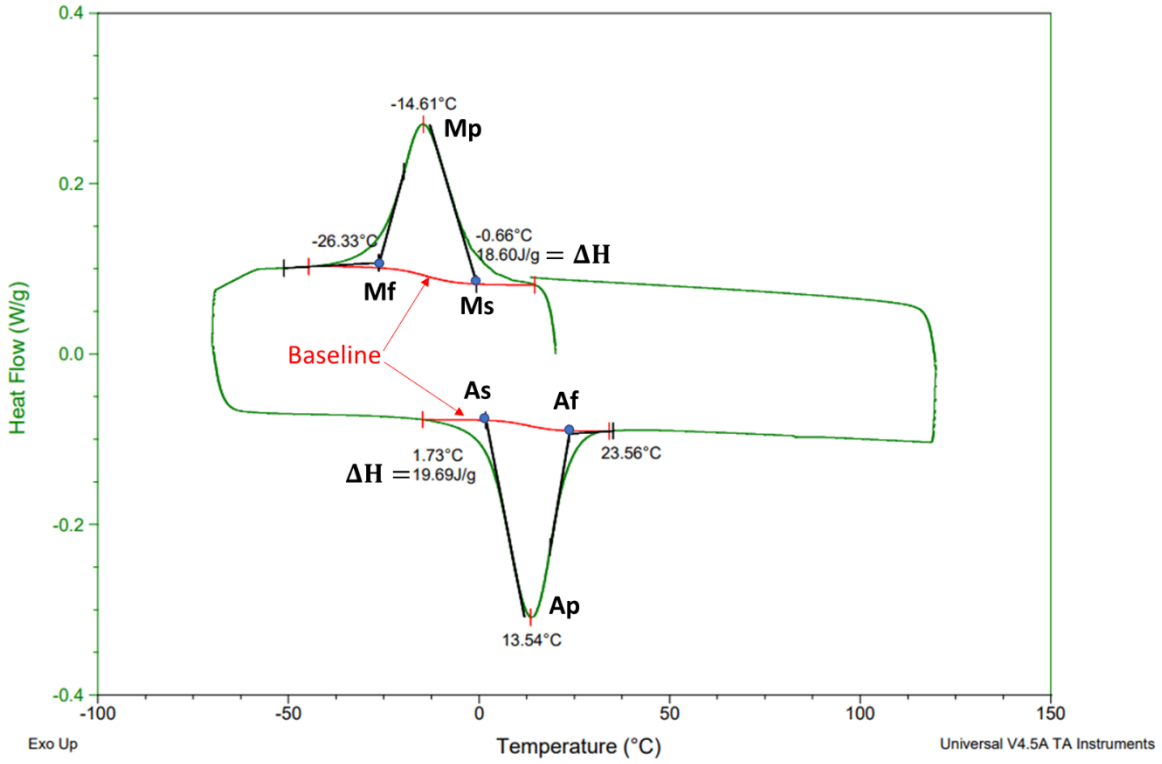

Figure 5. 19: DSC graph with integrated peak and tangent intersections

5.8 Nanoindentation

The UNHT ultra-high-resolution nanoindenter by Anton Paar™ is used to examine the mechanical properties of a material at the nanoscale. A diamond Berkovich indenter was used to characterize nanohardness, H, reduced elastic modulus, E_r, and the work recovery ratio, η.
Berkovich indenter was installed at the bottom side of the transducer, while the optical microscope is linked to the transducer for positioning.
During indentation, the optical microscope is used to locate the area to be indented by moving along the X and Y planes. Once the zone has been located, the Berkovich tip moves towards the indentation point and begins to move downwards along the Z-axis, then begins to indent the sample (depth resolution 0.003 nm). The transducer is equipped with a force sensor to measure the various phases of force application and removal (load resolution 3nN), thus obtaining the load-displacement graph. The calibration process that precedes the indentation is used to accurately position the optical microscope using an Al benchmark, while the fused quartz benchmark is used to calibrate the contact area function (see equation (2. 11)).

The surface indentation was performed using a 2 x 5 matrix pattern. The row and column spacing of matrix are 20 μm and 20 μm. The top row of indents was located within 40 μm below the surface.
A maximum load of 1mN was used for all the indentations. The maximum load is reached linearly in 30 seconds, is held constant for 10 seconds and then begins to decrease linearly to zero after 30 seconds. The speed rate for both loading and unloading is therefore 2mN/min.

All indentation tests were conducted at the Istituto Italiano di Tecnologia (IIT) based in Genova.

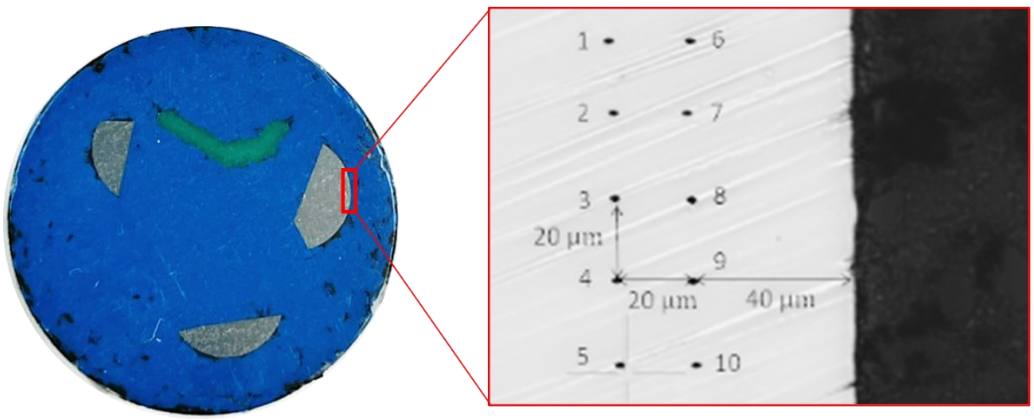

Figure 5. 20: indentation array on a Nitinol specimen

Figure 5. 21: ultra-high resolution nanoindenter by Anton Paar™ in the IIT laboratory.

5.9 Tribometer

5.9. 1 Tribometer configuration and setup

The RTEC™ tribometer was used to study the tribological properties of Nitinol. The tribometer configuration is shown below.

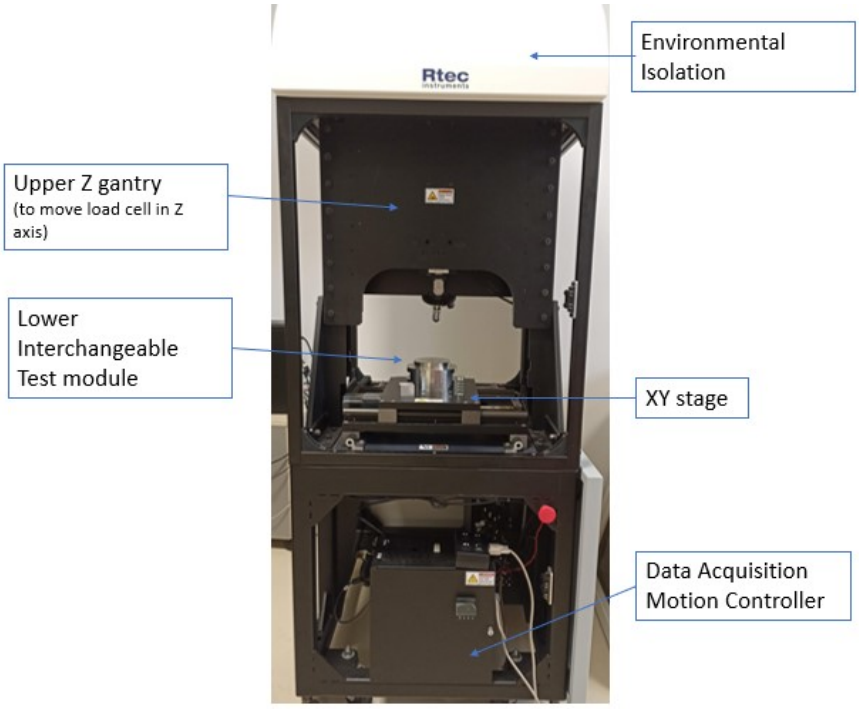

Figure 5. 22: RTEC™ tribometer configuration

As mentioned in the previous chapters, a pin-on-disc configuration test was chosen. For each test to be carried out on the tribometer, it is important to decide on the set-up to be adopted. In this case, the pin-on-disc apparatus consists of a pin, represented by the machined Nitinol sample, that is held stationary and a steel AISI 51200 100CR6 flat circular disc attached to a *rotary drive*. A special aluminium *fixing plate* with three M4 screws equally spaced around the circumference is used to secure the disc over the rotary drive. The steel disc is placed in the centre of the plate and secured by tightening the three screws; the whole assembly is mounted on top of the rotary drive.

The tribometer has two load cells, F_x and F_z. The F_x load cell is located at the base of the *friction arm* assembly, while the F_z load cell is placed on the *Z stage* above the friction arm assembly.

During the test, the coefficient of friction is continuously monitored by measuring the friction force (F_x) while a fixed load (F_z) is applied to the pin-disc contact.

The test begins when the pin, which is subjected to the normal load (F_z), contacts the rotating disc.

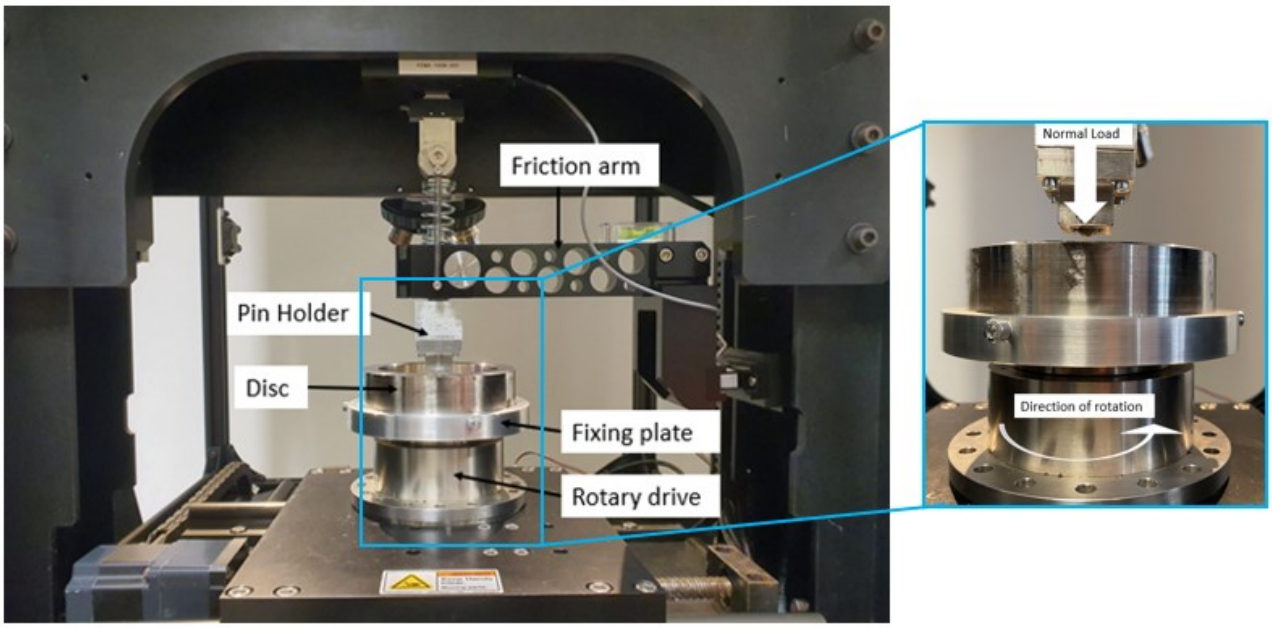

Figure 5. 23: tribotest setup and components (left), the pin-on-disc mechanism (right)

5.9. 2 The pin and the disc

Nitinol balls, which are the pin of the test, were machined on a lathe using the same cutting parameters as the previous samples. In fact, the cylindrical shape of the previous machined specimens (diameter 9mm and length 3mm) was not suitable for wear testing. Therefore, it was deemed necessary to machine more AM Nitinol samples on the lathe to obtain a final spherical shape with a radius of 4.6 mm and height of 5mm.

In tribotesting it is important the use of reference materials to validate the procedure. For this reason, a comparison between Nitinol balls and a ball made of a common bearing steel (AISI 51200 100CR6) is reported.

A tribological test was therefore carried out in which the pin was a steel ball taken from a roller bearing. The steel roller was flood machined on the lathe using the same cutting parameters as the Nitinol. In this way, the machining process used for the Nitinol balls was faithfully replicated also for the steel ball.

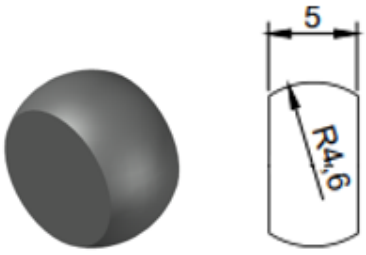

Figure 5. 24: ball for tribotest

The counterpart consists of a AISI 51200 100CR6 flat circular disc. The faces of the disc have been polished to achieve a surface roughness S_a of 27.5 $\pm$ 3.9 nm measured by *Sensofar Metrology™ S Neox* 3D profilometer.

Figure 5. 25 shows the dimensions of the disc and the diameter of the wear track. As can be guessed, the wear track corresponds to the sliding path.

The dimensions of the disc are as follows:

External diameter, $D = 125.7$ mm

Internal diameter, d = 98.5 mm

Disc height, h = 38 mm

Diameter of the wear track, $D_t = 120.9$ mm

Figure 5. 25: AISI 51200 100CR6 disc dimensions

	Specimen Pairs						
Pin	F_AB	F_T3	F_T6	C_AB	C_T3	C_T6	Steel
Disc	steel	steel	steel	steel	steel	steel	steel

Table 5. 10: Specimen pairs in tribological test

5.9. 3 Test parameters and procedure

The tribological test parameters are as follows:

- Load: value of the force in Newtons at the wearing contact.
- Speed: the relative sliding speed between the contacting surfaces in meters per second.
- Distance: the accumulated sliding distance in meters
- Time: the duration of the test
- Sliding radius: radius of the wear track

	Load (F_z) (N)	**Speed**	**Distance (m)**	**Time (min)**	**Sliding Radius (m)**	**Test condition**	**Direction of rotation**
Values	10	0.03 (m/s), 4.74 (rpm)	108	60	0.0605	DRY (no lubricant)	Anticlockwise

Table 5. 11: tribotest parameters

The procedure specified in the pin-on-disk standard (ASTM G99) was followed, which consists of:

1. Clean and dry the specimens: balls were washed in an ultrasonic bath with 99% ethanol and dried with a hairdryer while the disc face was wiped with ethanol.
2. Measure the specimens' dimensions and roughness.
3. Insert the disc is in the centre of the fixing plate and secure it by tightening the three screws so that the disc is perpendicular to the axis of the resolution. To ensure this last point, a dial gauge was used as shown in *Figure 5. 26.*
4. Insert the pin in its holder and adjust so that the specimen is perpendicular to the disc surface. The spirit level on the friction arm supporting the pin holder was used to ensure vertical alignment.
5. Enter process parameters: load value Fz, test duration, speed (rpm) and number of revolutions are set in the dedicated software connected to the machine.
6. Begin the test with the specimens in contact under load.
7. At the end of the test, remove the specimens and clean.
8. Remeasure the specimens' dimensions.
9. Prepare the setup for the next test, then use the still blank face of the disc or polish the already used face to restore the original roughness.

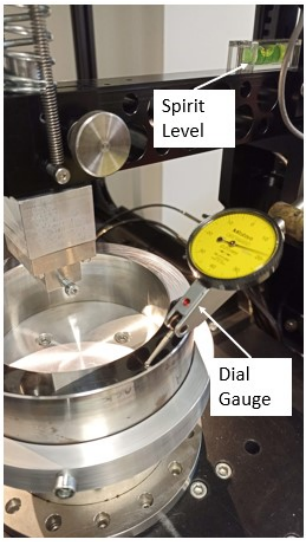

Figure 5. 26: dial gauge and spirit level to ensure vertical alignment.

5.9. 4 Wear Calculation

The wear measurement is reported as the volume loss in cubic millimetres for the pin and disc. Linear measures of wear are used since mass loss is too small to measure precisely.

More interest is given to the wear on the ball whose dimensions were measured using *Sensofar Metrology™ S Neox* 3D profilometer. The wear scar profile is measured in two orthogonal directions. The figures below show the worn area with the horizontal and vertical diameter measurements and the corresponding profiles of the F_AB sample used as an example. No post-processing was carried out, as the aim was to measure the worn part directly from the profilometric image.

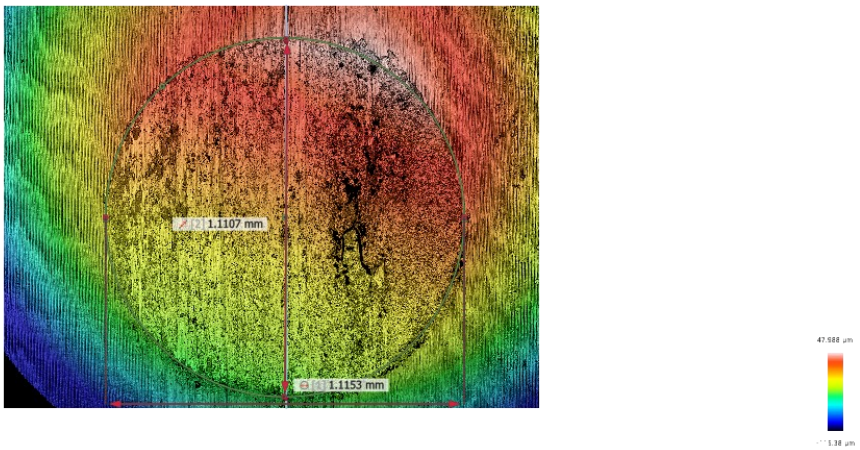

Figure 5. 27: wear scar main view with diameters measurements

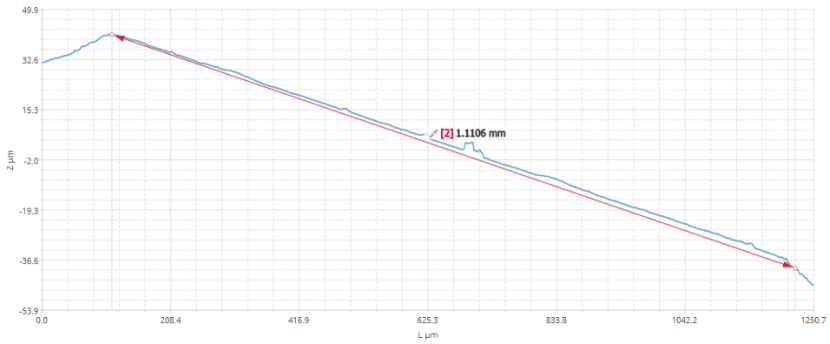

Figure 5. 28: horizontal profile

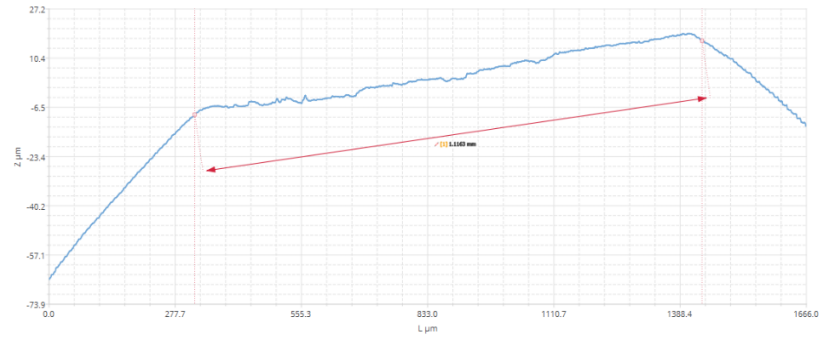

Figure 5. 29: vertical profile

The measurements of the two diameters of the wear scar are then averaged. The procedure for calculating the volume loss, starting from the diameter measurement, is shown below.

$$a = rsin(\theta) \tag{5. 3}$$

Where a is the wear scar ray calculated from the previous measurements on the profilometer, r is the radius of the ball, θ is the angle between r and b (see *Figure 5. 30*).
From the previous equation it is possible to calculate θ and then obtain:

$$b = rcos(\theta) \tag{5. 4}$$

Knowing b, h can be calculated by the difference between the radius of the ball and b:

$$h = r - b \tag{5. 5}$$

h represents the depth of the worn zone.

Now that h is known, it is possible to calculate the volume of the spherical segment that corresponds to the volume loss, using the following formula:

$$V = \pi h^2 \left(r - \frac{h}{3} \right) \tag{5. 6}$$

Standard (ASTM G99) reports the following equation for calculating volume losses when the pin has initially a spherical shape of radius r and the disc is flat:

$$V = \frac{\pi (2a)^4}{64r} \tag{5. 7}$$

The comparison between the two methods of calculating volume loss is explained in the results section.

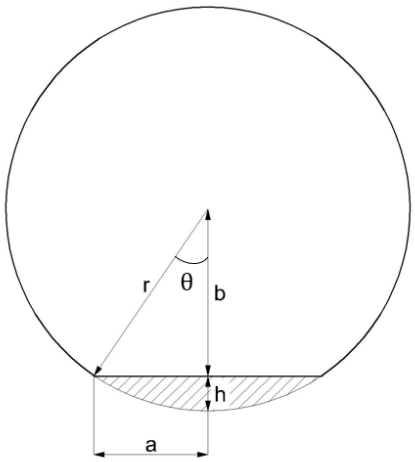

Figure 5. 30: spherical segment illustration

5.9. 5 Coefficient of Friction

During the test, the frictional force F_x is constantly measured by the load cell located on the frictional arm with a time interval of 0.1s, so that the value of the friction coefficient μ is directly displayed, since:

$$\mu = \frac{F_z}{F_x} \tag{5. 8}$$

The graphs of the friction coefficient as a function of time for the F_T3 and Steel specimens are shown below.

As can be seen from the graphs, two coefficients of friction have been distinguished: the *Initial Coefficient* and the *Steady State Coefficient*. The test takes time, which varies from sample to sample, to reach the nominal friction coefficient, i.e., the steady state value. Therefore, two coefficients were calculated: the first is an average of the coefficients within the initial phase of the test, the second is an average of the steady state coefficients.

A comparison of the two graphs also shows that the time taken to reach the steady state friction coefficient varies. In the case of F_T3, the initial part takes about 500 seconds, in the case of steel 800 seconds. The blue line in the graph represents the signal recorded by the tribometer. Because of the complexity of the signal, it was considered necessary to apply a 120 moving average filter (red line), which means that each average is calculated over a sliding window of length 120 across neighbouring elements. Some tests were subject to stick and slip phenomena, as can best be seen from the higher irregularity of the red line of the F_T3 sample compared to the steel. In fact, the steel is more regular in the steady state zone.

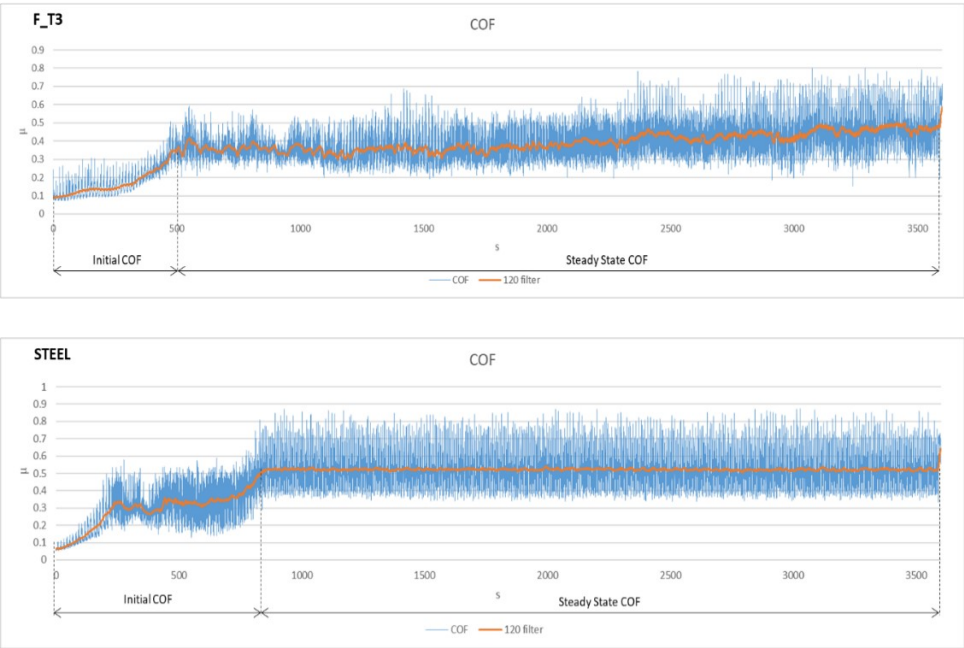

Figure 5. 31: Example of graphs obtained from coefficient of friction measurements.

CHAPTER 6

RESULTS

The results of the analyses and tests described in the previous chapter are presented below. In particular, the findings of the surface integrity, microstructure, super-elasticity, transformation temperatures, wear, and friction coefficients of the NiTi samples are discussed, focusing on the comparison between the different process parameters (for a reminder, see *CHAPTER 4*).

6. 1 Surface Integrity

Let us begin by showing the surface roughness of the machined samples in order to observe a first difference between flooding machining and cryogenic machining.

6.1. 1 Roughness

Figure 6. 1 shows a typical surface of a cryogenic sample aged at 600°C (C_T6) while Figure *6. 2* shows the corresponding profile extracted from the same acquisition. Data on the width of a feed mark has been reported.

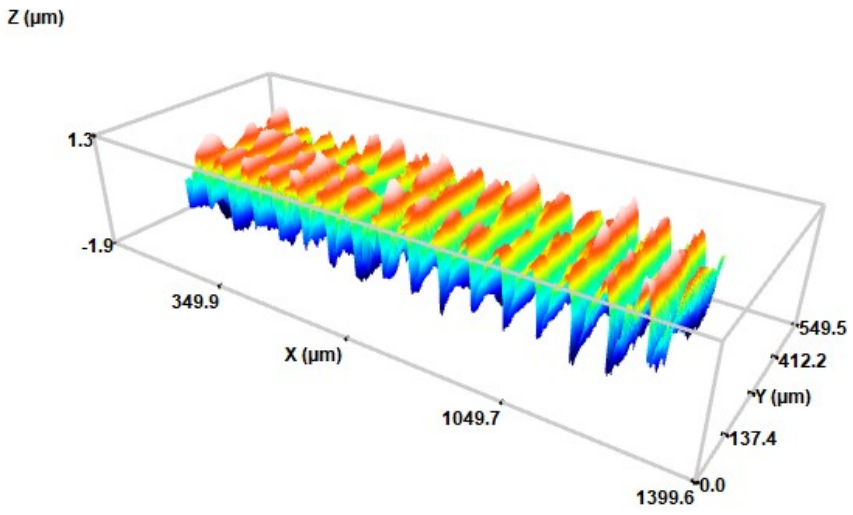

Figure 6. 1: C_T6 sample surface acquired by scanning with the 3D profilometer. Feed marks from turning are visible

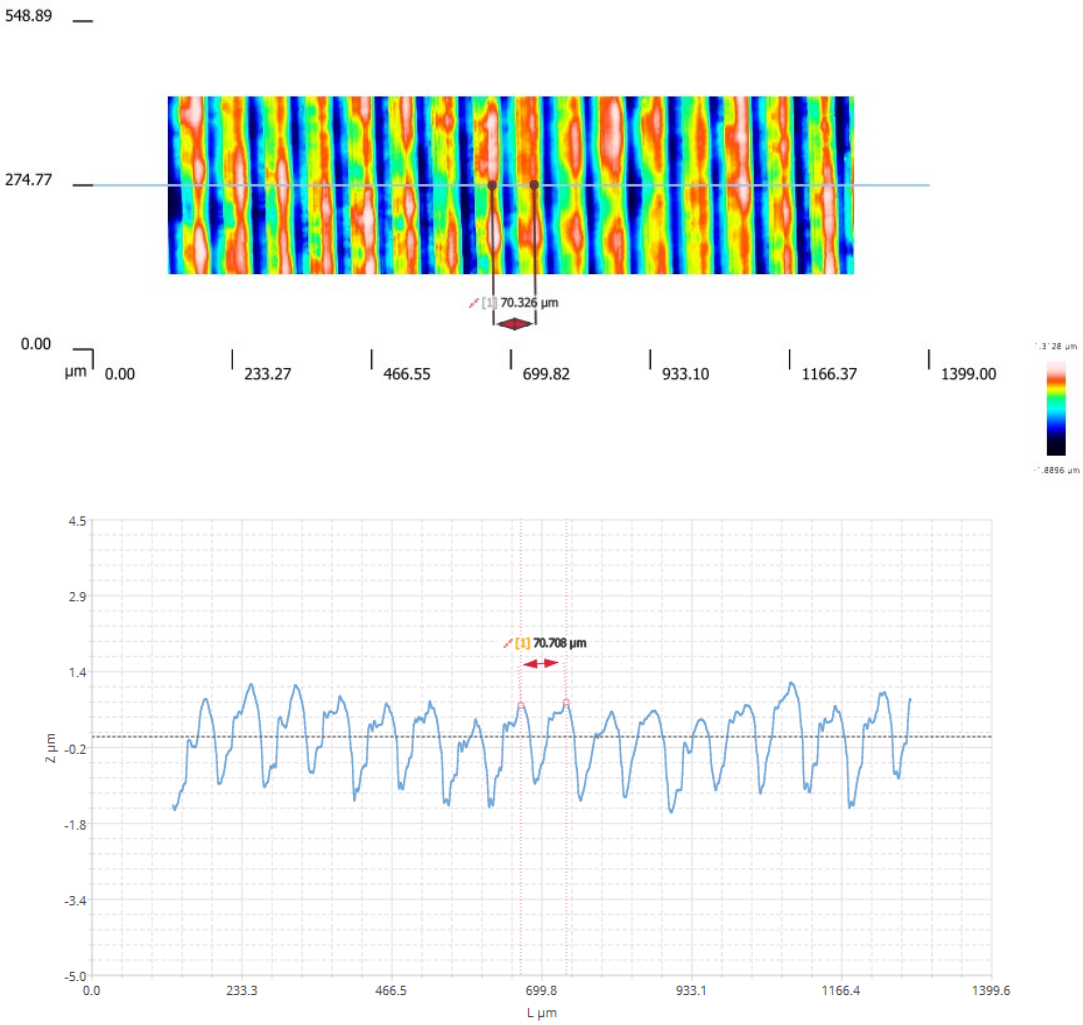

Figure 6. 2: Typical profile of NiTi alloy after machining

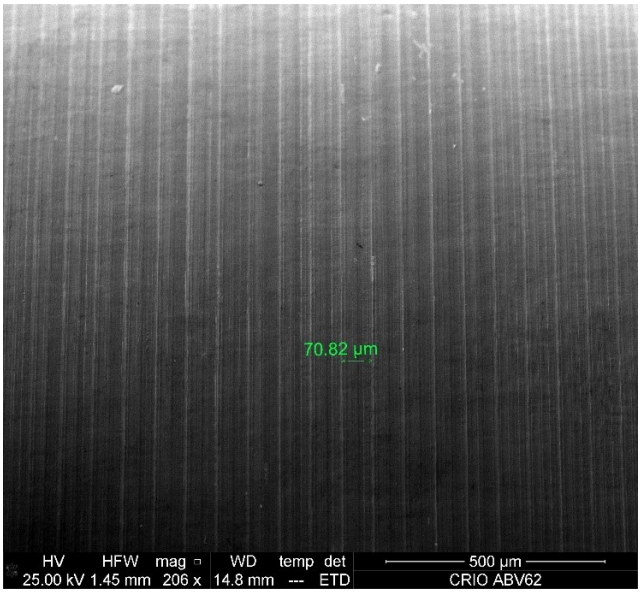

Figure 6. 3 SEM image showing feed marks after machining.

Both the 3D profilometer and the SEM provide images in which the feed marks caused by machining can be seen. The fact that the measured feed mark width is 70 µm is proof that the feed used during machining is 0.07 mm.

Several measurements were taken for each specimen. The table shows the average roughness Sa and the corresponding standard deviation.

	Specimens	Sa (mean) [µm]	Standard Deviation [µm]
Flood	**F_AB**	0.33	0.029
	F_T3	0.35	0.005
	F_T6	0.34	0.017
Cryo	**C_AB**	0.29	0.005
	C_T3	0.25	0.014
	C_T6	0.29	0.016

	Flood-cryo Difference Δ%
AB	13.8%
T3	40%
T6	17.24%

Table 6. 1: arithmetical mean height Sa and standard deviation of specimens (left table), flood-cryo difference varying heat treatments (right table)

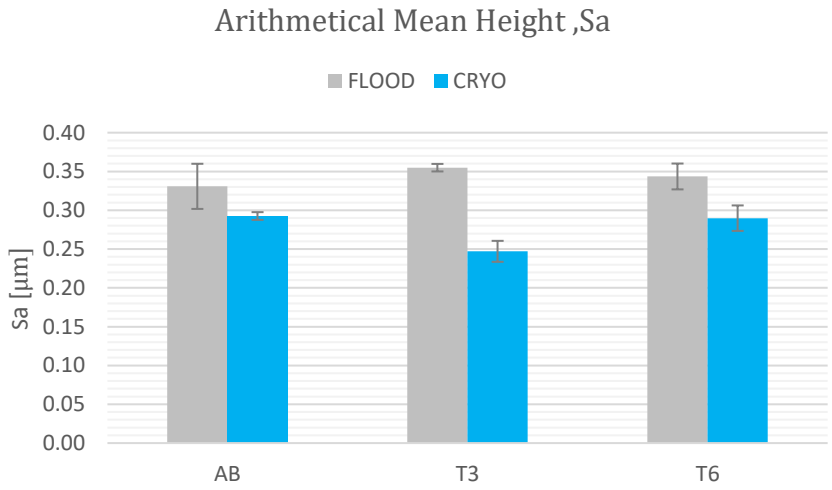

Figure 6. 4: flood-cryo comparison in terms of arithmetical mean height, Sa

It was decided to report Sa, which is the most significant surface roughness parameter, to highlight the differences between flood and cryogenic machining. From the data shown in the tables above and the corresponding graph, it is easy to see how cryogenic machining improved the surface integrity of the specimens in terms of roughness. In fact, in the case of the T3 samples, Sa decreased by 40% between flood and cryo. Samples aged at 300°C are those that show the most net change between the two machining methods. This is followed by the 600°C aged specimens and then by the untreated specimens (AB). T6 and AB show a decrease in Sa roughness of almost 20% for the former and just over 10% for the latter.

6.1. 2 SPD Layer

The following optical images show the surface area affected by machining. Red dashed curves have been drawn to highlight the severe plastically deformed layer (SPD) of each machined specimen. The SPD layer is thicker on the T6 specimens, particularly on the T6 cryo. On the other hand, the T3 samples are those where the SPD layer is thinner and the difference between cryo and flood is small, although the SPD layers of the flooded samples appear to be thinner than those of the cryo samples due to the higher cutting temperature reached during flood machining, which favours deformation recovery.

To see the effects of machining it is important to note the thickness of the SPD layer as it is closely related to the surface hardness of the material.

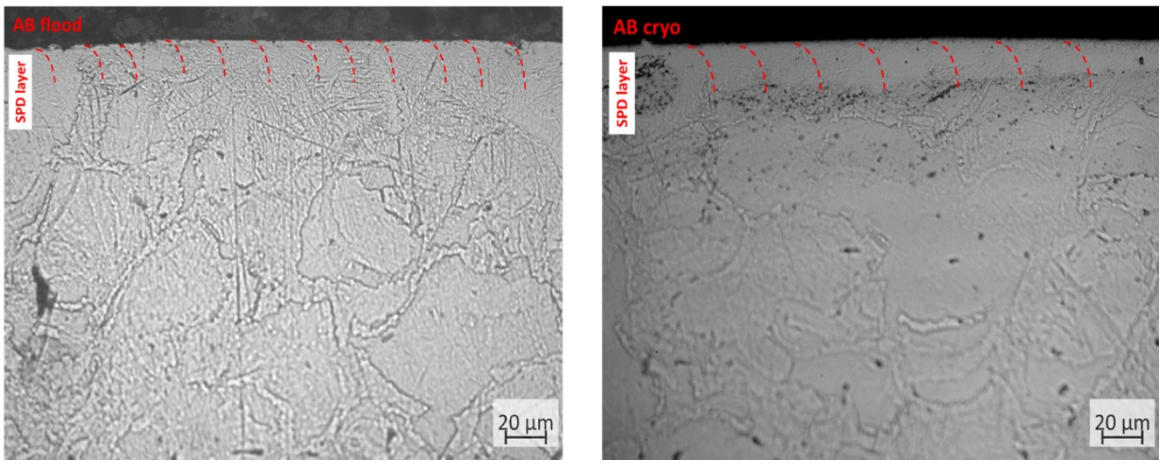

Figure 6. 5: Microstructure of AB flood and cryo machined specimens

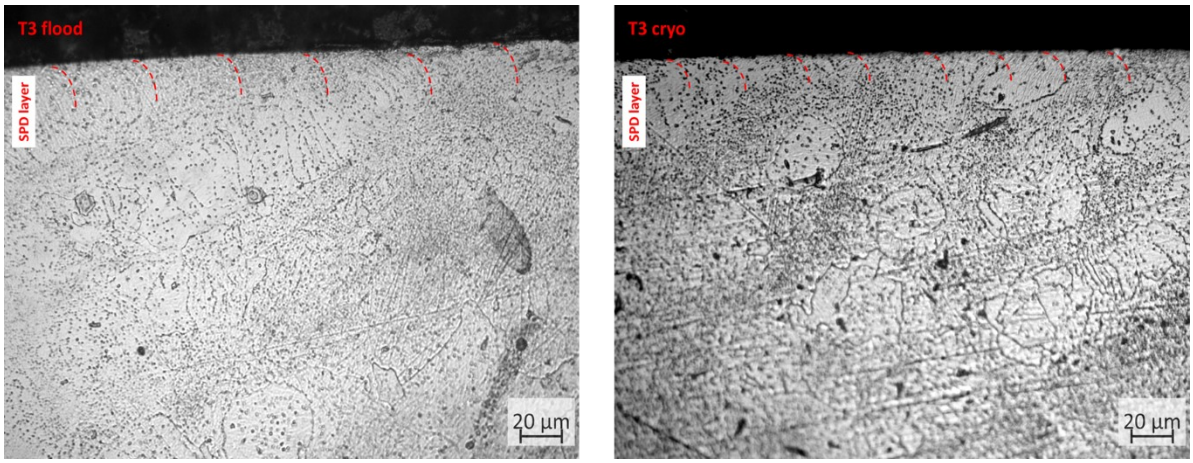

Figure 6. 6: Microstructure of T3 flood and cryo machined specimens

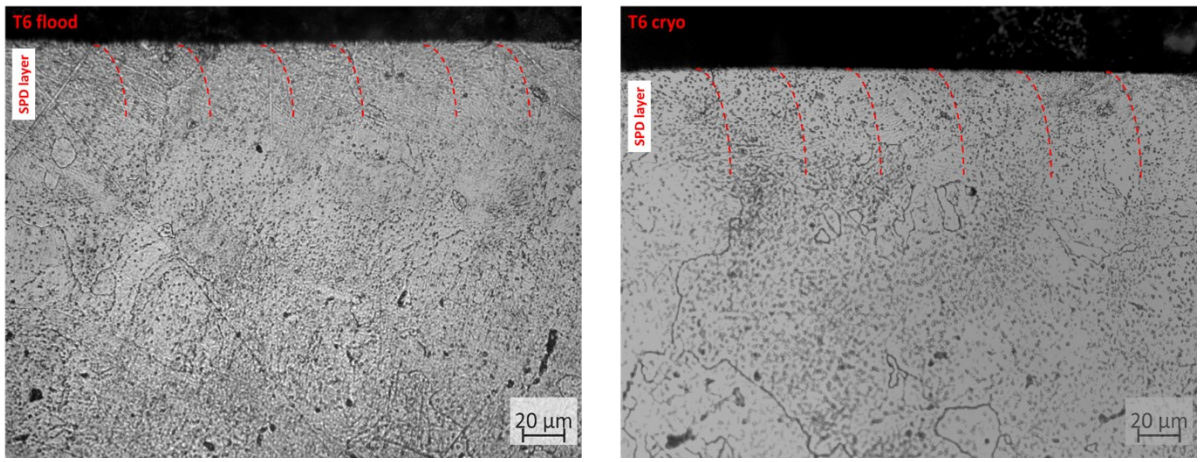

Figure 6. 7: Microstructure of T6 flood and cryo machined specimens

6. 2 Microstructure

6.2. 1 Bulk Microstructure

The optical images of the etched Nitinol samples after AM and heat treatment are shown below. The images represent the cross section with respect to the building direction (BD), i.e., the direction followed when the specimens were printed in additive manufacturing.

The AB microstructure consists of equiaxed B2 cubic austenite grains with an average size equal to the hatch spacing, approximately 60 μm as shown in Figure 6. 8..

From the images, the samples that have undergone heat treatment (T3 and T6) have larger and more irregular grains than sample AB.

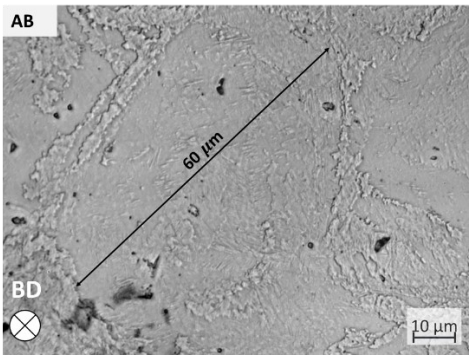

Figure 6. 8: AB grain size

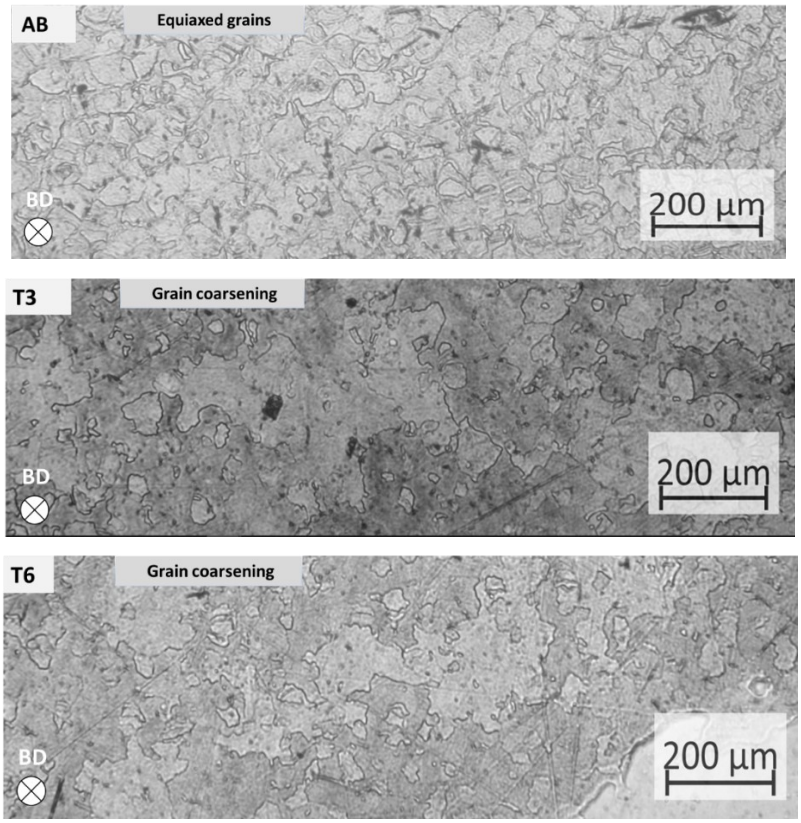

Figure 6. 9: AB, T3 and T6 microstructure before machining.

6.2. 2 Precipitates Detection

To assess the precipitates' nature, energy dispersive spectroscopy (EDS) elemental analysis was performed on unetched polished samples.

The magnified FEG-SEM images are given below, which show the shape of the precipitates found in samples T3 and T6. Sample AB, which did not undergo heat treatment, did not develop any precipitates.

The precipitates in sample T3 are spherical, denser, and smaller than those in sample T6. In the latter, precipitates larger than 1 μm are found. This kind of precipitate loses its spherical shape in favour of a more elongated, needle-like shape. This result agrees with what has been reported in paragraph *2.3. 1* stating that the size of the precipitate is a function of the ageing temperature. In particular, the size of the precipitates increases as the treatment temperature increases, becoming incoherent with the matrix.

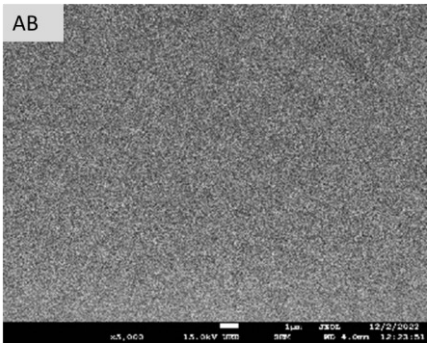

Figure 6. 10: AB FEG-SEM image, no precipitates detected.

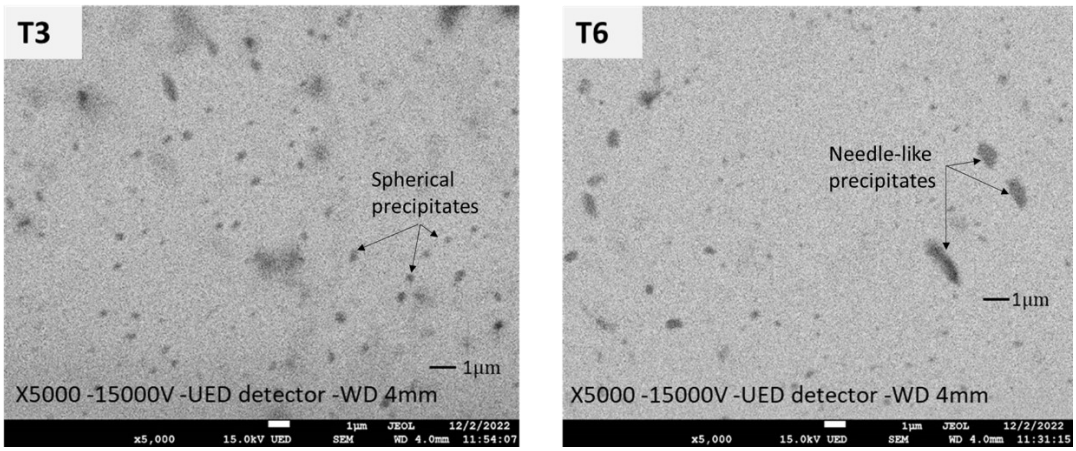

Figure 6. 11: FEG-SEM images showing the shape of the T3 and T6 precipitates.

EDS analysis gives the following results in terms of the chemical composition of the precipitates and the neutral zone (the zone where no precipitates are detected).

Two different zones were investigated: one inside the precipitate (darker zone), and one outside the precipitate (lighter zone) where the chemical composition of the original alloy is expected to be found (Ni 50.8, Ti 49.2 %at.).

As can be seen from the data in *Table 6. 2*, sample T3 shows a not insignificant percentage of oxygen both inside and outside the precipitate. It can be concluded that this oxygen infiltration within the alloy may have occurred during the heat treatment. The nature of the precipitate found in sample T3 could be attributed to the following precipitate: Ti_4Ni_2O already reported in the literature [27].

The precipitates found in both sample T3 and T6 are Ti-rich. This is probably because Ti-rich precipitates are larger in size and therefore easier to detect. On the other hand, Ni-rich precipitates such as Ni_4Ti_3 are known to form on a smaller scale (1-3nm) and are therefore difficult to find with these instruments and at these magnifications.

Specimens	Elements	Neutral zone Atomic %	Precipitate Atomic %
T3	Ni	47.43	33.98
	Ti	46.44	52.98
	O	6.13	13.04
T6	Ni	51.23	45.08
	Ti	48.77	54.92

Table 6. 2: EDS result: chemical composition

Ti-rich precipitates can be identified because they appear darker under the SEM images. In contrast, Ni-rich precipitates should appear brighter than the surrounding area.

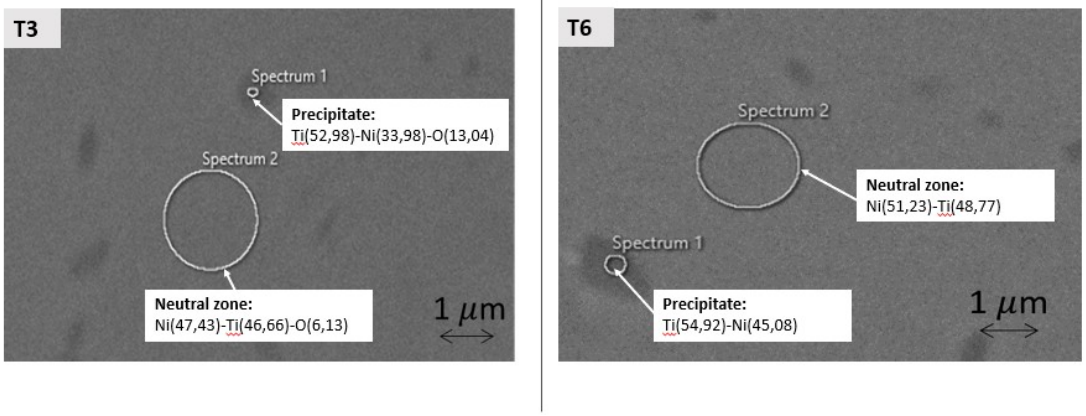

Figure 6. 12: FEG-SEM images, chemical composition from EDS results

6. 3Transformation temperatures

DSC results from pre-machined, flooded and cryogenically machined specimens at different heat treatments are presented in tabular and graphical form. The aim of the DSC analysis is to identify the transformation temperatures, so the values of M_s, M_f, A_s, A_f and, where present, R_s and R_f are given below. The room temperature was set at 24°C.

The following points can be deduced from Table 6. 3:

1. It is confirmed that the pre-machining samples are austenitic at room temperature.
2. There is never any presence of the R phase in the pre-machining samples or in the T6 samples even after machining.
3. T3 samples are never austenitic at room temperature after both flood and cryo machining. The transformation from austenite to martensite through the R-phase starts at around 30°C for both processes. In T3 samples the R phase is present in both the austenite-martensite transformation (cooling) and the reverse martensite-austenite transformation (heating).
4. AB specimens only show the R phase when flood machined and during the austenite to martensite transformation (cooling). In this case it can be assumed that cryogenic machining slows down the appearance of the R phase.
5. In general, it can be observed for all samples that machining always results in an increase in the final austenite temperature. In certain cases, such as the T3 samples, machining does not lead to full austenitic transformation at room temperature.
6. The difference between flood and cryo is less pronounced than that between the heat treatments. However, in the case of the T6 specimens, there is a marked improvement with cryo, as A_f decreases and approaches the values of T6 before machining.
7. No significant conclusions can be drawn about the transformation enthalpy or latent heat ΔH of either the cooling or heating part. The change in enthalpy depends on the volume of the transformed material. As can be seen from the table, in most cases ΔH of pre-machined samples is higher than that of machined specimens. Thus, the volume of transformed material in machined samples can be smaller than the pre-machined material. The reduced volume of transformed material is due to the high dislocation/twinning density introduced by plastic deformation during the machining process. Cryogenically machined samples, due to the low temperature of the cutting process, are expected to be those with the lowest ΔH. However, this is particularly true for low cutting speeds.

	Samples	Cooling					Heating				
		R_s (°C)	R_f (°C)	M_s (°C)	M_f (°C)	$\Delta H_{cooling}$ (J/g)	R_s (°C)	R_f (°C)	A_s (°C)	A_f (°C)	$\Delta H_{heating}$ (J/g)
Pre- Mach.	**AB**	no	no	-7.6	-65	16.34	no	no	-18	12.8	12.76
	T3	no	no	-4.9	-64	10.99	no	no	-6	21.5	14.44
	T6	no	no	-17	-63	20.12	no	no	-15	9.1	20.02
Flood	**F_AB**	2.75	-22.6	-26	-69	7.137	no	no	-21	15.5	12.94
	F_T3	30.9	18.43	-23	-69	11.284	-2.9	31.2	31.2	40.6	15.63
	F_T6	no	no	2.06	-67	17.09	no	no	1.73	23.6	19.69
Cryo	**C_AB**	no	no	2.06	-67	17.09	no	no	-18.4	23.2	16.78
	C_T3	34.7	20.5	-26	-69	11.95	3.36	30.9	30.9	43.2	15.94
	C_T6	no	no	-13	-39	16.63	no	no	-6.9	11.6	19.38

Table 6. 3: DSC results

The graph in Figure 6. 13 makes a comparison between A_f, as this is the value of most interest on which the super-elastic property of the material depends.

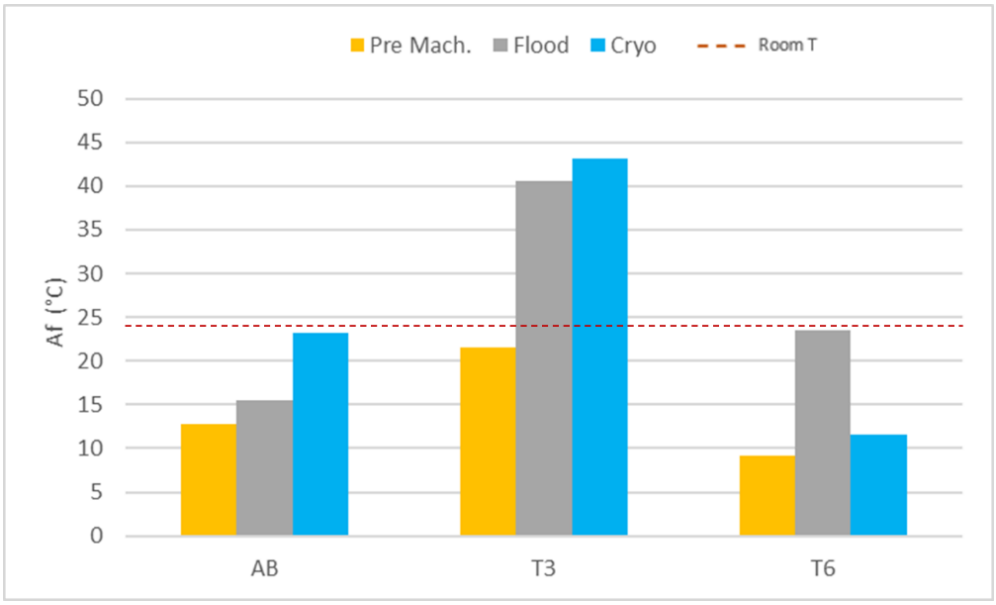

Figure 6. 13: Af comparison from DSC results

6.3. 1 DSC Results - Heat Treatment Comparison

The following graphs were generated using MATLAB from data provided by the DSC. The plots show the martensite to austenite transformation (heating part) and the point where A_f (X coordinate) occurs has been highlighted. For each grouping (pre-machining, flood and cryo) the first graph (red line) relates to AB, the second (green line) to T3 and the third (blue line) to T6. These graphs also confirm that the A_f of T3 flood and cryo is above the ambient temperature indicated by a dotted line, while T6 flood is close to this line.

The plots also show the two peaks of the T3 flood and cryo samples. The first peak concerns the R phase, the second completes the transformation ending with Af.

PRE-MACHINING DSC

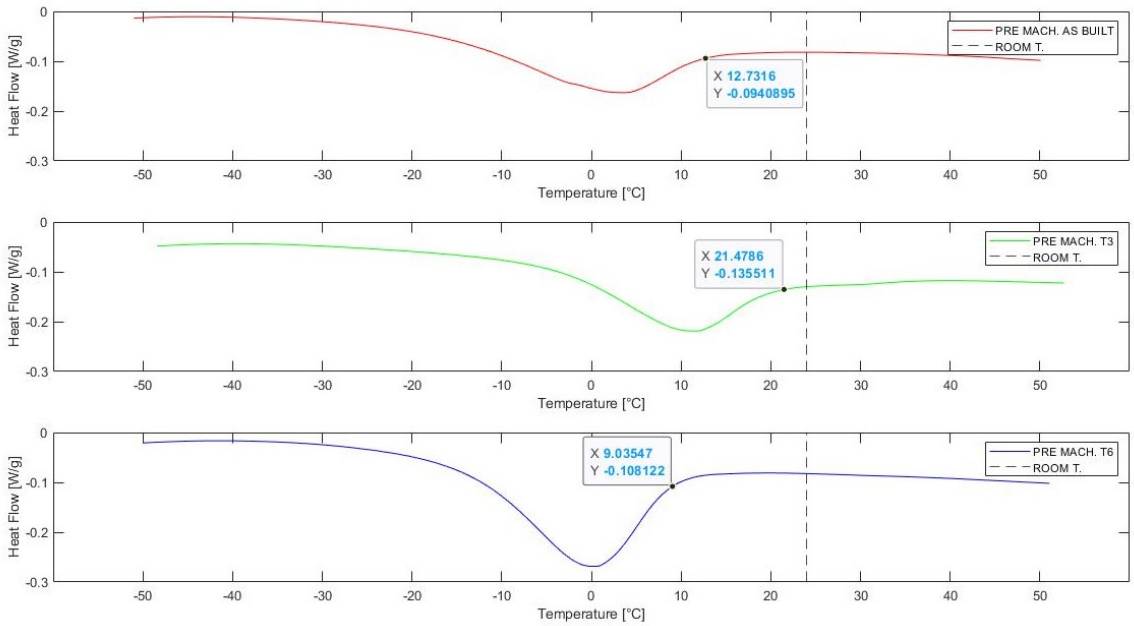

Figure 6. 14: Martensite to austenite transformation of the Pre-machined specimens (AB, T3 and T6)

FLOOD DSC

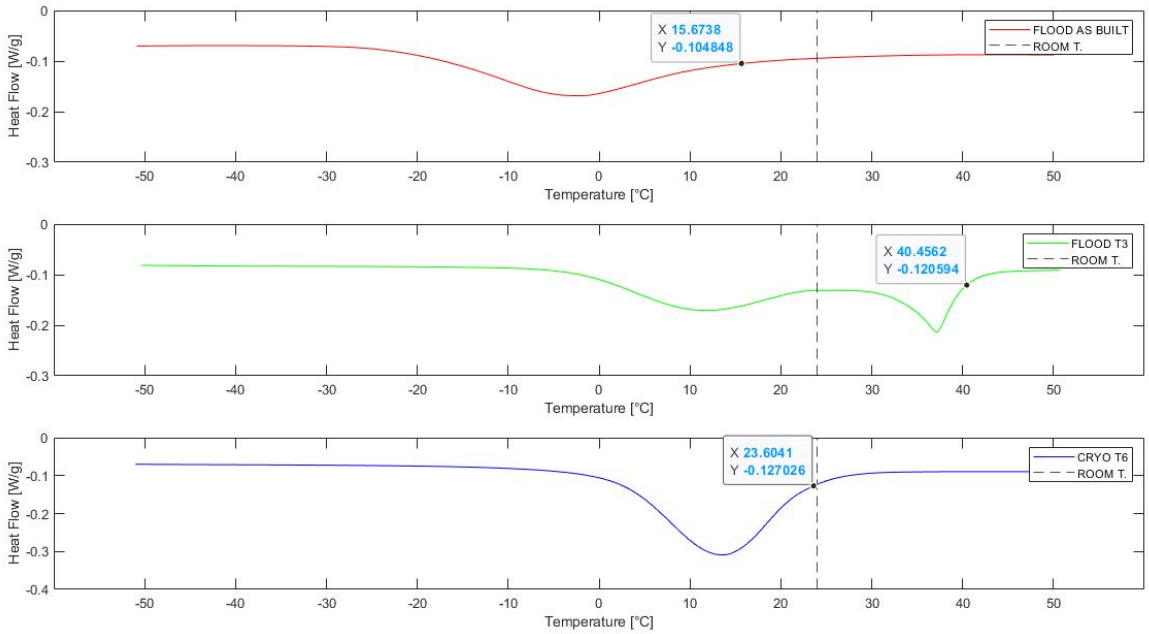

Figure 6. 15: Martensite to austenite transformation of the Flood specimens (AB, T3 and T6)

CRYO DSC

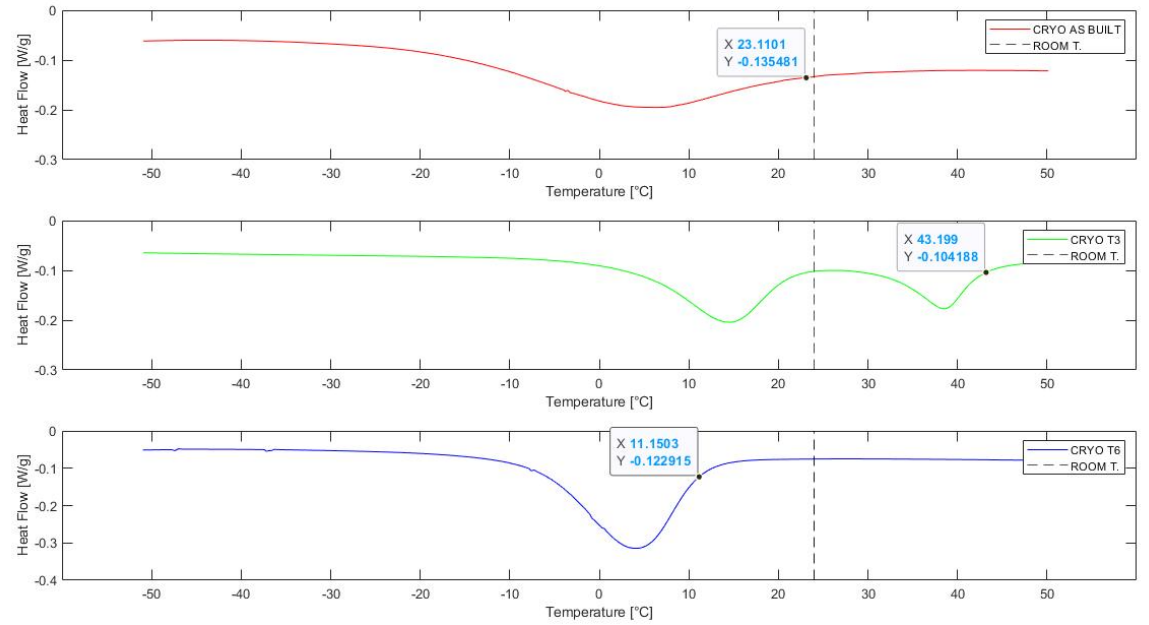

Figure 6. 16: Martensite to austenite transformation of the Cryo specimens (AB, T3 and T6)

6.3. 2 DSC Results – Pre Machining, Flood and Cryo comparison

In this paragraph, the thermal analysis focuses more on the difference between the pre-machining, flood and cryo processes cases. In the graphs, martensite start (or R-phase) is indicated by stars, and austenite finish by with fitted circles. It was decided to plot these points because they define the austenitic zone from that of the transition to martensite (top curve) or from martensite (bottom curve).

What can be concluded from the analysis of the graphs is:

1. in all cases machining leads to an increase in the transformation temperature, as announced in paragraph *2.4. 5 Effect of machining on processing temperatures*. In fact, the graphs reveal that the red marker (i.e., the one showing the pre-machining condition) always indicates lower temperatures than the flood (grey marker) and cryo (blue marker) conditions.
2. The difference between flood and cryo is more difficult to notice. However, in most cases it can be said that the cryogenic condition leads to a greater stabilisation of martensite (aka to an increase in transformation temperatures). This can be seen in the AB and T3 cases where the grey marker precedes the blue one. However, in the T6 samples the situation is the opposite, i.e., the flood condition has higher transformation temperatures.
3. In the case of the T3 samples AB flood sample, machining has led to the formation of the R phase.
4. Referring to cases (a), (b) and (c) in the paragraph *2.4. 5*, it can be deduced that:
    - pre-machining condition: it falls between cases (a) and (b)
    - flood condition: it belongs to case (a) with AB sample, case (c) with T3 sample and case (b) with T6 sample.
    - cryo condition is specular to the flood condition.

AS BUILT

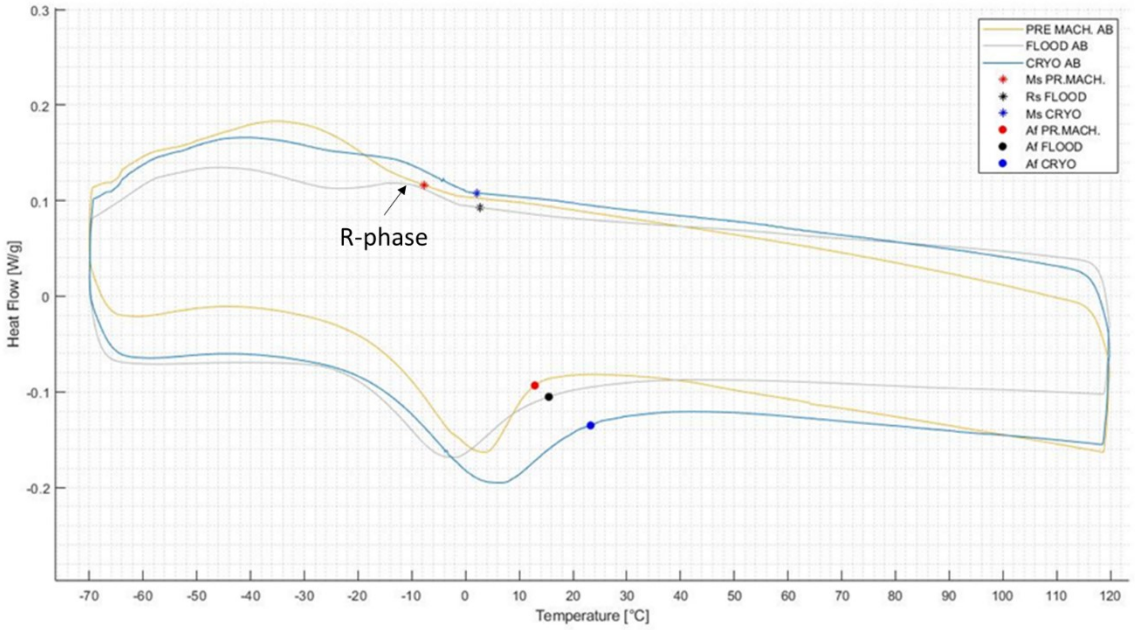

Figure 6. 17: Complete DSC cycle of AB specimens in the pre-machining, flood, and cryogenic cases. Martensite (or R-phase) start, and austenite finish points are shown.

T3

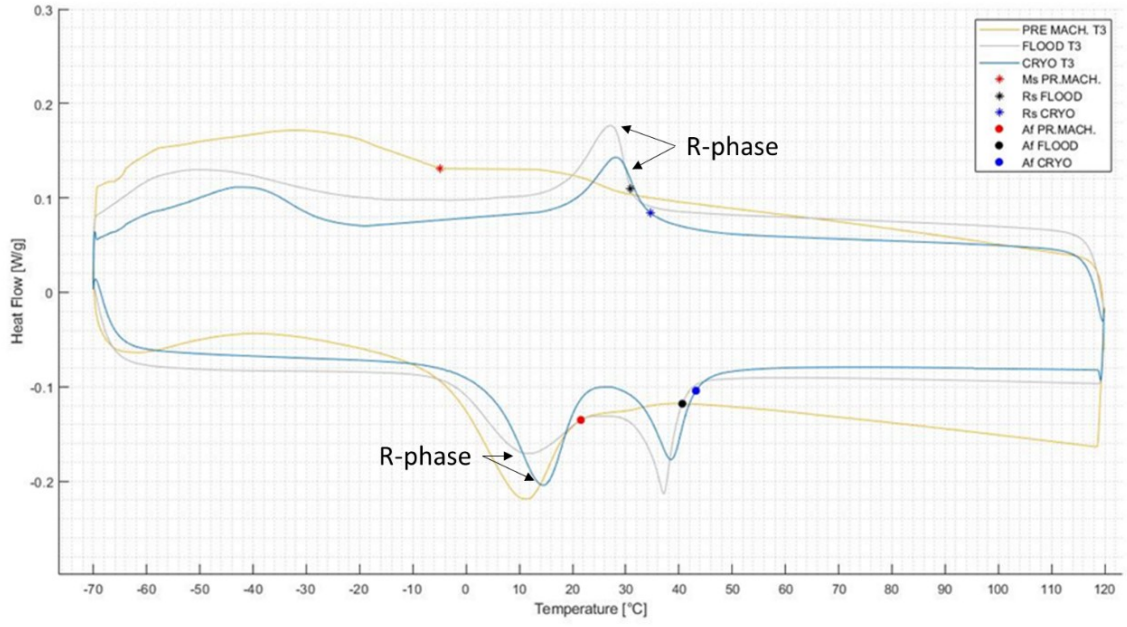

Figure 6. 18: Complete DSC cycle of T3 specimens in the pre-machining, flood, and cryogenic cases. Martensite (or R-phase) start, and austenite finish points are shown.

T6

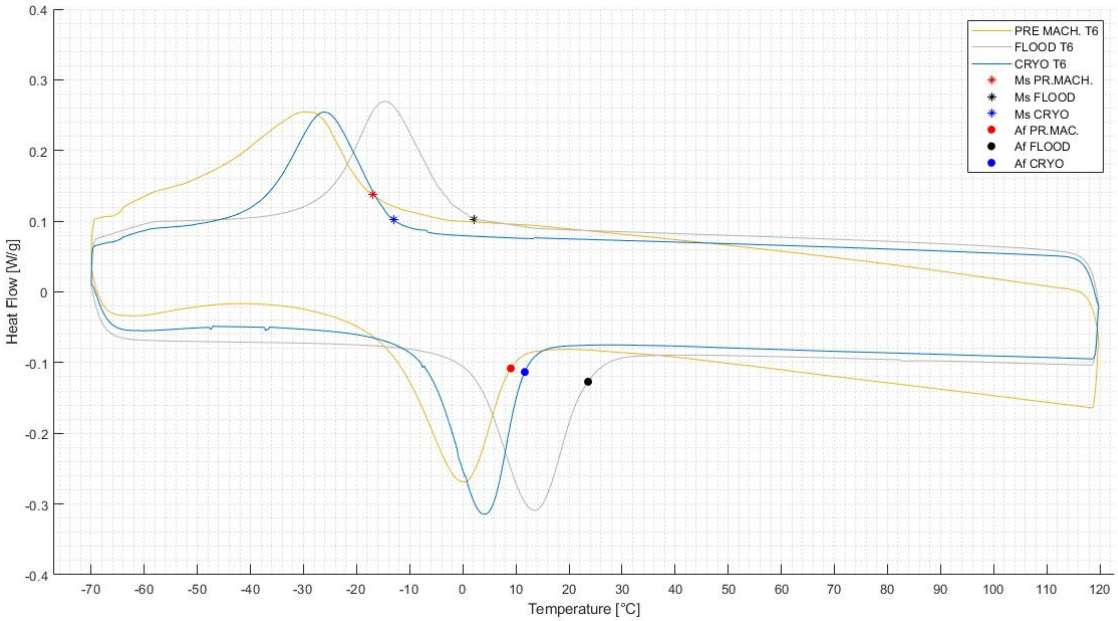

Figure 6. 19: Complete DSC cycle of T6 specimens in the pre-machining, flood, and cryogenic cases. Martensite start, and austenite finish points are shown.

6. 4 Nanoindentation results

Nanoindentation tests provided values for Young's modulus E, hardness H, and work recovery ratio μ. The data and graphs comparing these parameters for the different specimens are shown below, with reference to the differences between the pre-machined and machined specimens and between the heat treatments.

6.4. 1 Hardness

From the data and the graph, it can be seen that:

1. For AB and T6 specimens, the pre-machining hardness is always higher than that of the corresponding machined sample. This difference is particularly pronounced in the case of T6, where the hardness of the machined specimen is on average 39% lower than that of the pre-machined specimen.
2. Before machining T3 and T6 show the lowest and the highest hardness respectively, with one of the AB setting in between. Hardness is reduced by 48% for T3 and increased by 37% for T6 compared to sample AB. This could be attributed to the formation and type of precipitates from the two different heat treatments, grain coarsening compared to sample AB, as well as the recovery of the AM -induced residual stress.
3. There is never too much difference in hardness between flood and cryo.

	Pre-Machining			Flood			Cryo		
	AB	**T3**	**T6**	**AB**	**T3**	**T6**	**AB**	**T3**	**T6**
H (GPa)	6.58	3.43	8.99	5.36	3.99	5.23	5.02	3.71	5.65
Standard Deviation	1.38	0.47	1.24	0.33	0.6	0.65	0.39	0.51	0.71

Table 6. 4: specimens' hardness

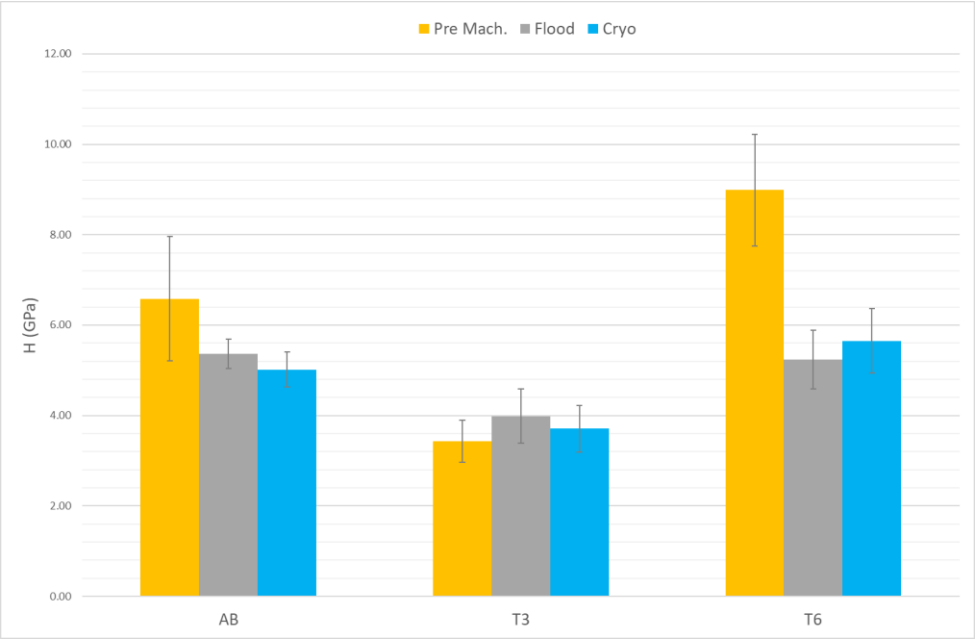

Figure 6. 20: hardness at varying process conditions.

6.4. 2 Elastic modulus

	Pre-Machining			Flood			Cryo		
	AB	**T3**	**T6**	**AB**	**T3**	**T6**	**AB**	**T3**	**T6**
E (GPa)	82.18	63.33	98.53	70.42	72.12	73.37	67.97	60.37	76.62
Standard Deviation	10.43	6.84	13.77	3.89	6.3	11.25	5.4	3.1	6.65

Table 6. 5: specimens' elastic modulus

The following section shows the results of the Modell ratio, i.e., the relationship between hardness and elastic modulus. This parameter is important because it indicates the resilience of the material, as discussed in section *2.6. 2.*

6.4. 3 Modell ratio

When talking about resilience, it is useful to combine the values of hardness and elastic modulus rather than considering them as separate data. For this reason, the Modell ratio parameter is introduced, which is the ratio of material hardness to the corresponding modulus of elasticity. A high value of the Modell ratio means that the material can tolerate a high level of penetration depth without exceeding the elastic limit. The value of the Modell ratio MR is then calculated from the ratio between the hardness and elastic modulus results given above:

	Pre-Machining			Flood			Cryo		
	AB	**T3**	**T6**	**AB**	**T3**	**T6**	**AB**	**T3**	**T6**
MR	0.08	0.054	0.09	0.076	0.055	0.071	0.074	0.061	0.074
Standard Deviation	0.009	0.006	0.007	0.005	0.006	0.008	0.005	0.008	0.007

Table 6. 6: specimens' MR

As can be seen from the data, the trend is like that seen in the case of hardness, so pre-machining samples AB and T6 show the highest MR values, while pre-machining T3 is the lowest of all. In all three situations (pre-machining, flood and cryo) the T3 sample is the worst in terms of MR. In the case of the machined sample, both AB and T6 show similar values, whereas T6 pre-machining wins in terms of H/E ratio.

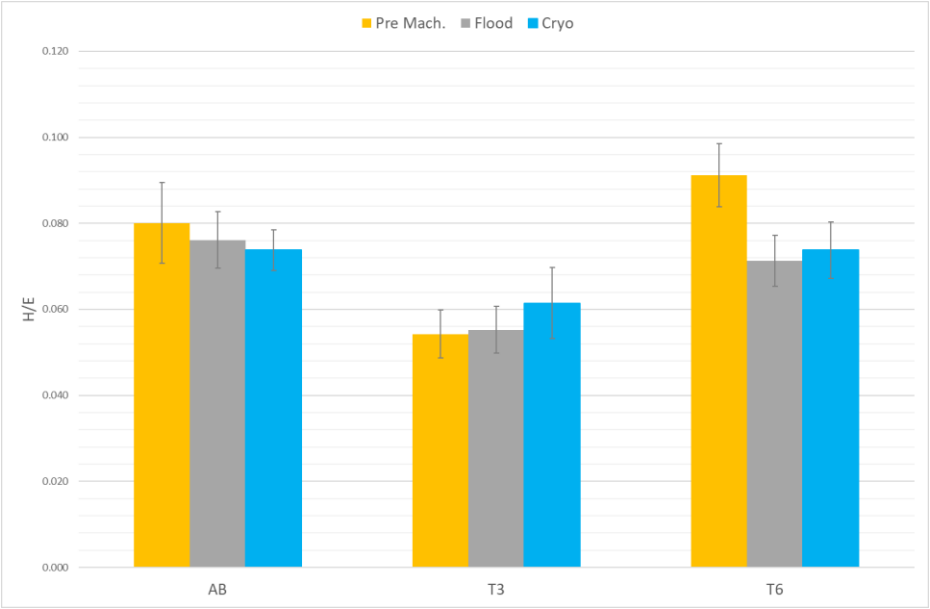

Figure 6. 21: Modell Ratio at varying process conditions.

6.4. 4 Recovery Ratios

The work recovery ratio, μ, and the depth recovery ratio, ψ (see equations (2. *16* and (2. *17*), are useful parameter for assessing the recoverable deformation capacity of NiTi. The results of the recovery rates obtained from the nanoindentation tests are as follows:

	Pre-Machining			Flood			Cryo		
	AB	**T3**	**T6**	**AB**	**T3**	**T6**	**AB**	**T3**	**T6**
μ	0.591	0.444	0.718	0.459	0.388	0.551	0.529	0.482	0.515
Standard deviation	0.082	0.051	0.045	0.024	0.020	0.047	0.028	0.027	0.034
ψ	0.619	0.503	0.729	0.525	0.45	0.67	0.567	0.503	0.558
Standard deviation	0.083	0.056	0.058	0.029	0.035	0.059	0.027	0.027	0.037

Table 6. 7: specimens' Work Recovery Ratio

The trend of the two parameters is the same, so only the graph of the work recovery ratio is shown below. In the pre-machining condition, ageing at 300° results in a 25% decrease in μ compared to sample AB, whereas ageing at 600° results in a 21% increase in μ. This shows once again how the different ageing temperatures, and the following effects, led to a worsening or an improvement of the AB situation.

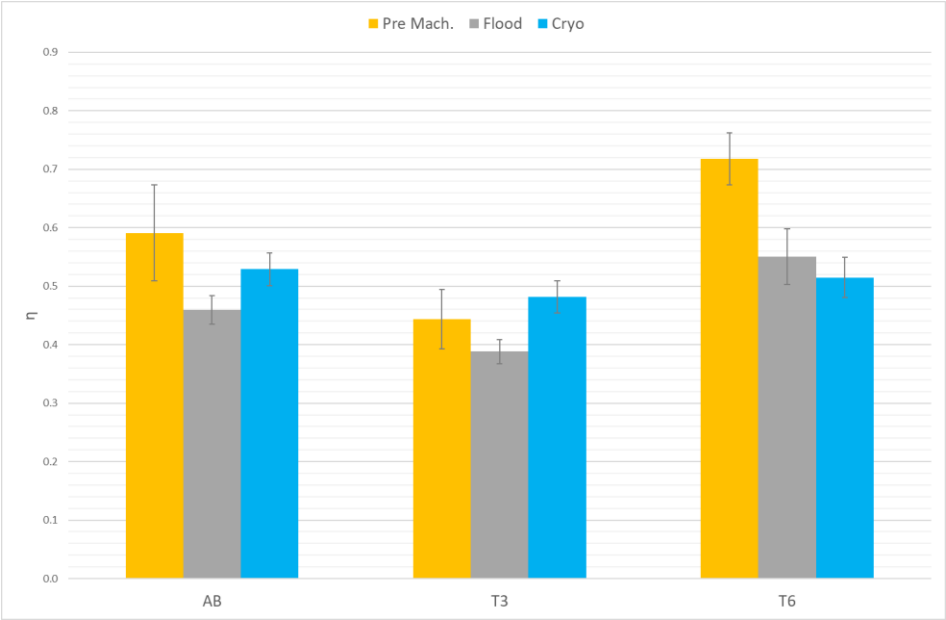

Figure 6. 22: work recovery ratio at varying process conditions.

The following graph shows the loading/unloading characteristics of the three conditions before machining and cryogenic machining. These curves have been chosen because they are the most representative of the elastic recovery. It is easy to see that the T6 curve is the one with the highest elastic recovery, i.e., with the highest value of depth recovery ratio, ψ, followed by the AB curve and finally the T3 curve.

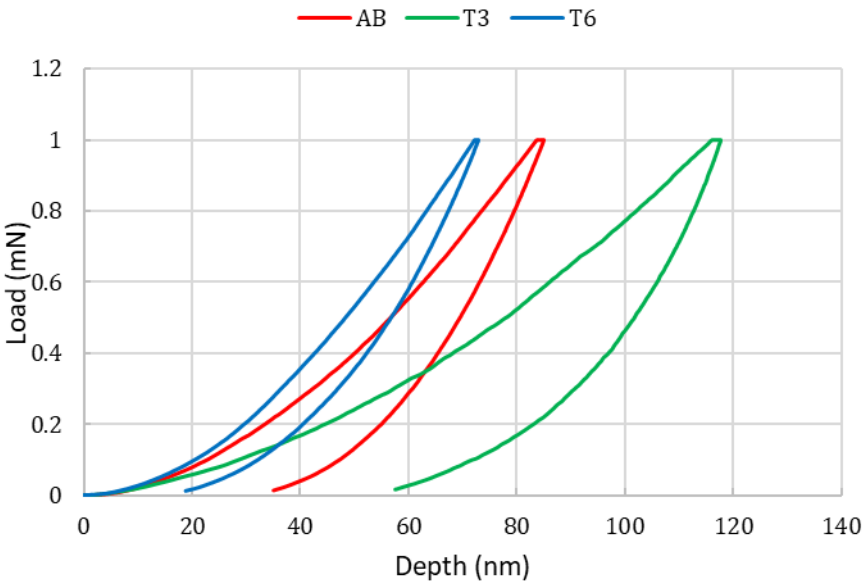

Figure 6. 23: Load vs. indentation depth curves before machining.

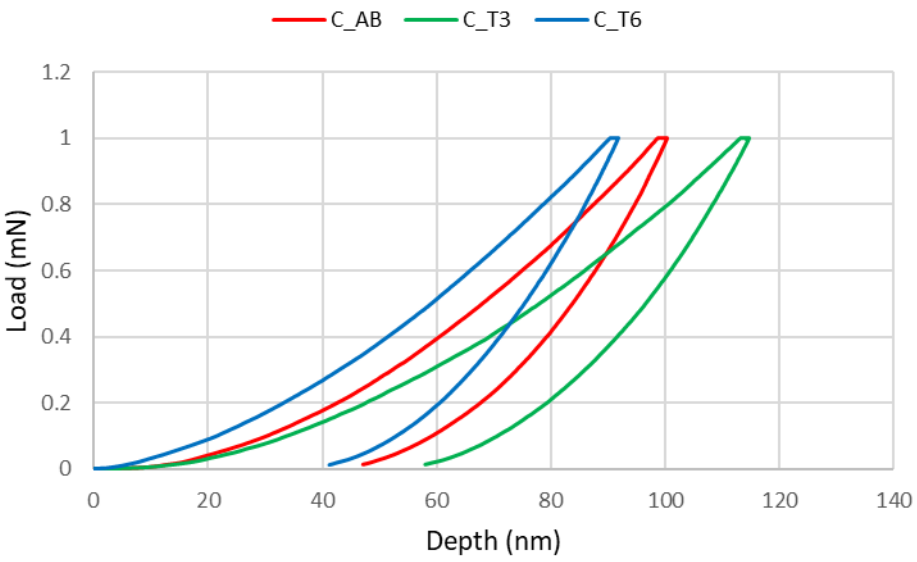

Figure 6. 24: Load vs. indentation depth curves cryogenic machining

6. 5 Wear and friction coefficient

6.5. 1 Volume loss results

Below are the results of the profilometer measurements of the wear of the balls because of the tribometer test illustrated in Chapter 5. The mean radius value of the worn circular area, wear depth and volume loss are given.

Two volume losses were calculated, the first using the method described in equations 5.3-5.6 and the second with the one suggested by the Standard (ASTM G99), i.e., equation 5.7. The percentage variation between the two methods is given in the last column.

	Ball Specimens	**Mean Radius** (a) **(mm)**	**Wear Depth** (h) **(mm)**	**1°Volume Loss** (V1) **(mm^3)**	**2° Volume Loss** (V2) **(mm^3)**	**V2-V1 %**
Flood	**F_AB**	0.55	0.032999	0.015699	0.015624	0.48
	F_T3	0.722	0.057088	0.046903	0.046515	0.83
	F_T6	0.400	0.017391	0.004365	0.004354	0.25
Cryo	**C_AB**	0.451	0.022194	0.007107	0.007084	0.32
	C_T3	0.709	0.054989	0.043524	0.043177	0.80
	C_T6	0.389	0.016459	0.00391	0.003901	0.24
	STEEL	0.350	0.013335	0.002567	0.002562	0.19

Table 6. 8: wear test results in terms of average wear radius, wear depth, volume loss

From the last column of the table, it can be seen that the difference between the two methods can be neglected when calculating the volume loss, hence the volume loss values will refer to the first method, i.e. V1, which will be simply denoted by V.

The table also shows that, as expected, the larger the wear radius a, the greater the wear depth h and the volume exported V.

The volume loss data has been plotted in the following graph comparing the different heat treatments.

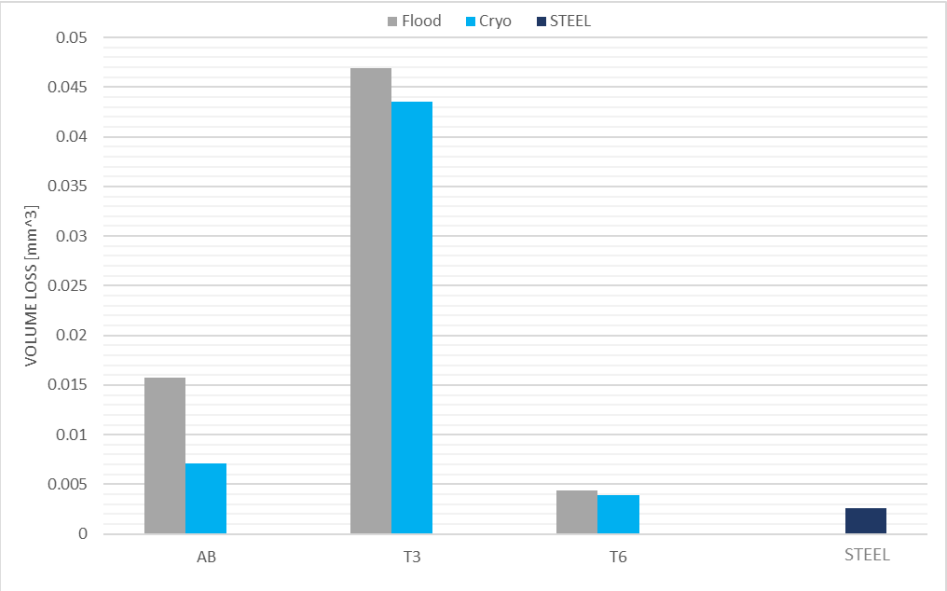

Figure 6. 25: volume loss graph

More than the difference between flood and cryo, what is eye-catching is the variation between the heat treatments. In particular, the 300°C ageing treatment (T3) appears to have lost much more material than the other two (AB and T6).

On average, the percentage change in volume loss between T3 and T6 samples is approximately 90%, while the difference between T3 and AB samples is 75%. The variance between AB and T6 is more modest, at around 63%. The T6 samples are the only ones with a volume loss value comparable to that of steel, with an average percentage difference of around 38%.

	Volume Loss Difference Δ%
AB – T3	74.8 %
T6 – T3	90.85 %
T6 – AB	63.7 %
Steel – T6	38 %

Table 6. 9: percentage variation in volume loss between heat treatments and between T6 and steel

Another notable observation is the difference between flood and cryo, which is greatest for the untreated specimens (AB), where flood processing loses about 55% more material than cryo. This difference is much less pronounced for the heat-treated specimens (T6 and T3), where the variation between flood and cryo is about 10%. Finally, in all circumstances cryo is the most suitable for tribological testing since it results in less volume loss than the flood condition.

It can be assumed that the difference in volume loss between cryo and flood is secondary to the difference between the heat treatments. This is demonstrated by T3 and T6 where the volume loss of the former is 90% greater than that of the latter.

6.5. 2 Hertzian pressure

This paragraph calculates the Hertzian pressure at the start and end of the tribological test. To do this it is necessary to know the applied load (F_z), the radius (R) of the pin (ball in this case), the modulus of elasticity and the Poisson's coefficient of the pin and disc.

The abbreviations used below have the following meanings:
a_i = radius of the contact area at the beginning of the test (calculated from equation 2.21)
P_i = Hertzian pressure at the beginning of the test (it depends on a_i and is calculated from equation 2.25)
a_f = mean radius of the worn area at the end of the test (it corresponds to the mean radius reported in *Table 6. 8)*
P_f = Hertzian pressure at the end of the test (it depends on a_f and is calculated from equation 2.25)

The following table shows the Hertzian contact results:

	Ball Specimens	P_i (MPa)	P_f (MPa)	$P_f - P_i$ %
Flood	**F_AB**	675	15.8	97.66
	F_T3	683	9.15	98.66
	F_T6	689	29.9	95.66
Cryo	**C_AB**	663	23.4	96.46
	C_T3	624	9.49	98.48
	C_T6	703	31.6	95.51
	STEEL	1068	39.0	96.35

Table 6. 10: Hertzian pressure at the start and end of the test

There is a drastic drop in Hertzian pressure between the beginning and end of the tribological test, as it is higher than 95% for all samples. The specimen with the greatest difference is F_T3, which is also the one that has worn the most, while C_T6 has the smallest pressure difference and is also the one that has worn the least.

6.5. 3 Comparison of wear scars

The horizontal diameter profiles of the worn zone, i.e. those perpendicular to the sliding direction, are shown below. Special attention is given to the surface condition of the worn zone. Using SENSOVIEW, it was possible to remove the plane error through the 'Shape removal/Plane' tool.

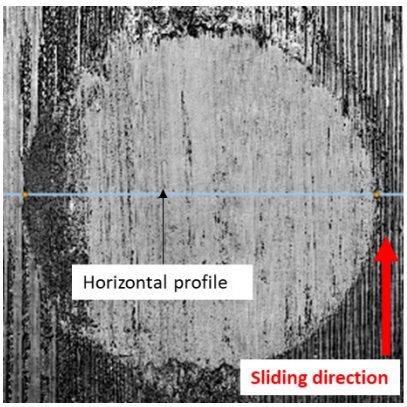

Figure 6. 26: wear scar of C_AB sample

The horizontal blue line in the previous figure corresponds to the following C_AB horizontal profile.

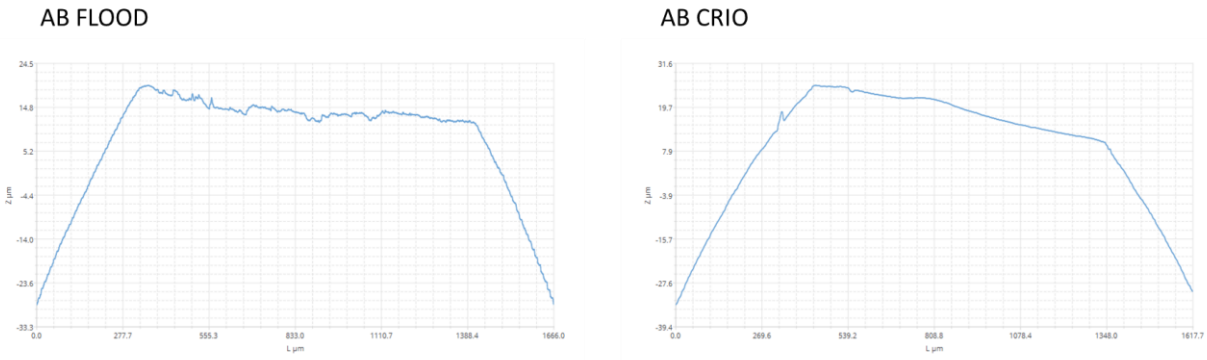

Figure 6. 27: comparison between AB horizontal profiles

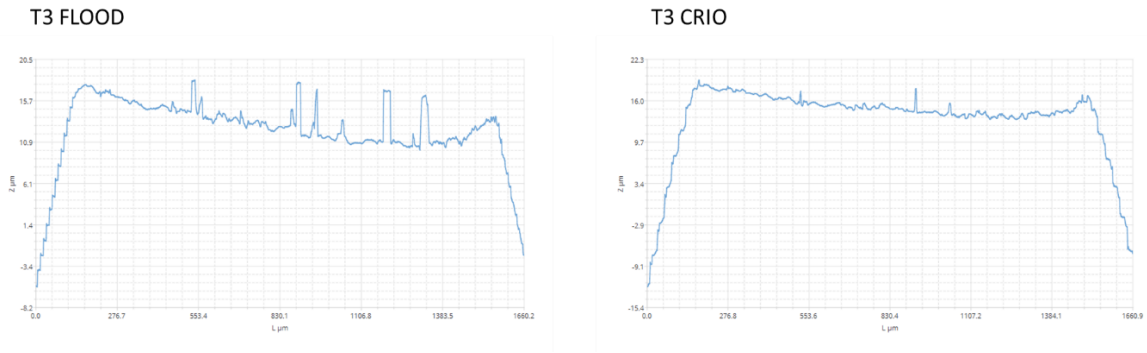

Figure 6. 28: comparison between T3 horizontal profiles

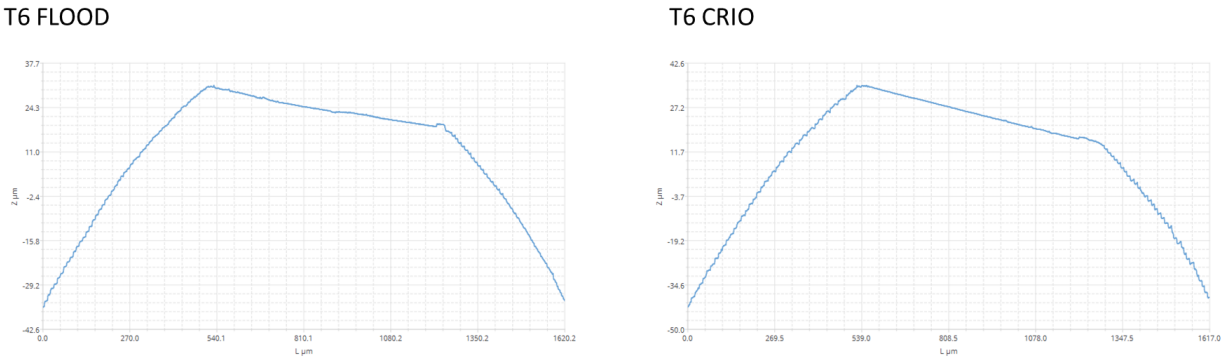

Figure 6. 29: comparison between T6 horizontal profiles

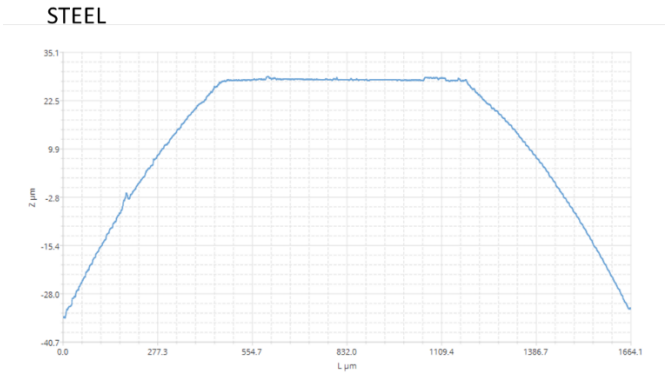

Figure 6. 30: STEEL horizontal profile

Profile comparisons show that the cryo samples have a smoother surface. In contrast, flood samples are more irregular and prone to adhesion of the material with which they are in contact.

In the case of the T6 specimens, which have suffered less wear than the other specimens, the difference between flood and cryo is almost imperceptible and their profile is also very similar to that of steel. Again, the trend indicated by the volume loss analysis is confirmed.

SEM images obtained with the BSED detector are shown below. The edges of the worn scar of the T3 samples are much better defined and the adhesion of the material from the disc is homogeneously distributed (black spots). In the case of the less worn C_T6 and steel, adhesion is present, but it is more concentrated and alternates with flat and poorly pitted areas.

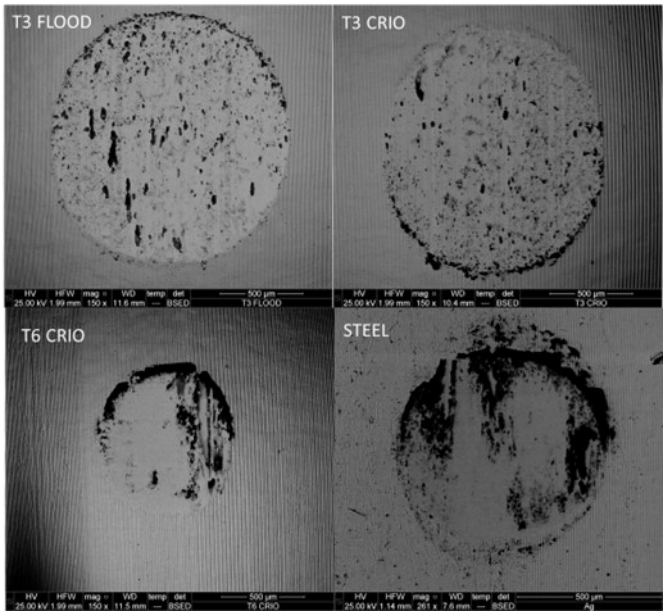

Figure 6. 31: BSED SEM images of the worn scars of F_T3, C_T3, C_T6 and STEEL samples.

6.5. 4 Coefficient of friction

Below are the results of the initial coefficient of friction (Initial COF), the steady state coefficient of friction (Steady state COF) and the point in the test at which it is reached (Steady state starting time).

	Ball Specimens	Initial COF	Steady state COF	Steady state Starting time (s)
Flood	**F_AB**	0.155 ± 0.049	0.372 ± 0.088	500
	F_T3	0.171 ± 0.068	0.395 ± 0.048	500
	F_T6	0.142 ± 0.041	0.397 ± 0.067	1200
Cryo	**C_AB**	0.171 ± 0.059	0.393 ± 0.039	600
	C_T3	0.175 ± 0.058	0.406 ± 0.051	300
	C_T6	0.143 ± 0.05	0.357 ± 0.076	1100
	STEEL	0.280 ± 0.094	0.522 ± 0.009	800

Table 6. 11: COF results

The following graph compares the steady state COF of the different samples. The red dots also show the value of the SS starting time. In the case of the coefficient of friction, it is not easy to find the trends observed in the other tests. However, the steel has the highest COF and is the most different from the Nitinol samples. It is also interesting to note that sample C_T6 has the lowest COF of all and that, in general, the T6 samples are the ones that are furthest behind in reaching the Steady state COF.

In addition, the samples that suffered most from the stick and slip effect had a higher standard deviation. Steel suffered very little from this effect and in fact had a much lower standard deviation than the Nitinol samples.

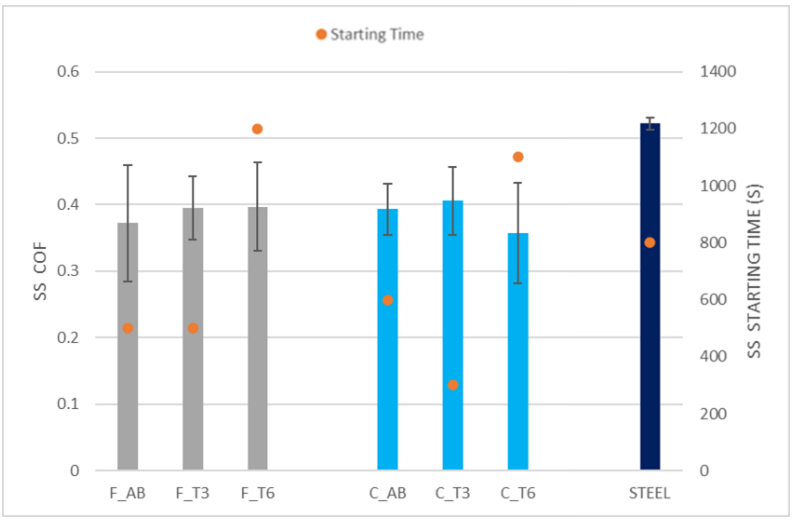

Figure 6. 32: steady state COF graph

CHAPTER 7

CONCLUSIONS AND FINDINGS

The aim of the work was to investigate an SMA alloy of nickel and titanium (50.8%at. Ni, 49.2%at. Ti), known for its shape memory and super-elastic properties. Many previous studies have looked at this type of material and its beneficial effects, but rarely they examine the behaviour of the alloy in combination with a process chain.

This study focused firstly on the implementation of a multi-stage path to evaluate different process parameters: firstly, the samples produced by additive manufacturing were subjected to different heat treatments: AB (no treatment), T3 (aged at 300°C) and T6 (aged at 600°C). A further subdivision of the samples took place during the machining process (turning), where two coolant configurations were adopted: flood and cryogenic.

At the end of the process chain, the samples differ depending on the heat treatment and processing conditions (flood or cryogenic). The decision to vary and analyse these parameters is based on the desire to study the formation of different types of precipitates because of ageing temperatures and to analyse the effects of flood versus cryogenic processing. Many studies have focused on the latter condition due to its advantages and the improvement in the surface integrity of turned parts using cryogenic gas as a cooling system.

At the end of the experimental work carried out on the samples obtained from the process chain, the results were evaluated in terms of surface roughness, transformation temperatures, hardness, elastic recovery, model ratio (H/E) and wear.

Looking at the results presented in the previous chapter, the following conclusions can be drawn: cryogenic machining brings an improvement in terms of surface roughness, which translates into improved fatigue life and better tribological performance of the material. Furthermore, from the images showing the SPD layer of the different machined specimens, cryogenic machining results in a thickening of this layer (see *Figure 6. 7*). However, the results of the various tests show a greater differentiation between the heat treatments, whereas the difference between flood and cryogenic processing often fades into the background. The reason for this is probably due to the microstructure and the formation of different types of precipitates because of the heat treatment. It was therefore concluded that the microstructure plays an important role in influencing the transformation temperatures and the material properties.

The FEG-SEM images (*Figure 6. 11*) clearly show the difference in precipitate size and number between the sample aged at 300°C and that aged at 600°C. As predicted by theory, the precipitates become finer and more coherent with the matrix as the ageing temperature decreases. Coherency with the matrix occurs when the precipitate is surrounded by a strain field that creates a strong resistance to the direct formation of the martensitic transformation. This is confirmed by the DSC analysis (see *Figure 6. 14 – 6.16*), where T3 machined samples show a clear delay in reaching the temperature of A_f. This demonstrates that the presence of spherical precipitates coherent with the matrix leads to an increase in transformation temperatures. In general, it can be concluded that machining itself leads to an increase in transformation temperatures. In fact, the samples are austenitic at room temperature (24°C) in the pre-machining condition, which is no longer true when evaluating the post-machining condition of the T3 sample, where $A_f > T_R$ (room temperature).

From the DSC results, it appears that the T6 cryo sample is the best condition to obtain direct transformation and guarantee the austenitic phase at room temperature.

Once again, the type of precipitate is crucial, since in the case of ageing at 600°C, the precipitates have lost coherence with the matrix, so that the transformation temperatures decrease, allowing $A_f < T_R$. It is no coincidence that the load vs. indentation plots in Figure 6. 23-24 show that the T6 specimens have the greatest elastic recovery, confirming the fact that the condition where $A_f < T_R$, combined with direct transformation (no R phase), is the one best suited to exhibit the super-elastic property.

Regarding the hardness and Modell Ratio results, it can easily be seen that the pre-machining conditions of AB and T6 are always better than the corresponding post-machining conditions. In particular, the T6 pre-machining sample shows the highest hardness and H/E value compared to all other samples. The reduction in hardness after machining may seem an unexpected result, but it can be justified by the fact that A_f of unmachined specimens is always lower than A_f of machined specimens, which leads to a stabilisation of the austenitic phase, resulting in a higher critical stress for the martensitic transformation to occur and consequently an increase in hardness [28].

In the case of T3 specimens, the strain hardening effect due to machining predominates over the critical stress effect, as A_f of T3 before machining is close to the room temperature value, and consequently the hardness in T3 samples increases in both flood and cryo conditions.

Finally, the results show that the T6 sample is again the best in terms of hardness and that the cryogenic treatment resulted in a slight increase in hardness compared to the flood condition due to a thicker SPD layer induced by the cryogenic machining.

In terms of wear results, the Modell Ratio (H/E) parameter is an indicator of what can be expected from tribological testing. In fact, the results show that high values of the Modell Ratio result in low wear values and therefore lower volume removed.
Again, the specimens that show a clear wear resistance are those aged at 600°C, followed by the untreated (AB) specimens and finally the 300°C aged specimens, which show a clear worsening in terms of wear. Comparing the MR (Model Ratio) data of the AB and T6 machined specimens, no major differences can be seen; in fact, the best performance of the T6 specimens is in the inner part of the material (bulk), which shows high MR values. What happens is that the machined layers are eroded at the start of the test and then the innermost material with a higher MR is attacked. The T6 cryo sample has a higher MR than the corresponding T6 flood, and the T6 samples also have the highest pre-machining MR. This combination makes the T6 cryo specimen the most favourable in terms of wear.
The T6 cryo specimen also has the lowest coefficient of friction, not only among the Nitinol samples, but also compared to steel.

It can be concluded that, in a process chain consisting of AM, heat treatment and finish machining on $Ni_{50.8}Ti_{49.2}$ samples, the heat treatment is the cause of the formation of precipitates whose shape, size and quantity determine the super-elastic response of the material, whereas machining reduces such properties. Cryogenic machining has also been demonstrated to improve performance in terms of roughness and wear resistance.

The super-elasticity and high Modell Ratio make Nitinol a good candidate for applications where it is necessary to support high loads and thus take advantage of the super-elasticity effect. As mentioned in Chapter 3, the Nitinol alloy is an interesting alternative to conventional materials in the bearing industry. In fact, when two surfaces are in contact and subjected to a radial load, the pressure in the contact zone decreases as the contact area increases due to high elastic deformation.
Even more satisfactory results in terms of wear resistance and hardness can be obtained by considering a 60NiTi alloy, as shown in the literature. However, the aim of the present work is not to compare different compositions of Nitinol or between the alloy and other conventional materials, but to study an SMA alloy to draw conclusions and observations on the effects of material properties induced by a process chain of industrial interest.

APPENDIX

DRAWING BOARD

Two drawings are shown below: the first refers to the sphere machined on the lathe to obtain the tribological test pin (the various machining steps are shown), the second refers to the fixing plate specifically designed for the tribological test.

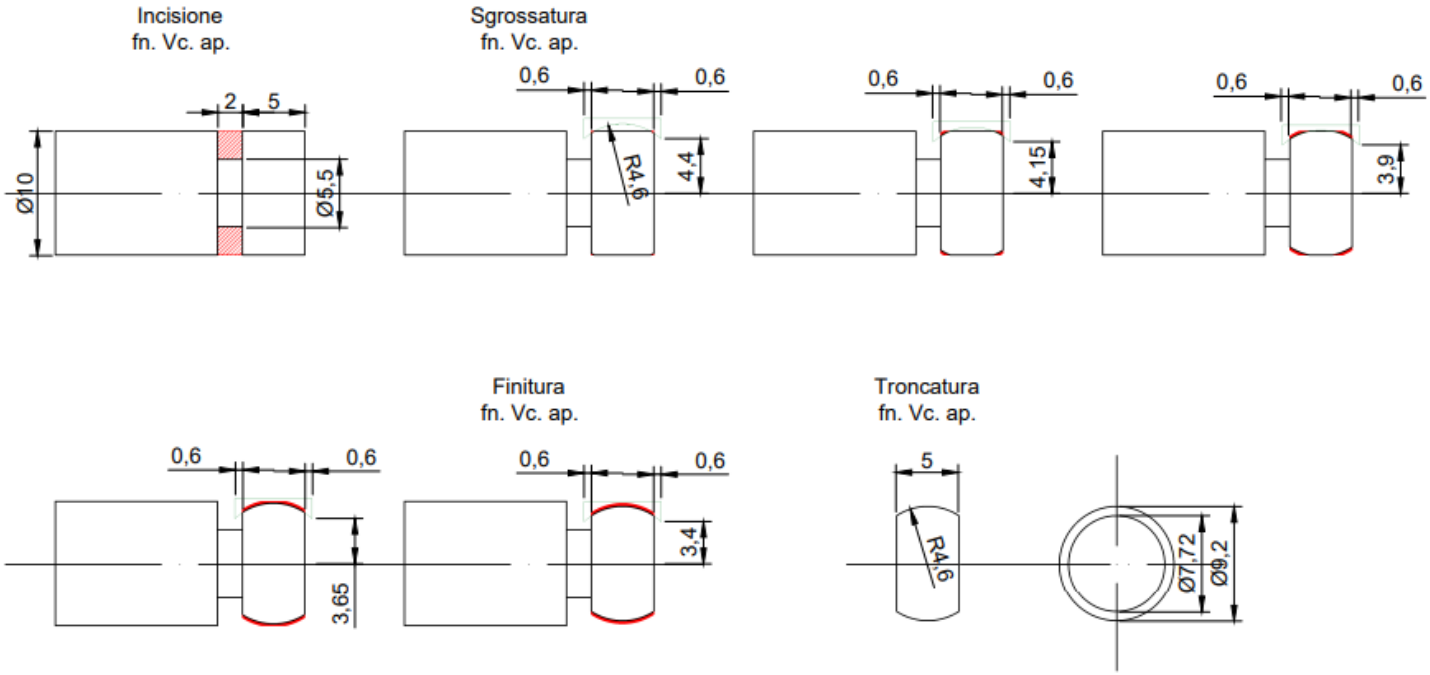

Legenda	
	Percorso Utensile
	Materiale asportato

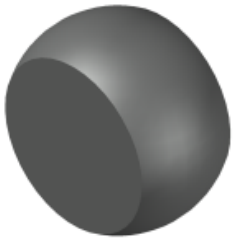

UNIVERSITÀ DEGLI STUDI DI PADOVA

Campione sferico troncato per tribologia

Data	Tavola	Scala
6/12/2021	U	2:1

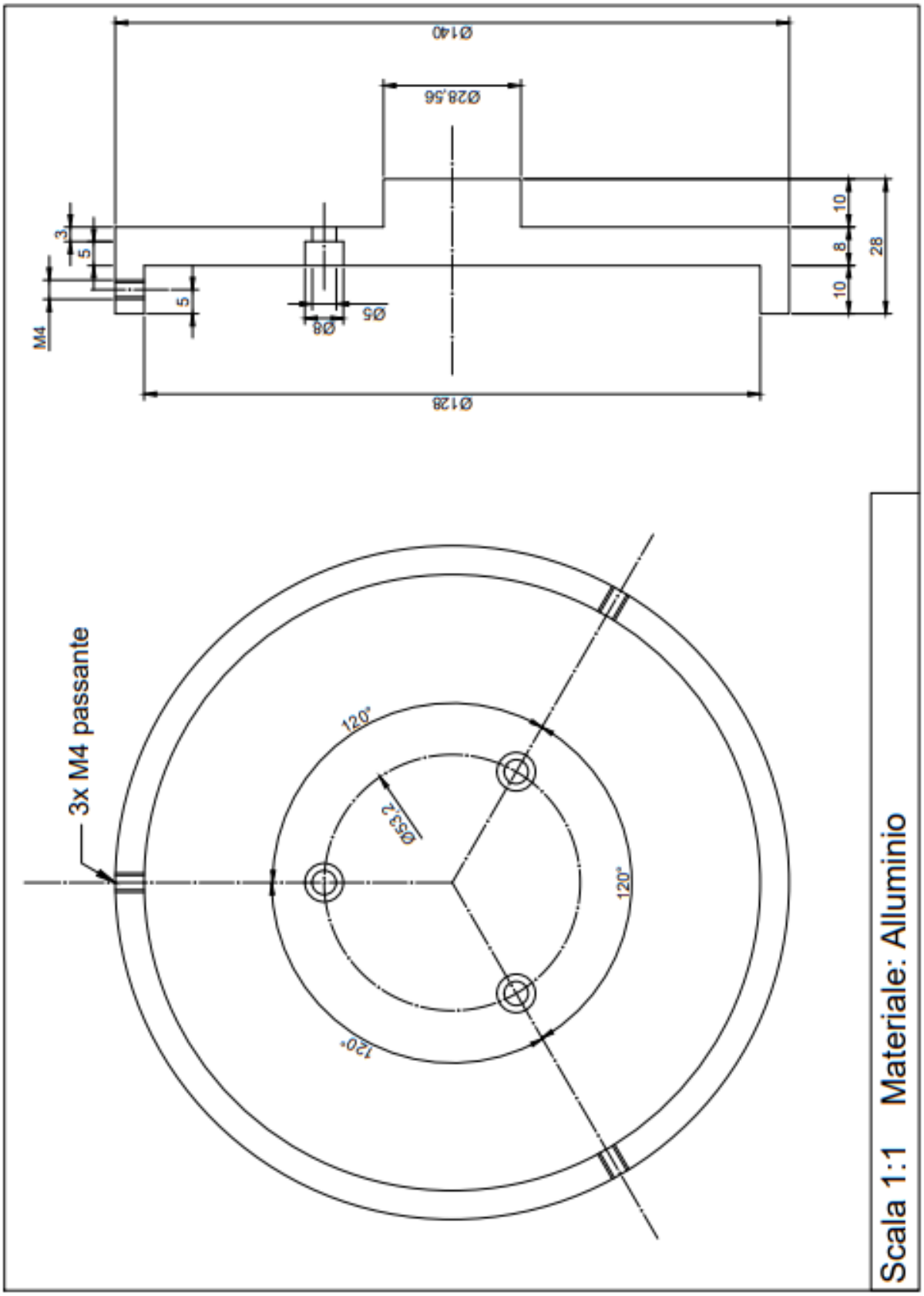
Ø140
Ø28,56
10
8
28
10
3
5
5
M4
Ø5
Ø8
Ø128
3x M4 passante
120°
Ø53,2
120°
120°
Scala 1:1 Materiale: Alluminio

BIBLIOGRAPHY

[1] C. Dellacorte and L. E. M. Iii, “Launch Load Resistant Spacecraft Mechanism Bearings Made From NiTi Superelastic Intermetallic Materials.”

[2] V. Buljak and G. Ranzi, “Shape memory alloys,” in *Constitutive Modeling of Engineering Materials*, Elsevier, 2021, pp. 293–313. doi: 10.1016/B978-0-12-814696-5.00014-9.

[3] “Quality enhancement of microstructure and surface topography of NiTi parts produced by laser powder bed fusion _ Elsevier Enhanced Reader”.

[4] P. A. ÍPRAVA MARTENZITICKÉ TRANSFORMACE SLITIN NA BÁZI NiTi, “PROCESSING AND MARTENSITIC TRANSFORMATIONS OF NiTi-BASED ALLOYS DIZERTA ¡ NÍ PRÁCE.”

[5] “Introduction to Nitinol,” 2017.

[6] E. Patoor, D. C. Lagoudas, P. B. Entchev, L. C. Brinson, and X. Gao, “Shape memory alloys, Part I: General properties and modeling of single crystals,” *Mechanics of Materials*, vol. 38, no. 5–6, pp. 391–429, May 2006, doi: 10.1016/j.mechmat.2005.05.027.

[7] Y. Guo, A. Klink, C. Fu, and J. Snyder, “Machinability and surface integrity of Nitinol shape memory alloy,” *CIRP Ann Manuf Technol*, vol. 62, no. 1, pp. 83–86, 2013, doi: 10.1016/j.cirp.2013.03.004.

[8] M. Elahinia, N. Shayesteh Moghaddam, M. Taheri Andani, A. Amerinatanzi, B. A. Bimber, and R. F. Hamilton, “Fabrication of NiTi through additive manufacturing: A review,” *Progress in Materials Science*, vol. 83. Elsevier Ltd, pp. 630–663, Oct. 01, 2016. doi: 10.1016/j.pmatsci.2016.08.001.

[9] K. Khanlari, “Mechanical and tribological characterization of NiTinol 60 parts manufactured by different powder metallurgy processes,” 2018.

[10] “Leghe a memoria di forma.”

[11] A. R. Pelton’, J. Dicellol, and S. Miyazaki2, “Optimisation of processing and properties of medical grade Nitinol wire,” 2000.

[12] X. B. Wang, B. Verlinden, and J. van Humbeeck, “R-phase transformation in NiTi alloys,” *Materials Science and Technology (United Kingdom)*, vol. 30, no. 13, pp. 1517–1529, Nov. 2014, doi: 10.1179/1743284714Y.0000000590.

[13] S. Kalpakjian, S. R. Schmid, and K. S. V. Sekar, *Manufacturing engineering and technology*.

[14] I. S. Jawahir *et al.*, “Cryogenic manufacturing processes,” *CIRP Ann Manuf Technol*, vol. 65, no. 2, pp. 713–736, 2016, doi: 10.1016/j.cirp.2016.06.007.

[15] Y. Kaynak, B. Huang, H. E. Karaca, and I. S. Jawahir, “Surface Characteristics of Machined NiTi Shape Memory Alloy: The Effects of Cryogenic Cooling and Preheating Conditions,” *J Mater Eng Perform*, vol. 26, no. 7, pp. 3597–3606, Jul. 2017, doi: 10.1007/s11665-017-2791-7.

[16] M. R. Aboutalebi, M. Karimzadeh, M. T. Salehi, S. M. Abbasi, and M. Morakabati, “Influences of aging and thermomechanical treatments on the martensitic transformation and superelasticity of highly Ni-rich Ti-51.5 at.% Ni shape memory alloy,” *Thermochim Acta*, vol. 616, pp. 14–19, Sep. 2015, doi: 10.1016/j.tca.2015.08.004.

[17] S. K. S, I. A. Kumar, L. Marandi, and I. Sen, “Assessment of small-scale deformation characteristics and stress-strain behavior of NiTi based shape memory alloy using nanoindentation,” *Acta Mater*, vol. 201, pp. 303–315, Dec. 2020, doi: 10.1016/j.actamat.2020.09.080.

[18] “45_OliverPharr1992Nanoindentation”.

[19] “nanoindentatrion”.

[20] T. L. Oberle, “Wear of Metals.”

[21] J. F. Archard, “Contact and rubbing of flat surfaces,” *J Appl Phys*, vol. 24, no. 8, pp. 981–988, 1953, doi: 10.1063/1.1721448.

[22] C. Press, “MODERN TRIBOLOGY HANDBOOK Volume One Principles of Tribology.”

[23] G. E. Morales-Espejel and A. Gabelli, “Rolling bearing seizure and sliding effects on fatigue life,” *Proceedings of the Institution of Mechanical Engineers, Part J: Journal of Engineering Tribology*, vol. 233, no. 2, pp. 339–354, Feb. 2019, doi: 10.1177/1350650118779174.
[24] A. Calvi, “Spacecraft Structural Dynamics & Loads An Overview.”
[25] E. Videira, C. Lebreton, S. D. Lewis, and L. Gaillard, “DESIGN, ASSEMBLY AND PRELOADING OF BALL BEARINGS FOR SPACE APPLICATIONS-LESSONS LEARNED AND GUIDELINES FOR FUTURE SUCCESS.”
[26] C. Dellacorte, R. D. Noebe, M. K. Stanford, and S. A. Padula, “Resilient and Corrosion-Proof Rolling Element Bearings Made From Superelastic Ni-Ti Alloys for Aerospace Mechanism Applications,” 2011. [Online]. Available: http://www.sti.nasa.gov
[27] N. Shayesteh Moghaddam *et al.*, “Achieving superelasticity in additively manufactured NiTi in compression without post-process heat treatment,” *Sci Rep*, vol. 9, no. 1, Dec. 2019, doi: 10.1038/s41598-018-36641-4.
[28] K. Khanlari, Q. Shi, K. Li, K. Hu, P. Cao, and X. Liu, “Effects of printing volumetric energy densities and post-processing treatments on the microstructural properties, phase transformation temperatures and hardness of near-equiatomic NiTinol parts fabricated by a laser powder bed fusion technique,” *Intermetallics (Barking)*, vol. 131, Apr. 2021, doi: 10.1016/j.intermet.2021.107088.

[29] https://www.olympus-ims.com/en/metrology/surface-roughness-measurement-portal/